Master of Science in Applied Geophysics
Research Thesis

Distributed Acoustic Sensing: Exploring the potential of unconventional fiber configurations

---

Zurich, August 6, 2021

Author:
Tjeerd Kiers (19-944-164)

Supervisors:
Dr. Pascal Edme
Dr. Patrick Paitz
Prof. Dr. Andreas Fichtner

External examiner:
Dr. Norbert Klitzsch (RWTH Aachen)

Abstract

Over the last decade, Distributed Acoustic Sensing (DAS) has gained increased attention as a cost-effective and practical ground motion monitoring technique, due to the unprecedented temporal and spatial sampling possibilities. Considering these inherent advantages, DAS-collected strain rate measurements can be beneficial as addition to traditional particle motion sensors, or potentially replace them under certain circumstances.

A DAS system, consisting of an interrogator and attached optical fiber, is conventionally employed in a single (inline) direction providing 1D longitudinal strain rate measurements along the installed fiber. In this thesis, we explore unconventional fiber configurations to retrieve additional wavefield components. To investigate the potential of these unconventional fiber geometries, we perform numerical tests, discuss real data from a field campaign in Yverdon (Switzerland) and report on our analysis of synthetic and field data.

Both synthetic and field results show that a loop- and cross fiber lay-out provide the pseudo-divergence, defined as the sum of the local spatial velocity gradients ($\partial_x v_x + \partial_y v_y$), which is proportional to the full wavefield divergence at the free surface. We confirm that the fiber loop & cross shape predominantly capture Rayleigh surface waves, but are insensitive to Love wave energy. An important factor regarding the loop & cross behaviour is the configuration size with respect to the wavelength (λ). Reduced amplitudes are recognizable for loop & cross dimensions spanning more than $1/5\lambda$, followed by additional phase distortions from $1/3\lambda$ and completely altered waveforms for even larger loop & cross sizes.

We show that a spherical configuration (composed of 3 independent orthogonal fiber loops) is theoretically attractive by enabling the retrieval of both the full divergence and the individual spatial gradients in the three orthogonal directions. The free surface-relation between the pseudo- and full divergence can be exploited to approximate the local ratio of the shear and pressure wave velocity (V_S/V_P), which is demonstrated with synthetic data by means of spectral element modeling. However, the field results are less convincing due to, supposedly, poor cable-ground coupling as a result of required dense cable winding.

Finally, we introduce a local approach to estimate the effective shear velocity (V_S) without the need for larger arrays. We achieve this by combining local gradients and particle acceleration data, obtained from the fiber loop and one centred 3C-geophone respectively. Our novel approach is validated with synthetic data and we present promising field data results. The proposed 4C-configuration mitigates traditional finite-difference errors related to tilted or inaccurately spaced ground motion sensors. Furthermore, our novel arrangement offers the advantage of azimuthal independence, which can be of interest for V_S-estimations from earthquake-, traffic- or potentially ambient noise recordings. The local character of the effective V_S-computation is dependent on the incident P-wavelength and is therefore potentially exploitable with regard to 1D shear velocity subsurface models.

The presented synthetic and field results in this thesis show the potential of employing unconventional fiber configurations with regard to multi-component gradient sensing. This work further contributes to the development of attractive DAS applications at various scales, especially related to wavefield separation (ground-roll suppression), shallow static corrections and near-surface characterization.

Contents

List of Figures

1 Introduction

Over the past 10 to 15 years, Distributed Acoustic Sensing (DAS) has increased massively in popularity in the seismological and seismic exploration community. This is mainly due to the big potential many researchers and engineers see and predict for DAS (Ajo-Franklin et al., 2019; Kamal, 2014). We see an impressive development regarding DAS systems and related physical concepts, which is expected to continue in the near future as well (Fenta & Szanyi, 2021). This will pave the road for new applications and ways to profit from the potential of DAS.

In general, DAS collects seismic strain (rate) recordings along an optical (glass) fiber by utilizing an interrogator, which sends a laser pulse in the optical fiber and analyzes the back-scattered light. One of the first research and industry areas in which this became widely-used was Vertical Seismic Profiling (VSP), where the fiber was clamped to the tubing (Daley et al., 2013) or cemented behind the casing (Mateeva et al., 2014; Egorov et al., 2018). Afterwards, it went fast: DAS became more integrated in the seismic industry (Kamal, 2014) and many successful attempts were reported in other research areas as well, such as recording earthquake events (Lindsey et al., 2020; Luo et al., 2020) and passive noise/traffic monitoring (Ajo-Franklin et al., 2019; Dou et al., 2017; Peterson et al., 2020).

The reason why many researchers and industry partners are becoming increasingly interested in this new distributed sensing technique, is that DAS has some inherent advantages over conventional geophone arrays.

1. DAS enables us to retrieve seismic data along an optical fiber with unprecedented high spatial and temporal sampling (Farhadiroushan et al., 2010; Dou et al., 2017). The optical fiber is turned into a distributed seismic sensor which can be interrogated every 0.25m for tens of kilometers at the same time. This allows new seismic acquisition dimensions, which are impossible using conventional geophone strings.

2. Once an optical fiber is installed in a tube or trench, no further maintenance or preparation is needed. An interrogator can always be attached to one end of the fiber and seismic data can be recorded, which is particularly valuable for VSP or other monitoring applications (Mateeva et al., 2014) (Dou et al., 2017).

3. Compared to conventional geophones, optical fiber is often already a more economical choice and the prices are decreasing rapidly (Yin et al., 2008). To be specific, in 1979 a single mode commercial optical fiber costed around 20$/m and in 2008 this already decreased to 0.1$/m (Yin et al., 2008).

Although the advancement of DAS is going quick and the enthusiasm is growing, more research on multiple aspects is essential to retrieve the full potential of DAS. Active research topics are for instance handling the large volumes of data (Stork et al., 2020), overcoming or exploiting the directional (in)sensitivity of DAS (Den Boer et al., 2013; Kuvshinov, 2016) and potential multicomponent sensing (Ning, 2019; K. A. Innanen et al., 2019).

However, a topic which has not been extensively associated with DAS yet is wavefield gradiometry. In general, this seismic research field has received increasing attention since the great value of it was shown by J. O. A. Robertsson & Muyzert (1999) and J. Robertsson & Curtis (2002). Later on, these concepts proved to be the foundation for many applications described among others by Langston (2007), Maeda et al. (2016), Edme et al. (2018), Schmelzbach et al. (2018), Muyzert et al. (2019) and Van Renterghem (2019). Significant steps to relate this seismic subject to DAS have been made by Paitz (2021), but there is considerably more potential for combining DAS and wavefield gradiometry.

1.1 Motivation & objectives

In this thesis, we try to further explore the wavefield gradiometry potential of DAS. We attempt to do that by employing unconventional fiber configurations. With these configurations we expect to

measure interesting wavefield components such as the divergence. We study this gradiometry potential of DAS by:

1. Simulating innovative DAS configurations and analyzing their synthetic data output.
2. Conducting a field campaign at Yverdon (Switzerland) to compare the retrieved field data with synthetic results and test the feasibility of such fiber configurations in the field.

We have translated this ambition into several more specific objectives for this project. We will investigate, explore and report:

- the possibility of measuring the wavefield divergence with DAS.
- the opportunity to obtain multi-directional wavefield gradients utilizing DAS.
- the potential of retrieving local material properties from gradient DAS measurements.
- the feasibility of these utilized DAS configurations and recommendations to improve the experimental setup.

1.2 Outline

In order to report on our results and findings regarding the above-mentioned objectives, we have structured this thesis in the following way.
We start with a concise review of the relevant theory regarding Distributed Acoustic Sensing, its inherent directionality, the basics of wavefield gradiometry and the effect of the Earth's free surface in Chapter 2.
Subsequently, we give an overview of the field campaign at Yverdon, our synthetic model and the methodology in Chapter 3.

We have structured the theoretic potential, synthetic data and field results of the proposed DAS configurations into four chapters, namely chapter 4-7. Chapter 4 is focused on the data quality of the DAS configuration field data. Chapters 5 and 6 highlight the potential of measuring the pseudo-divergence by a fiber loop or cross and applying a gradient decomposition on DAS sphere data. Finally, chapter 7 extends this to characterizing the local material properties.
We conclude this thesis by highlighting some limitations, discussing the (potential) applications of this work and concluding the main findings in Chapters 8 and 9.

2 Theoretical background

This chapter contains some theoretical background and serves as a backbone for the entire thesis. First, the concept of Distributed Acoustic Sensing (DAS) measurements is described, with regard to the back-scattering principle, gauge length and strain rate output. Afterwards, we discuss the directionality property of a DAS system and highlight the omni-directional advantage of a fiber loop. We finish this chapter by reviewing wavefield gradiometry in general and the implications of the Earth's free surface.

2.1 Distributed Acoustic Sensing principles

2.1.1 Back-scattering principles

In general, a DAS system always consists of two parts: an optical fiber (FO) and an interrogator unit (IU) which sends a laser pulse into the fiber (Farhadiroushan et al., 2010). When this laser pulse hits one of the many naturally occurring impurities (density anomalies) in the glass fiber, a part of the light photons is randomly scattered in all directions by three scattering principles: Raman, Brouillon and Rayleigh scattering (Kechavarzi et al., 2019). Distributed Acoustic Sensing exploits the latter (Lindsey et al., 2020) and utilizes the light photons which are scattered back exactly in the fiber direction, as shown in Figure 1 (Lindsey et al., 2020).

These partly back-scattered light photons are sensed by the interrogator unit and linked to a spatial fiber location by making use of the travel time, speed of light and the refractive index of the optical fiber (around n=1.45) (Dean et al., 2017). This concept is called Optical Time Domain Reflectometry (OTDR) and is the most popular principle utilized in DAS systems.

As the DAS measuring principle is based on partial back-scattering of the propagating laser pulse, light intensity decreases at larger fiber distances. Hence, there is a practical limit from where the back-scattered light is not strong enough anymore to be detected by the interrogator. Currently, several tens of kilometers is achievable with a modern DAS system (Cedilnik et al., 2019), but this maximum sensing distance will increase in the future.

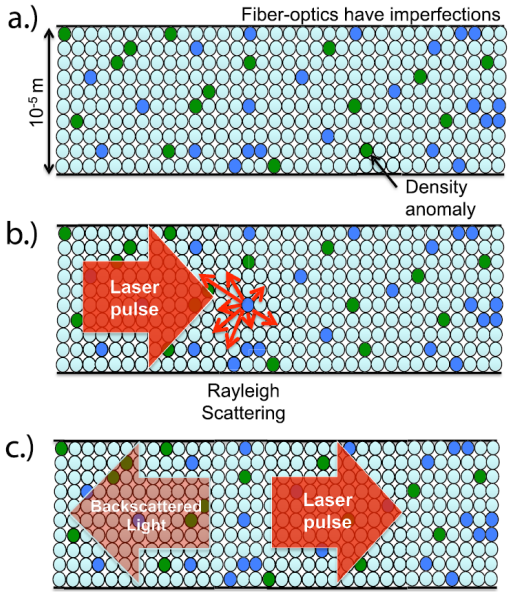

Figure 1: *Conceptual drawing from Lindsey et al. (2020) illustrating the back-scattering process of a DAS system. a) Cross-section of a standard optical fiber b) Incoming light pulse causing Rayleigh scattering at density anomalies c) Largest part of the laser pulse continues along the fiber and a small part is scattered back.*

2.1.2 Resolution, gauge length and strain rate output

The back-scattering of each individual impurity is not powerful enough to be sensed properly by the interrogator. Therefore, for every channel an average is taken of a pre-set segment along the fiber, which is called the gauge length (Dean et al., 2017). Choosing a proper gauge length is always a trade-off between Signal-to-Noise Ratio (SNR) and spatial resolution, since the strain is integrated over this gauge length.

Nowadays, common gauge lengths are ranging from only a few meter to tens of meters, depending on the application. However, theoretically much smaller gauge lengths are possible, approaching centimeter scale (Farhadiroushan et al., 2010). Such small gauge lengths would give access to new applications, such as multicomponent helicoidal sensing (see Appendix A), but are not feasible yet (although the DAS development is going fast). Regarding the selection of a proper gauge length, suitable for the desired application, Dean et al. (2017) describes some relevant rules of thumb. Practically, as the channel output is always an average of a fiber segment spanned by the gauge length, the gauge length acts both as a moving average and low pass filter of the incident signal.

The gauge length must not be confused with the channel spacing, as illustrated in Figure 2 (Dou et al., 2017; Stork et al., 2020). In contrast to the gauge length, the minimum channel spacing is determined by the laser pulse width (Daley et al., 2013). Currently, laser pulse widths in the order of several nanoseconds are achievable, resulting in a minimum channel spacing of 0.25m (considering the two-way travel time) (Dou et al., 2017).

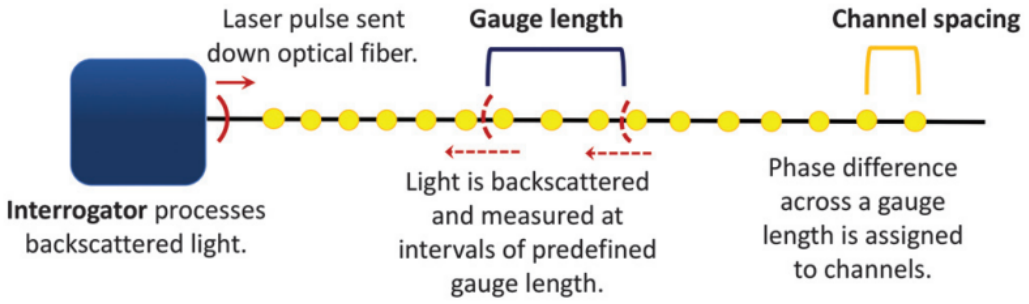

Figure 2: *Conceptual drawing from Stork et al. (2020), clarifying the difference between the gauge length and the channel spacing in a DAS system.*

The output of most DAS systems is the fiber strain rate at every channel with a pre-defined sampling frequency. The maximum sampling frequency is limited to the two-way travel time of the furthest channel. The strain which a fiber segment is subjected to (e.g. a passing seismic wave), is proportional to the light phase change in between two light pulses spanning over the gauge length around that respective channel location (Dean et al., 2017). To be more specific, when the fiber optic cable is at rest, the light pulse back-scattering is random but constant. However, when a fiber part experiences strain, the backscattered phase pattern changes slightly, which is sensed and quantified by the interrogator.

The phase change of the signal itself has a highly non-linear transfer function (Hartog et al., 2014), so the phase change between two fiber locations is taken instead, which are separated by one gauge length (Dean et al., 2017). Hence, this measuring principle results in the averaging effect of the gauge length. The channel location is assumed to be in the middle of the respective gauge length fiber segment.

The relationship between a measured phase change and the corresponding strain at a certain channel x meters from the interrogator unit is described by Lindsey et al. (2020):

$$\epsilon_{xx}\left(t, x_j\right) = \frac{\lambda}{4\pi n L_G \zeta} \Delta\Phi, \tag{1}$$

where ϵ_{xx} is the longitudinal strain, t is time, x_j the scatter location, $\Delta\Phi$ the phase change within one gauge length, $\lambda(m)$ the laser pulse wavelength, n the refractive index of the glass, $L_G(m)$ the gauge length and ζ a scalar multiplicative factor dependent on known material properties (Lindsey et al., 2020). This strain output is sampled with a pre-set frequency resulting in strain rate data.

In real applications, the system output easily becomes substantial in terms of data volume. A sub-meter channel spacing in combination with a sampling rate up to tens of kHz, results in large amounts of data (Stork et al., 2020). Handling these data volumes is not the focus of this project, but is becoming a significant part of modern DAS research, for example described by Stork et al. (2020) and Tejedor et al. (2017).

Additionally, experiments have been conducted regarding the minimum and maximum strain output of a DAS system. According to Lindsey et al. (2020), the minimum amount of measurable strain is related to the injected optical energy. On the other hand, the maximum strain is a topic of debate and can either be related to the elasticity of the fiber (Hartog, 2017), or to the phase unwrapping algorithm (Lindsey et al., 2020). Experiments on this subject were performed by Nap (2020).

2.1.3 DAS coupling & system response

An important assumption related to DAS measurements is the coupling of the fiber with the ground. More specifically, our primary interest is the strain experienced by the hosting ground directly encompassing the fiber, instead of the fiber strain itself. Often it is assumed that the fiber strain is equal to the strain experienced by the host material, but this does not necessarily have to be true. The validity of this assumption under different circumstances is discussed among others by Kuvshinov (2016) and experimentally tested by Nap (2020) and Peterson et al. (2020).

The system response to a very broad range of frequencies is experimentally tested and described by Paitz et al. (2020). The authors of that study show that DAS has relatively flat responses across 17 octaves. For an elaboration on different types of common DAS noise, the reader is referred to Lindsey et al. (2020). Lindsey et al. (2020) give an overview of various phenomena such as common-mode noise (Dou et al., 2017) and optical fading (Gabai & Eyal, 2016).

2.2 DAS: Directionality

2.2.1 Directionality property

A DAS system measures 1D axial strain or the temporal derivative thereof, which means that the incidence angle of an incoming wave has substantial influence on the DAS output (Kuvshinov, 2016; Mateeva et al., 2014; Marijnissen, 2020). More specifically, a DAS system is sensitive to longitudinal inline waves, in contrast to perpendicular (broadside) ground motion, which will result in a smaller light phase change and hence, less observed strain.

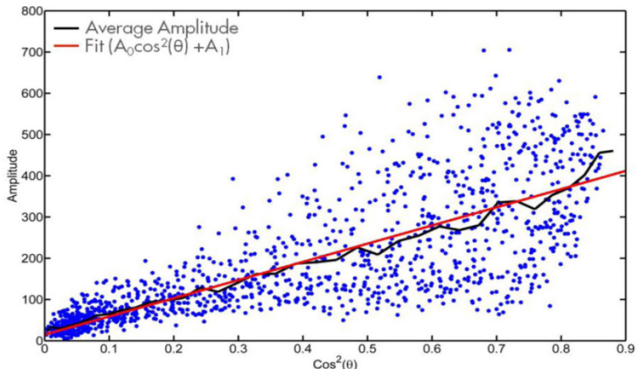

Figure 3: *Plot from Mateeva et al. (2014), illustrating the experimentally determined relation between the angle of incidence α and the measured strain amplitudes of a DAS system.*

A relation between the angle of incidence and the computed fiber strain has been experimentally determined by Mateeva et al. (2014) and is generally accepted to be $cos(\alpha)^2$, where α is the angle of incidence (as shown in Figure 3). Note that this relation is significantly different compared to conventional geophones for which the cosine-relation is not squared ($cos(\alpha)$). Hence, DAS systems are more sensitive to the orientation of the wavefield compared to geophone arrays.

Therefore, especially in the early DAS days, overcoming this broadside insensitivity was prioritized by among others Den Boer et al. (2013) and Den Boer et al. (2015). A popular approach is to use helicoidal fiber shapes in order to 1) increase the total length of inline fiber parts in mul-

tiple directions and 2) avoid complete broadside orientations (Kuvshinov, 2016). Besides that, specific fiber arrays have been proposed, where conventional straight fiber was installed in different shapes like squares (Luo et al., 2020), loops or spheres (Peterson et al., 2020).

However, exploiting the inherent directional sensitivity of DAS systems is gaining significant interest as well and the first signs have been promising. Over the past years, some researchers have established a theoretical and numerical framework for constraining the full strain tensor by exploiting specific helicoidal configurations (Ning, 2019; K. Innanen, 2017b). This DAS multicomponent sensing potential is described further in Appendix A.

2.2.2 Fiber loop: omni-directionality

Due to the DAS directionality characteristic (Section 2.2.1), it is important to consider the orientation of the DAS fiber. This could be ambiguous when the back-azimuth of an incoming wavefield is unknown and hence, the conversion to true amplitudes becomes questionable. This problem can be theoretically tackled by using a fiber loop. A loop has an inherent omni-directional sensitivity in the respective plane, when the loop circumference is equal or (a whole factor) smaller than the DAS gauge length. In such a case, the DAS output of the loop will be completely independent of the wavefield back-azimuth.

Subsequently, this concept can be extended to a fiber sphere configuration, consisting of three orthogonal loops in three spatial directions. Instead of omni-directionality in one plane, as for the loop, a sphere theoretically provides an equal sensitivity for wavefields from all spatial directions. These directional advantages of a fiber loop and sphere have been tested in the field by Peterson et al. (2020), who confirm the omni-directional property of loop and sphere configurations.

In addition to the fiber loop, the helicoidal fiber shape has been extensively proposed for overcoming directionality issues (Den Boer et al., 2015) or deliberately suppressing certain wave types (Kuvshinov, 2016). Although the helicoidal configuration increases the sensitivity to wider incidence angles, it won't provide the same directional independence of a sphere.

2.3 Wavefield gradiometry

2.3.1 Spatial wavefield gradients

In conventional seismic acquisition, it is common to measure one (vertical) or the three translational components of the ground particle displacement, velocity or acceleration (Aki & Richards, 2002). Although 3-component data already provides more information on the P- and S-wavefield compared to only measuring the vertical component (Van Renterghem, 2019), spatial wavefield gradients have the potential to provide additional information useful for overcoming land seismic or seismological challenges (J. Robertsson & Curtis, 2002; Langston, 2007; Maeda et al., 2016; Edme & Yuan, 2016; Schmelzbach et al., 2018). We briefly cover the foundation of wavefield gradiometry, which serves as a theoretical basis for this thesis.

The relation between the stress tensor σ and the strain tensor ϵ_{ij} is given by the elastic constitutive equation (Aki & Richards, 2002):

$$\sigma = \begin{pmatrix} (\lambda+2\mu)\epsilon_{xx} + \lambda(\epsilon_{yy}+\epsilon_{zz}) & 2\mu\epsilon_{xy} & 2\mu\epsilon_{xz} \\ 2\mu\epsilon_{yx} & (\lambda+2\mu)\epsilon_{yy} + \lambda(\epsilon_{xx}+\epsilon_{zz}) & 2\mu\epsilon_{yz} \\ 2\mu\epsilon_{zx} & 2\mu\epsilon_{zy} & (\lambda+2\mu)\epsilon_{zz} + \lambda(\epsilon_{xx}+\epsilon_{yy}) \end{pmatrix}, \tag{2}$$

where λ and μ are the Lamé constants.

Subsequently, this strain tensor ϵ_{ij} is related to the ground particle velocity v_i through (Aki & Richards, 2002):

$$\dot{\epsilon} = \begin{pmatrix} \partial_x v_x & \frac{1}{2}(\partial_y v_x + \partial_x v_y) & \frac{1}{2}(\partial_z v_x + \partial_x v_z) \\ \frac{1}{2}(\partial_x v_y + \partial_y v_x) & \partial_y v_y & \frac{1}{2}(\partial_z v_y + \partial_y v_z) \\ \frac{1}{2}(\partial_x v_z + \partial_z v_x) & \frac{1}{2}(\partial_y v_z + \partial_z v_y) & \partial_z v_z \end{pmatrix}, \tag{3}$$

where the time derivative of ϵ is denoted by a dot.

Equation 3 shows that from closely spaced 3D 3C-velocity measurements, all six independent components from the strain rate tensor can be retrieved (J. O. A. Robertsson & Muyzert, 1999). Usually, the spatial velocity gradients are obtained by a Finite-Difference (FD) approach applied to two closely-spaced 3C-geophones. Although practically straightforward, it is prone to several types of inaccuracies, which is further discussed in Allouche et al. (2017).

By differencing particle velocities over space, the resulting unit will be $\frac{m}{s}/m = \frac{1}{s}$, which describes the local strain rate. Strain rate is also the direct output of a DAS system, which inherently measures the spatial velocity gradient in the axial fiber direction. However, note that these measured axial spatial velocity gradients with DAS are always an average over the pre-set gauge length.

2.3.2 Divergence & Rotation

Following Aki & Richards (2002), the wavefield particle velocity can be described in terms of two potentials: the divergence and curl of the wavefield:

$$\mathbf{v} = \nabla\phi + \nabla \times \boldsymbol{\psi}, \tag{4}$$

where $\mathbf{v} = [v_x, v_y, v_z]^T$.

At first, taking the divergence of the potential results in

$$\nabla \cdot \mathbf{v} = \nabla^2\phi, \tag{5}$$

as the divergence and curl operator cancel each other. The divergence expression of a wavefield can be described by taking the symmetric part of the strain tensor and relates a volume change to the local elastic material properties as follows (Aki & Richards, 2002):

$$\nabla \cdot \mathbf{v} = \partial_x v_x + \partial_y v_y + \partial_z v_z \tag{6}$$

The wavefield divergence is proportional to the pressure (Edme et al., 2018), only scaled by the local material properties either expressed by the Lamé constants or P- and S-wave velocities. An important characteristic of the wavefield divergence is that it only contains the P-wave constituents. No shear energy is present in the divergence as shear strain does not result in a volumetric change (Aki & Richards, 2002; J. Robertsson & Curtis, 2002; Edme et al., 2018).

Secondly, by applying the curl operator to Equation 4, the expression of the wavefield rotation is obtained (Aki & Richards, 2002):

$$\nabla \times \mathbf{v} = \nabla \times \nabla \times \psi \tag{7}$$

This can be described by the anti-symmetric part of the strain tensor and expressed as a vector:

$$\nabla \times \mathbf{v} = \begin{pmatrix} \partial_z v_y - \partial_y v_z \\ \partial_z v_x - \partial_x v_z \\ \partial_x v_y - \partial_y v_x \end{pmatrix} \tag{8}$$

In contrast to the wavefield divergence, the wavefield rotation contains all S-wave energy (Aki & Richards, 2002). Hence, the concepts of the divergence and rotation of a wavefield form the basis of wavefield separation (J. Robertsson & Curtis, 2002).

2.3.3 Free surface condition

Most seismic acquisition takes place at the Earth surface. The implications of such a free surface are a well-known concept as it puts constraints on existing constitutive relations and acts as a full reflector.

The major free surface implication, with regard to wavefield gradiometry, resides in the fact that at the free surface the vertical components of the stress tensor vanish, which results in $\dot{\epsilon}_{iz} = 0$ for

$i = x, y$. Subsequently, this allows us to express the vertical derivatives of the particle velocity in terms of horizontal ones (J. Robertsson & Curtis, 2002; Schmelzbach et al., 2018; Van Renterghem, 2019), as shown below:

$$\partial_z v_x = -\partial_x v_z \tag{9a}$$

$$\partial_z v_y = -\partial_y v_z \tag{9b}$$

$$\partial_z v_z = -\frac{\lambda}{\lambda + 2\mu} \left(\partial_x v_x + \partial_y v_y\right) \tag{9c}$$

With these new vertical gradient expressions, we can rewrite the expressions for the wavefield divergence and rotation at the free surface:

$$\nabla \cdot \mathbf{v} = \frac{2\mu}{\lambda + 2\mu} \left(\partial_x v_x + \partial_y v_y\right) \tag{10a}$$

$$\dot{\omega} = \frac{1}{2} \nabla \times \mathbf{v} = \begin{pmatrix} \partial_y v_z \\ -\partial_x v_z \\ \frac{1}{2}\left(\partial_x v_y - \partial_y v_x\right) \end{pmatrix}, \tag{10b}$$

where $\dot{\boldsymbol{\omega}} = [\dot{\omega}_x, \dot{\omega}_y, \dot{\omega}_z]^T$.

These two expressions show that we can obtain the divergence (scaled by local material properties) and full rotation vector from 3C surface measurements only (J. Robertsson & Curtis, 2002). The geophone cross is a common configuration to retrieve all necessary velocity gradients for practical reasons.

Equations 6 and 10a show that $(\partial_x v_x + \partial_y v_y)$ and $(\partial_x v_x + \partial_y v_y + \partial_z v_z)$ are only scaled by the two Lamé parameters. Hence, they will differ in amplitude, but match in phase. We will refer to $(\partial_x v_x + \partial_y v_y)$ and $(\partial_x v_x + \partial_y v_y + \partial_z v_z)$ as the pseudo-divergence and full divergence, respectively.

3 Field campaign, synthetic model & methodology

In this chapter, we cover three topics in general. First, we describe the Yverdon field campaign in terms of geometry and acquisition. Secondly, we discuss the utilized synthetic model, the corresponding parameters and the synthetic approximations of several Yverdon fiber configurations. Finally, we briefly mention relevant details of the processing workflow.

3.1 Field campaign: Yverdon 2019

The experiments close to Yverdon-les-Bains (Switzerland) were conducted in October 2019. The Distributed Acoustic Sensing (DAS) field test was part of a bigger project funded by Innosuisse (GECOS). This consortium consisted of several parties, such as the seismic service company GEO2X, the University of Geneva, Service Industriels de Geneve and the ETHZ (see Acknowledgements).

3.1.1 Geometry

The test site geometry, including all exotic fiber configurations, is shown in Figure 4. All configurations are part of the same cable, which consists of a forward- and backward fiber. These fibers are attached to the interrogator at one side and connected to each other on the other side. We shortly describe each of the installed configurations illustrated by Figure 4.

- The square: This configuration consists of four sides, each 20m, so that the square sides are either perpendicular or parallel to the source direction (see Figure 4). Each side subsists again of three cables going forth, back and forth, before continuing to the next square side.
- The loops: In the centre, two loops of different size were slightly buried. The short loop has a circumference of 10m and the large loop is twice that size. Both loop configurations consist of a few windings.
- The crosses: In addition to the loops, also cross shapes of 2.5, 5 and 20m length were installed in the centre. A cross configuration involves two orthogonal strings, of which one is inline and one is crossline to the source direction (see Figure 4). The small cross entails 6-10 windings and the largest cross consists of 2-4 windings.
- The bundled mini-cross: As shown in Figure 4, at sides 1, 2 and 3, very small-scale 0.5-1m bundled cross shapes were buried. These configurations encompass many windings, bundled and strapped together.
- The sphere: At side 4, the sphere configuration was installed. It consists of three orthogonal 1.5m loops, which together form a sphere shape (see sphere-picture in Figure 4).
- Geophone cross: For reference purposes, a geophone cross was installed in the centre, incorporating 15 3C-geophones in both inline and crossline direction. Geophone pairs within this cross enable recovering the spatial velocity gradients, which can serve as validation of obtained DAS results. Geophone pair 5-11 (3m spacing) was taken as default, considering the trade-off between inaccuracies originating from the finite difference method and the geophone spacing with respect to the dominant wavelengths.

Note that most configurations were buried closely to the free surface (10-20cm), except for the sphere configuration, which was installed slightly deeper because of the 3D dimensions.

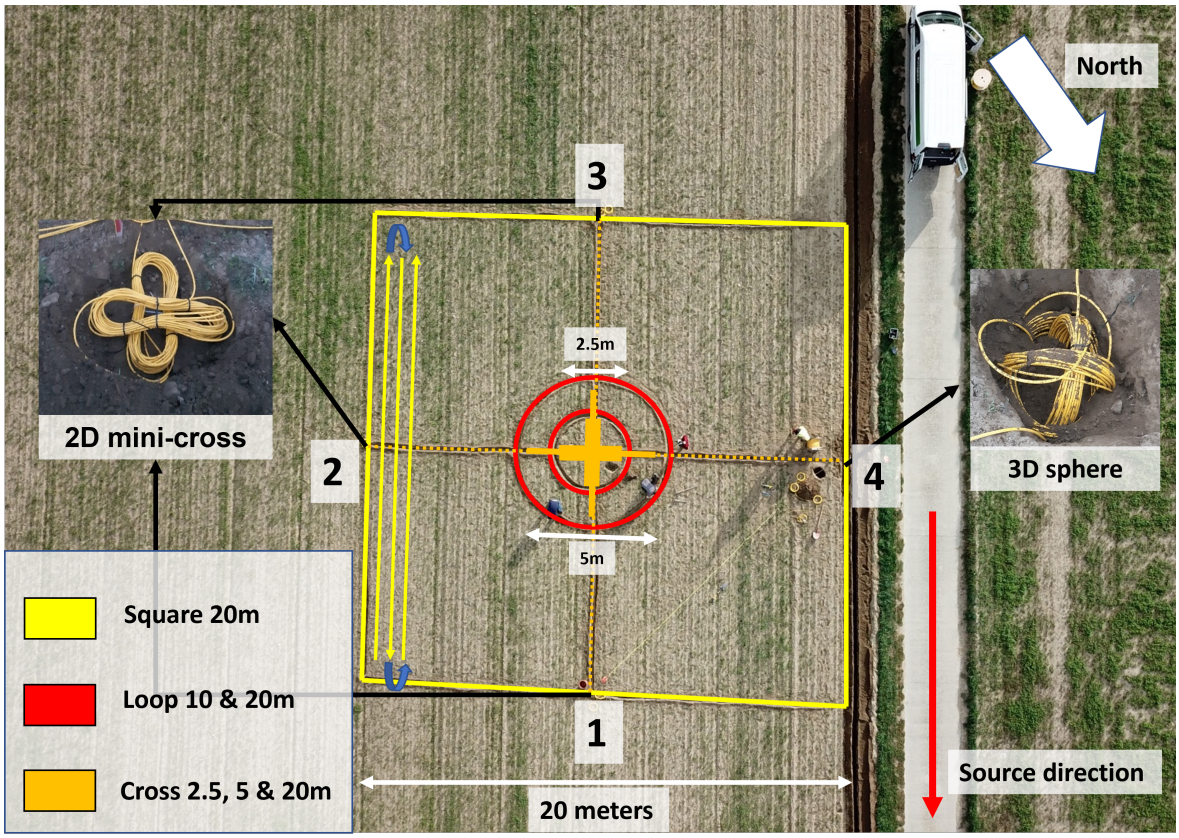

Figure 4: *Overview of the fiber configurations at the test site in Yverdon. The square, the loops and the crosses are denoted by yellow, red and orange, respectively. The four numbers indicate the four sides of the square. Mini-cross configurations were buried at sides one, two and three. At side four, the 3D sphere was located, consisting of three orthogonal loops. The red arrow denotes the direction of the executed shots.*

3.1.2 Acquisition

The DAS measurements were done by a commercially available iDAS v2.4 interrogator from Silixa. The interrogator was connected to the optic fiber cable, which was used for two different objectives simultaneously: 1) one part was shaped into the above-described configurations and 2) the other part was deployed in a long straight trench at different depths (results regarding that data are described and interpreted in Nap (2020) and Nap et al. (2020)). The gauge length was fixed at 10m with a channel spacing of 50cm.

As the receiver configurations were fixed at one position, the source was moved in order to have different offsets. The field test consisted of 167 aligned source positions (offsets 0 - 800m). At some positions, such as position 97, multiple shots were executed for comparison/repeatability purposes. For the source energy, a medium-size vibroseis truck was used, which emitted a 12s sweep (12 - 160Hz).

3.2 Synthetic modelling: Salvus

In order to validate proposed DAS concepts numerically we have used Salvus (Afanasiev et al., 2019), which is originally developed at ETH Zurich and commercially available at the Mondaic platform. Salvus is based on the spectral-element method and has an extensive set of features and applications, focused on numerical wave propagation (Afanasiev et al., 2019).

The spectral-element method (SEM) is part of the Finite Element Methods family and offers certain advantages, such as complex topography discretizations (Fichtner et al., 2013). For an extensive review and explanation of the Spectral Element Method, the reader is referred to Igel (2016).

3.2.1 Basic model & parameters

Our basic 3D model used for the simulations and retrieving the synthetic data is shown in Figure 5. It consists of a 3D volume extending 550m in x-, 100m in y- and 100m in z-direction, enclosed by 62.5m thick absorbing boundary layers, except for the free surface at the top of the model.

In general, the 3D model includes two blocks. On top resides a low-velocity layer with a vertically oriented gradient, which overlies a homogeneous high-velocity base layer (see Figure 5). Figure 5 shows the model structure of the P-wave velocity, but this is identical to the shear velocity and density build. The high-velocity base layer and top layer gradient will generate refracted events and dispersive surface wave behaviour, respectively.

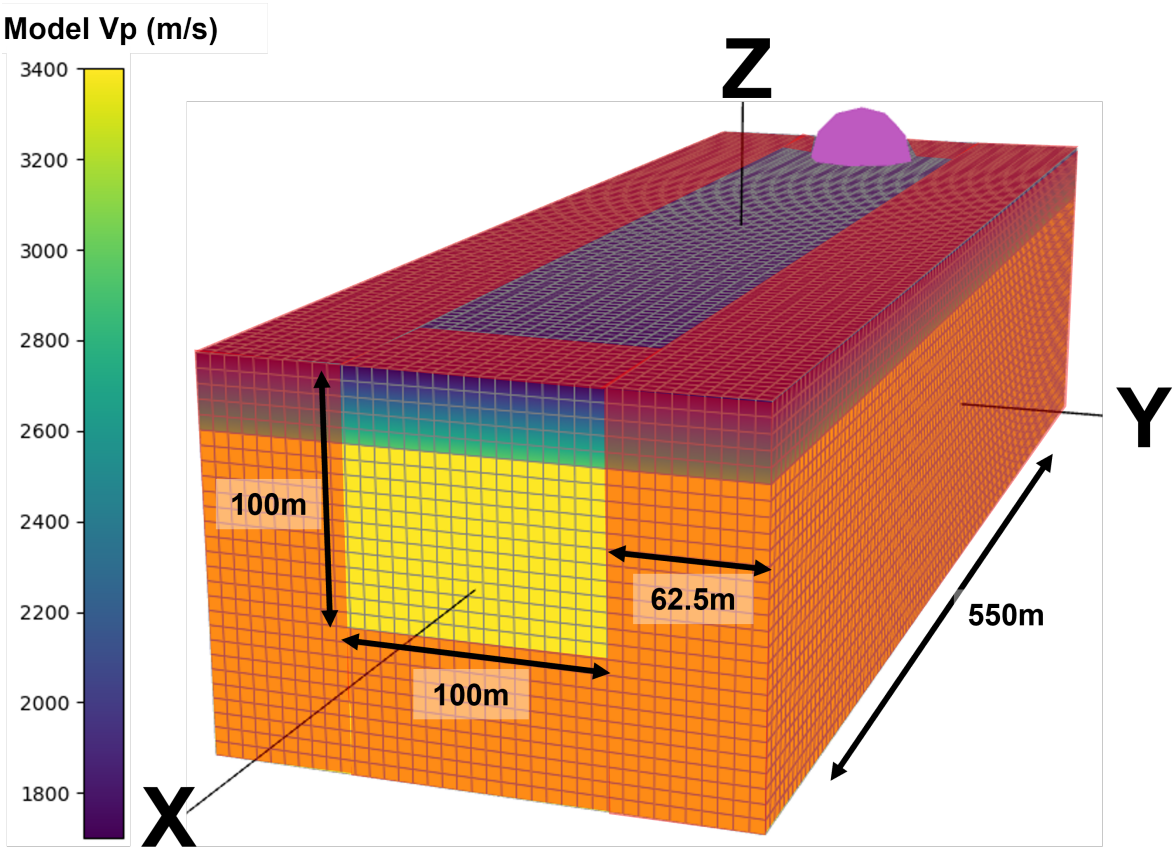

Figure 5: *Schematic overview of the basic 3D model used for the synthetic simulations. The model dimensions in x-, y-, and z-direction are 550m, 100m and 100m respectively. The model volume is surrounded by absorbing boundary layers of 62.5m thick, denoted by transparent red, except for the free surface at the top. The high velocity base layer is illustrated by yellow and is overlain by a lower velocity top layer containing a velocity gradient with depth. The vertical source is characterized by the purple sphere.*

The source is defined as a vertical vector force, exerted at the surface. Important model parameters, such as the element length and time step, were automatically determined by meeting the standard numerical criteria. The constant model parameters for all standard simulations are summarized in Table 1.

Table 1: *Summary of the constant 3D model parameters used for the numerical simulations.*

Model parameters	
Dimensions x, y and z	550m x 100m x 100m
Thickness top layer	31m
Absorbing boundary layers	62.5m
Element length	6.20m
Central frequency	20Hz
$V_{P,min}$ - $V_{P,max}$	1700 - 3400 m/s
$V_{S,min}$ - $V_{S,max}$	500 - 1000 m/s
ρ_{min} - ρ_{max}	1500 - 2700 kg/m^3

3.2.2 Optional model features & configuration approximations

To investigate proposed fiber configurations synthetically and to verify data observations, we added one or more of the following features to the standard model (Section 3.2.1). We describe the most relevant ones.

1. The road. The first field data analysis showed signs of a significant effect of the adjacent road (crossline propagating wavefield). Therefore, we created a synthetic high-velocity road element, which involves an elongated feature, stretching over the entire x-range and being only one element deep and wide. We assigned the same properties to this synthetic road as the high-velocity base layer, resulting in a large contrast with the surrounding top layer.

2. Removal of velocity gradient. To examine sensitivity-related topics, the velocity gradient could be removed, resulting in a homogeneous low-velocity layer overlying a high-velocity base.

3. Approximations of DAS configurations. We approximated the most relevant DAS configurations in the field by specific velocity- and strain receiver arrangements in Salvus. We briefly describe these synthetic configurations below.

    - The crosses. We approximated the DAS crosses for the two orthogonal strings separately. We approached both strings by placing 41 receivers along the entire cross string length and averaging their axial strain components.
    - The loops. We approximated the loops by placing 32 receivers in a ring. We converted their strain output in x- and y-direction to the local axial strain by applying the following relation: $\sin^2\theta + \cos^2\theta = 1$, where θ is the angle with one of the spatial axes. Subsequently, we averaged the converted strain values to obtain one loop strain value.
    - The sphere. We found that for small loops with sub-meter radii, a 4-receiver approximation is sufficient (considering our model parameters). A validation of this assumption can be found in Appendix B. We used this 4-receiver loop approximation to construct the synthetic sphere (diameter 0.50m), consisting of three loops in the three orthogonal planes.

    Note that we placed the synthetic configurations 10m from the middle (crossline), to avoid potential overlap with the synthetic road.

3.2.3 Output

The Salvus simulations generate two types of data output.

- The synthetic receiver data. This is stored as h5-files (ADSF) containing all receiver information and data. Each receiver provided nine traces, namely three for the x-, y- and z particle velocities and six for the independent strain components.
- Wavefield snapshots. Salvus saves snapshots of the simulated wavefield every x time steps. This proved useful for analyzing the wavefield development at the surface.

3.3 Data processing

For the data processing of both the synthetic and field data, we mostly used Matlab (version 2019b) and the corresponding functionalities. Additionally, the Matlab function package Seislab3.02 was used extensively for many basic seismic processing steps, such as reading data, trace computations and applying standard filters.

3.3.1 Synthetic data

The synthetic h5-data files were first converted to segy-files for further processing steps. The receiver traces contained the velocity and strain information for each time step. To obtain the same unit as the DAS field data, namely strain rate, we applied a central difference time derivative operator on the synthetic strain recordings.

3.3.2 Field data

The field recordings were correlated with the source sweep and stored as separated DAS and geophone segy-files. When not specified, the field data shown in this report has been filtered with an Ormsby frequency filter omitting frequencies outside the 7-160Hz bandwidth.

In this study, we often compare obtained DAS and geophone retrieved results. Frequently, there is a significant scalar amplitude factor between both receiver gathers. In order to make the comparison more convenient in terms of phase and relative energy distribution, we corrected for this. We computed the amplitude correction scalar from the ratio of the norms of both trace matrices. Subsequently, we applied the computed correction scalar to the entire DAS trace matrix to equalize the average energy with the geophone data. The amplitude correction scalars are always mentioned when applied, to indicate the overall amplitude difference between the DAS and geophone results.

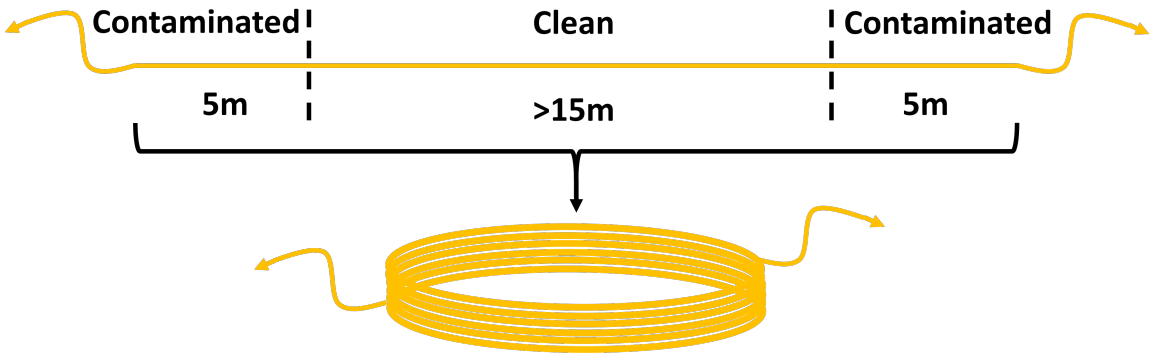

Figure 6: *Conceptual drawing illustrating the concept of clean/contaminated channels and configuration windings. This illustration shows the case of a fiber coil/loop, but the same concept applies to the other fiber shapes as well.*

The DAS channel output is an average over the encompassing gauge length (Section 2.1.2) and is pre-set at 10m for this field campaign (Section 3.1.2). Hence, the first and last 5m (10 traces) of cable within a configuration is contaminated with external strain rate information, which is illustrated in Figure 6. Therefore, we always subtract the first and last 10 traces of a DAS configuration and consider the remaining traces as 'clean'.

In order to have enough clean channels present in a configuration, the cable needs to be coiled or winded in the specific configuration shape (see Figure 6). As the gauge length is equal to one or many configuration windings, the configuration channels were stacked (i.e. we took the mean of the clean traces). This results in one configuration trace representing the entire DAS loop, cross or sphere. As discussed in Section 2.3.1, the DAS system output (strain rate) is equal to the local spatial velocity gradient(s).

To summarize, the smaller the size of the configuration, the more windings the configuration must entail, but the more local the measured spatial velocity gradients are.

4 Data quality of DAS configurations

This chapter is the first of four chapters describing, discussing and comparing the obtained synthetic and field results. Chapter 5, 6 and 7 are all focused on a specific attractive potential of the proposed Distributed Acoustic Sensing (DAS) configurations. However, we first start with this chapter on the data quality for two reasons. First, it largely shows the validity of the results presented in the next chapters and second, it can be used as a reference to explain specific observations at a later stage.

In this chapter we start with discussing the utilized data quality indicators. Subsequently, the shot-to-shot repeatability results of the configurations are presented by means of the data quality indicators. Finally, the impact of the nearby road is examined.

4.1 Shot-to-shot repeatability indicators

In order to assess the data quality of the different DAS configurations and to choose the optimal geophone FD-pairs, their shot-to-shot repeatability has been examined and evaluated quantitatively. We quantified the trace similarity of 18 repeated shots by making use of three indicators, namely the Normalized Root Mean Square (NRMS), the Coherence and Normalized Standard Deviation (NSD). We give a brief overview of those quantifying methods below. For a more extensive description of these methods and DAS data quality assessment in general, the reader is referred to Nap (2020).

In our case, we used 18 repeated shots at shot location 97, which were all compared with each other. For every DAS configuration, this results in 153 unique trace-to-trace comparisons. Note that we used the mean configuration trace, as described in Section 3.3.2, and a sliding time window.

In general, similarity values between repeated shots can be regarded as an important indicator for data quality, as the repeatability of a DAS configuration or geophone can be linked to for example fiber/geophone coupling (Nap, 2020).

4.1.1 Normalized Root Mean Square (NRMS)

The NRMS is a time-domain method, which is sensitive to both amplitude and phase differences between two compared seismic traces (Kragh & Christie, 2002).
The NRMS is computed by (Kragh & Christie, 2002):

$$NRMS\left(a_t, b_t\right) = \frac{200 \cdot RMS\left(a_t - b_t\right)}{RMS\left(a_t\right) + RMS\left(b_t\right)}, \tag{11a}$$

where the RMS is defined as:

$$RMS\left(x_t\right) = \sqrt{\frac{\sum_{t_1}\left(x_t\right)^2}{N}}, \tag{11b}$$

where N is the number of time samples in the interval $t_1 - t_2$ and a_t and b_t are the two compared seismic traces within this time window (Nap, 2020).

The computed NRMS value is given in percentages from 0% to 200%, where a lower percentage denotes more similarity than a high percentage. The NRMS computation results in 0% when the compared traces are completely similar, 141% for random noise and 200% for anti-correlated traces.

4.1.2 Coherence

The Coherence between two traces is computed in the time-domain as well, but is only sensitive to phase information (Nap, 2020; Kragh & Christie, 2002; White, 1980). The coherence is computed as follows (Nap, 2020):

$$\text{Coherence } \left(a_t, b_t\right) = \frac{a_t \cdot b_t}{\sqrt{a_t^2 \cdot b_t^2}} \tag{12}$$

The Coherence scale ranges from 1 to -1, where a value of 1 indicates complete similarity and -1 anti-correlation.

4.1.3 Normalized Standard Deviation (NSD)

In contrast to the previous two methods, the NSD is a frequency-domain approach and quantifies the shot-to-shot variation per frequency (Nap, 2020). The NSD value is calculated by:

$$NSD = \frac{\sigma}{X}, \tag{13}$$

where σ represents the standard deviation of the shot-to-shot data variation per frequency and X the corresponding mean value. Hence, a low NSD denotes little variation compared to the mean and translates to the shot repeatability.

4.2 Field data

We've structured this section based on the time- and frequency domain. For the FD geophone results, we took an average of all FD geophone pairs, excluding three significantly less functioning ones. The individual FD geophone pair results are presented in Appendix C.1. To all data, we applied a 7-160Hz bandpass filter before analysis and visualization.

4.2.1 Time domain

The shot-to-shot NRMS results of the Yverdon field configurations are shown in Figure 7. The relevant features in the Coherence results are largely similar, so this is presented in Appendix C.2.

We make a few observations based on the NRMS results in Figure 7.

- We notice that large amplitude events exhibit low NRMS-values and hence, high repeatability/quality, except for the high frequency refracted early arrivals.
- We see a distinct NRMS-repeatability difference between the DAS configurations for almost all times. We observe that the loop configuration (blue) shows the best repeatability results followed by the cross (red). Significantly worse NRMS values are computed for the sphere (purple), mostly for lower frequency arrivals. Furthermore, especially the mini-cross (cyan) exhibits clearly unacceptable repeatability values. The sphere and mini-cross have in common that they consist of bundles of cable, intuitively resulting in a questionable coupling of the inner bundle cables (further discussed in Chapter 6). Apart from the DAS configurations, it is surprising that the NRMS-values for the FD geophone configuration are relatively poor compared to the DAS loop and cross. Note especially the relatively lower geophone performance for the high amplitude first break.
- We observe that in general the large loop and large cross show better NRMS values compared to their smaller equivalents. We expect the origin of this difference to be similar to the lesser 2D mini-cross and sphere results, as the smaller loop and cross encompass more windings (Section 3.3.2).

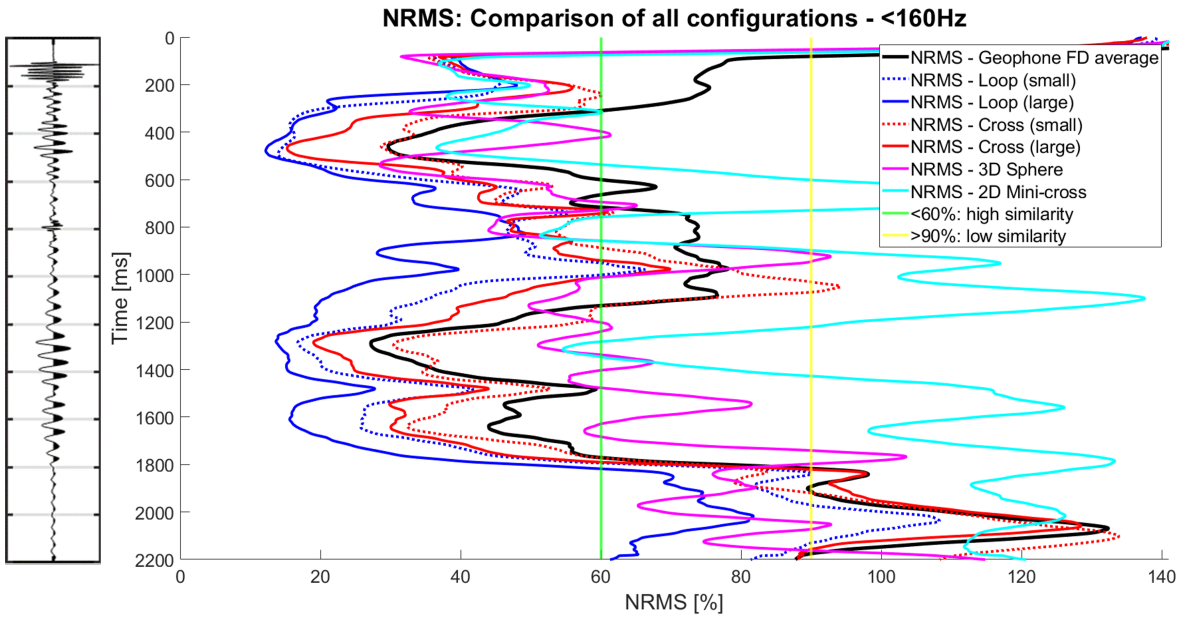

Figure 7: *Plot of the shot-to-shot NRMS results of all field configurations for shot 2-18 at shot location 97. The vertical green and yellow line denote the defined boundaries of high and low similarity (Nap, 2020). On the left, a trace of the average FD geophone result is added as signal reference.*

4.2.2 Frequency domain

We retrieved the configuration frequency spectra of the 18 repeated shots and visualized them in two different ways.

First, we computed the spectrum average over the 18 shots for all configurations, which is presented in Figure 8. The spectra were not normalized to enable true measured amplitude comparison. From Figure 8, we make three main observations.

- The sphere and in particular the mini-cross (the bundled configurations) show significantly smaller amplitudes, especially for the lower frequencies. We expect that the cable bundling has a large damping effect on the inner cables, which results in smaller amplitudes. Especially the two amplitude peaks at 20 and 30Hz, clearly visible in the loop, cross and geophone spectra, are completely absent in the sphere and mini-cross spectra.
- For the lower frequencies (20-30Hz), the loop configurations show higher amplitudes compared to the crosses. This is the opposite for the higher frequency content (refracted waves, 80Hz), which is better sensed by the cross configurations.
- In the 80Hz-range we notice significantly larger amplitudes for the small loop and cross, compared to their larger versions. The influence of the loop/cross size, related to the dominant wavelength/frequency, will be discussed in the Chapter 5.

Secondly, we utilized the same spectra to calculate the configuration NSD-curves over the entire frequency bandwidth. These results are demonstrated in Appendix C.3, as most configurations show a similar trend for the relevant frequency ranges. One exception is the FD geophone configuration, which exhibits remarkably high NSD values for the refracted waves (80Hz). These poorer FD geophone repeatability results for the high-frequency refractions are also clear in the NRMS-results in Figure 7, which would suggest relative difficulties for the FD geophone configuration regarding the refracted wave arrivals.

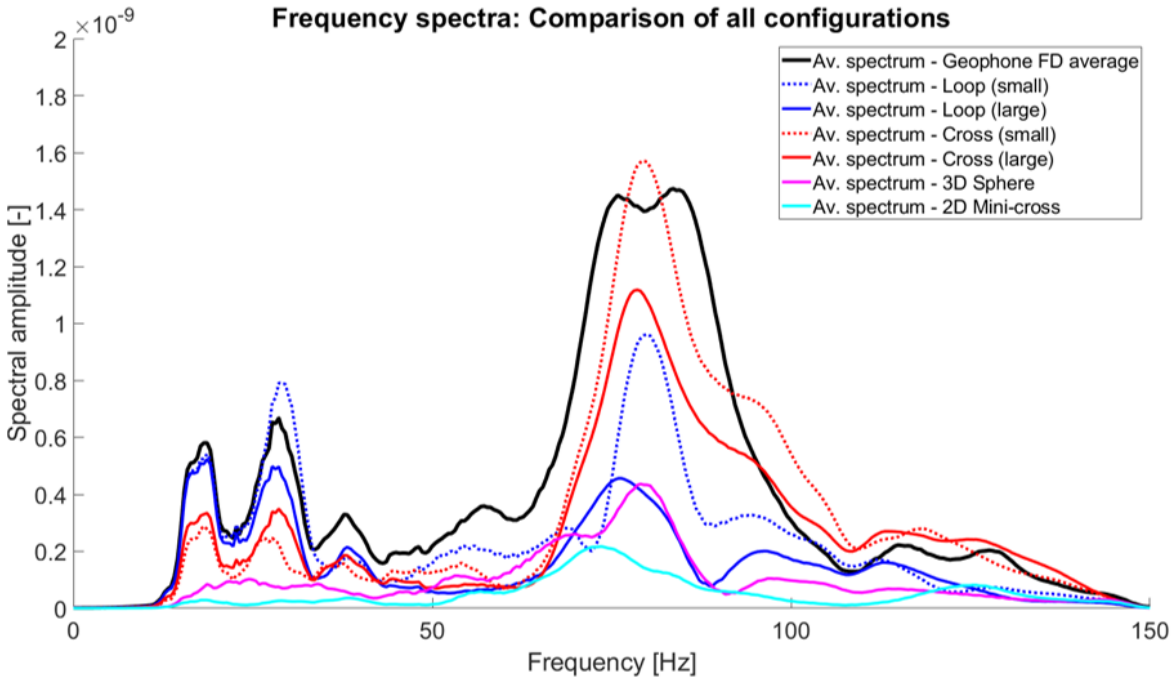

Figure 8: *Plot of the average frequency spectra of the field configurations for shot 2-18 at shot location 97. The mean amplitudes of the 18 shots (y-axis) are plotted against the frequencies on the x-axis. These spectra are without normalization for comparison reasons.*

4.3 Impact road

As shown in Figure 4, the road plays a prominent role at the Yverdon test site for two reasons. First of all, the vibroseis shots are executed on the road and secondly, the road is close to the configurations. Hence, an effect of the road on the field data is likely, due to the material property contrast.

The clearest indication of the road in the field data are the surprisingly large strain rate amplitudes in the crossline (y-)direction for both the early and late arrivals, displayed as red in Figure 9. Considering the aligned source positions in x-direction and the theoretical behaviour of body and surface waves, we would only expect little energy in the crossline $\partial_y v_y$-component. However, a strong $\partial_y v_y$-component is present in the data of the DAS loop, cross, sphere and geophone cross (see Figure 9).

To explain this strong crossline strain rate component in the field data, we added a 'road' to the synthetic model (see Section 3.2.2) to simulate the impact of such a contrasting body on nearby recordings. The results are presented in Appendix C.4 and clearly show a very considerable effect of the synthetic road. The impact is most substantial for the base layer refractions, indicated by very significant crossline strain (y-direction) amplitudes. This crossline strain is probably induced by scattering of the refractions at the road body, due to the high property contrast.

Although present in field data (see Figure 9), we do not notice major crossline strain (y-direction) for the surface waves in the synthetic data. However, we recognize that the synthetic road changes the waveform of the inline strain component (x-direction). This is presumably related to the synthetic source being on top of the road feature, as this results in an extra wavefield conversion from the road to the surrounding low-velocity model elements.

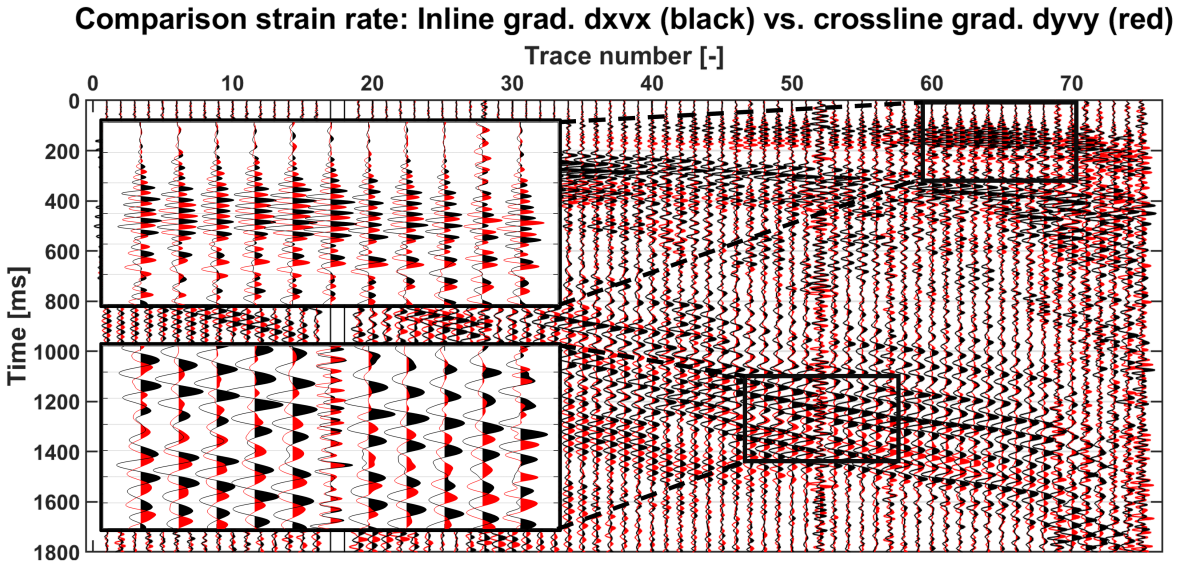

Figure 9: *Comparison of the strain rate in x- (black) and y-direction (red), $\partial_x v_x$ and $\partial_y v_y$ respectively. The spatial gradients are obtained by a FD geophone approach of pair 5-11 (3m spacing) in both directions. The offset of the first channel is 71m increasing with approximately 2.80m every trace (moving source). The data for this comparison has been bandpass filtered by an Ormsby-filter [7-60Hz] and an AGC is applied with a 1200ms window length.*

4.4 Summary

We have analysed the shot-to-shot repeatability and sensitivity of the field configurations in the time domain (NRMS & Coherence) and frequency domain (frequency spectra & NSD). The NRMS- and coherence data show very similar results, which suggests that the relative repeatability performance of the configurations mostly differs in terms of phase and not amplitude. Regarding the DAS configurations, there is clear difference between the larger-scale loops & crosses and smaller-scale sphere & mini-cross configurations. The bundled cable configurations 1) exhibit considerably poorer shot-to-shot repeatability and 2) are significantly less sensitive to especially the lower frequencies.

Apart from the repeatability results, we observe a probably significant effect of the adjacent road in the field data. Therefore, we have simulated a similar contrasting feature using Salvus, which confirms substantial crossline scattering of the refractions.

5 Loop & Cross: Divergence in the horizontal plane

We structure this chapter as follows. First, we discuss the theoretical potential of both the fiber cross and loop in terms of measuring the pseudo-divergence (Section 2.3.3). In the second part, we present the synthetic and field results of the cross and loop configuration, where the synthetic results can serve as validation of our theoretical expectations. Finally, we focus on the effect of the configuration size with regard to the wavefield frequency/wavelength and discuss the sensitivity of the loop and cross with respect to Rayleigh and Love surface waves.

5.1 Theoretical potential

The wavefield divergence is defined as the summation of the symmetric part of the strain tensor and can be expressed at the free surface by the two horizontal gradients, scaled by some parameters representing the local material properties (see Section 2.3.3). Therefore, measuring the divergence in the horizontal plane is already valuable.

In this thesis, we propose two fiber configurations to retrieve the pseudo-divergence: a fiber cross and a fiber loop.

A fiber cross consists of two orthogonal strings in the horizontal plane (x and y). Hence, elongation or shortening of the fiber strings provide directly $\partial_x v_x$ and $\partial_y v_y$, which are summed to obtain the pseudo-divergence.

The fiber loop responds to a change in circumference (observed fiber strain), which is conceptually illustrated by Figure 10. The circumference variation is related to the loop radius and hence, the loop is equally proportional to $\partial_x v_x$ and $\partial_y v_y$. Because of this implicit omnidirectional property, $\partial_x v_x$ and $\partial_y v_y$ can not be distinguished separately. Therefore they can only be expressed as their sum $(\partial_x v_x + \partial_y v_y)$, which is proportional to the pseudo-divergence by a factor of two. This is factor is related to the fact that the observed loop fiber strain is expressed by $\frac{2\pi(r+\Delta r)-2\pi r}{2\pi r}$ and hence, $\frac{\Delta r}{r}$, which should be $\frac{\Delta r}{r} + \frac{\Delta r}{r}$ to match the pseudo-divergence definition (Section 2.3.3).

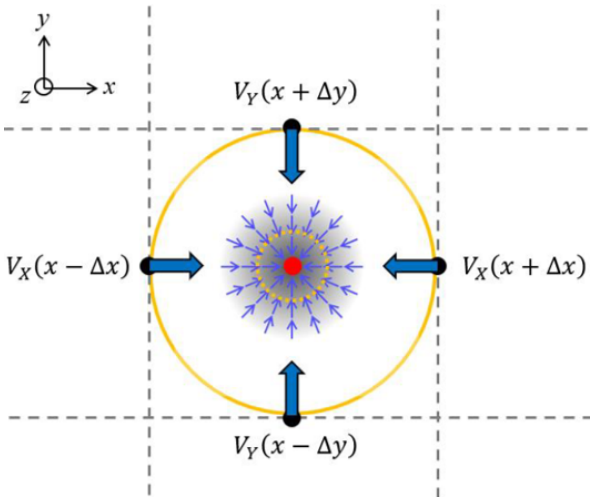

Figure 10: *Conceptual drawing from Edme et al. (2021) illustrating a pseudo-divergence measurement by a 3C-geophone (blue) and fiber loop (yellow) configuration. The blue arrows denote the four 3C-geophone measurements which together provide the pseudo-divergence by Finite Difference (FD). The yellow fiber loop is sensitive to the pseudo-divergence by measuring the strain induced by shortening or elongation of the fiber loop circumference.*

Regarding the surface wave sensitivity of the loop and cross configuration, we consider Rayleigh and Love waves, each with their own characteristics (Rind & Down, 1979). An elegant way to separate both wave types is by exploiting the exclusive presence of Rayleigh and Love waves in the divergence and vertical component of the rotation, respectively Maeda et al. (2016). Hence, the loop and cross configuration are theoretically only sensitive to Rayleigh waves, which we verify numerically in Section 5.5.

5.2 Synthetic data

Figure 11 displays the comparison of the synthetic pseudo-divergence obtained by the large synthetic loop (circumference 20m) and the local reference, retrieved from direct Salvus strain measurements (see Chapter 3 for details). The similar comparison for the smaller synthetic 10m-loop is presented in Appendix D.1.

In general, we observe a solid match between the obtained synthetic loop results and the local Salvus reference. Hence, these results validate the theoretical concept of the pseudo-divergence retrieval from a Distributed Acoustic Sensing (DAS) loop configuration. However, focusing on the surface wave window (Figure 11), we recognize a small amplitude misfit (5-10%) with the pseudo-divergence reference. The surface wave misfit stems from the size of the 20m-loop configuration (diameter: 6.38m), relative to the surface wavelength, which is further discussed in Section 5.4. Note that the loop factor-of-2 correction (Section 5.1) has already been applied in Figure 11 and Appendix D.1.

We analysed the synthetic cross configuration in a similar way and the pseudo-divergence comparison of the cross and reference results is identical to the synthetic loop. The fit for both the 2.5m- and 5m-cross is solid, although we notice the same slight surface wave amplitude misfit for the 5m-cross. For completeness, the synthetic pseudo-divergence comparisons of the 2.5m- and 5m-cross are presented in Appendices D.2 and D.3.

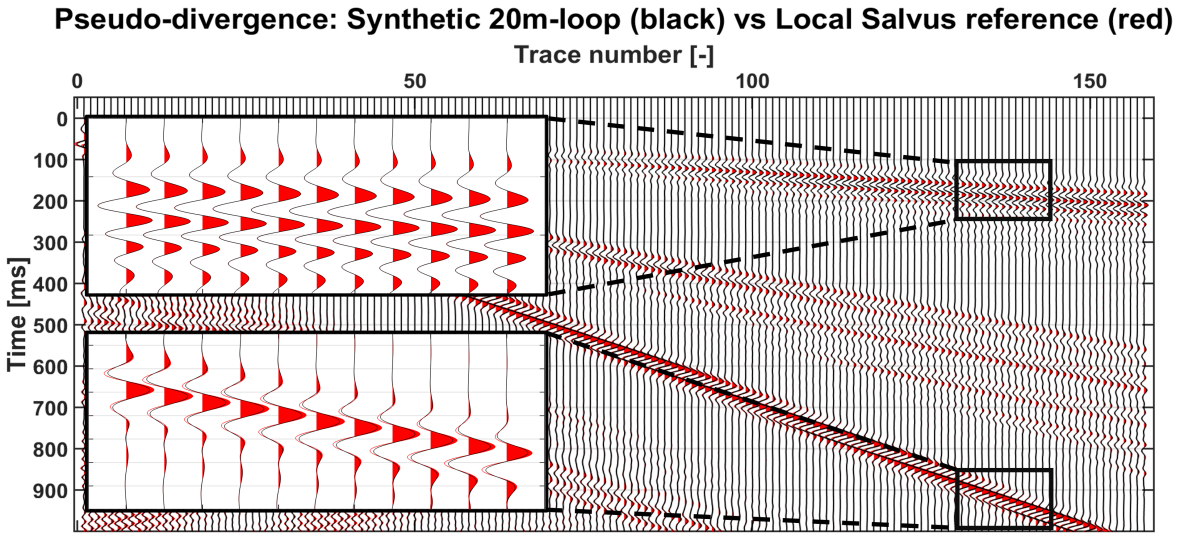

Figure 11: *Comparison of the synthetic pseudo-divergence obtained by the large synthetic 20m-loop (black) and the local pseudo-divergence reference (red). The match is solid, except for a slight amplitude misfit for the surface waves. The loop diameter is 6.38m. An AGC with a 300ms window length has been applied. The two boxes display zoomed windows of the early and late arrivals (refractions and surface waves respectively). Further information regarding the synthetic model parameters can be found in Section3.2. The plotted traces have offsets ranging from 30-500m.*

5.3 Field data

5.3.1 Yverdon cross configurations

The pseudo-divergence results from the 5m- and 2.5m-field cross are presented in Figure 12 and Appendix D.4 respectively. Both plots show a comparison between the obtained DAS cross results in black and the FD geophone retrieved pseudo-divergence in red (pair 5-11, 3m spacing). The FD geophone configuration acts as a reference in this case, considering it is a proven concept (J. Robertsson & Curtis, 2002). However, we showed in Chapter 4 that the DAS loop and cross configurations are

exceeding the FD geophone performance in terms of shot-to-shot repeatability.

The match between the DAS cross and FD geophone results is great, with regard to the pseudo-divergence phase and relative energy distribution, as shown in Figure 12 and Appendix D.4. The main events are present in both receiver gathers and are generally well-resolved by the DAS cross. However, as discussed in Section 3.3.2, a scalar amplitude correction has been applied to the DAS results. The correction factors are 1.60 and 1.78, for the large 5m- and small 2.5m-cross respectively, which is recognizable as well from the frequency spectra in Figure 8. The exact reason for this reduced overall DAS sensitivity is currently open for discussion, but cable coupling issues are most probable. This can be argued by noticing the slightly higher correction factor for the 2.5m-cross, which entails more windings.

The presented results in Figure 12 and Appendix D.4 are high-cut at 60Hz. As discussed above, for these frequencies the match between the DAS cross and FD geophones is solid. However, the refracted waves (early arrivals) are mostly present in a higher frequency band (80Hz), as shown in Appendix D.5. For this high-frequency refraction event, the DAS cross - FD geophone match is significantly worse in terms of both phase and relative amplitudes. The refraction event as resolved by the DAS cross is much sharper compared to the FD geophone output.

The same feature is present in the results of the 2.5m-cross, which has almost equal dimensions compared to the FD geophone configuration (3m spacing). Hence, it is unlikely that the refraction misfit is due to a different configuration size - wavelength effect. A more plausible explanation is supported by Figure 7 displaying that the FD-geophones have major difficulties resolving the high-frequency early arrivals (Section 4.2.1). This implies that the obtained pseudo-divergence results obtained by the DAS cross are actually more reliable compared to the FD geophone output.

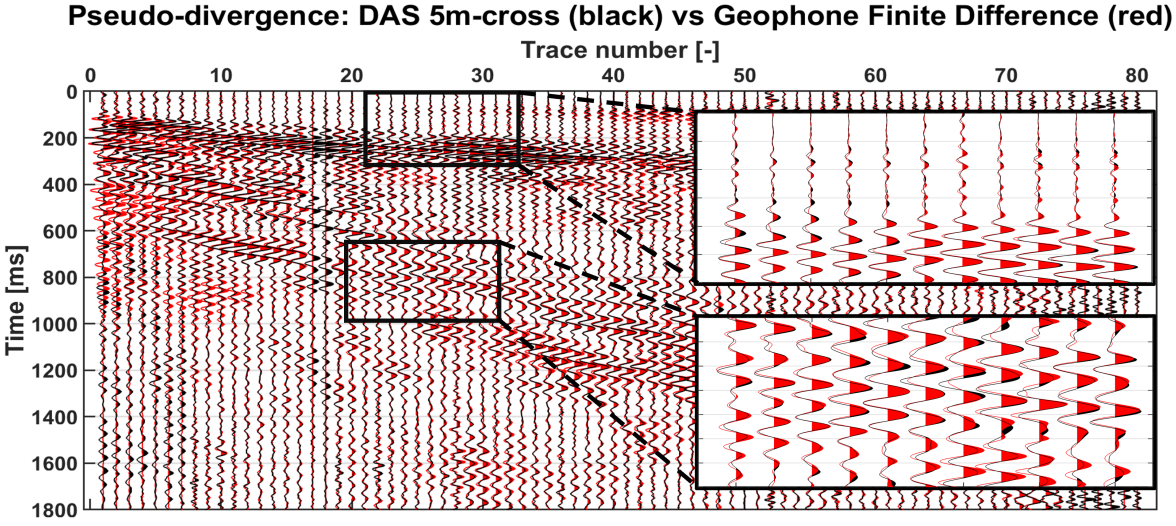

Figure 12: *Comparison of the pseudo-divergence obtained by the 5m-DAS cross (black) and geophone pair 5-11 (red). Generally, the match is solid in terms of phase and relative energy distribution. The geophone spacing in both horizontal directions is 3m. The offset of the first channel is 71m increasing with approximately 2.80m every trace (moving source). The data for this comparison has been bandpass filtered by an Ormsby-filter [7-60Hz] and an AGC is applied with a 1200ms window length. The DAS cross amplitudes have been multiplied with a factor of 1.60 to equalize the norms of both gathers.*

5.3.2 Yverdon loop configurations

The same comparison, now applied to the DAS loop, is demonstrated in Figure 13 and Appendix D.6 for the 20m- and 10m-loop respectively. The same FD geophone pair 5-11 (3m spacing) is used as a reference.

The DAS loop - FD geophone match (for frequencies below 60Hz) is similarly adequate, despite a minor phase difference present in both the large and small loop results. This minor relative phase shift is remarkable as both the loops and FD geophone configuration share the same centre. Compared to the cross configurations, the amplitude correction factor (Section 3.3.2) is significantly smaller (20m-loop: 1.43 & 10m-loop: 1.22). This factor difference between the loop and cross configurations is possibly related again to the smaller amount of loop windings (compared to the cross).

Additionally, we recognize a discrepancy between the correction scalars of the two differently-sized loops. A potential explanation could stem from the loop dimension with respect to the wavelength. As shown in section 5.2, this effect already induced smaller surface wave amplitudes for the synthetic 20m-loop, which would result in a larger correction factor. However, note that the subsurface geometry and synthetic velocities of the Salvus model and Yverdon test site are probably different. Hence, the impact of the configuration size with respect to the wavelength will be different as well.

The 20m-loop - FD geophone comparison including the higher frequencies is shown in Appendix D.7. The refracted event mismatch between the DAS loop and FD geophone configuration is similar to the fiber crosses. However, the DAS loop refraction amplitudes are now smaller than the FD geophone output, which is the opposite case for the crosses.

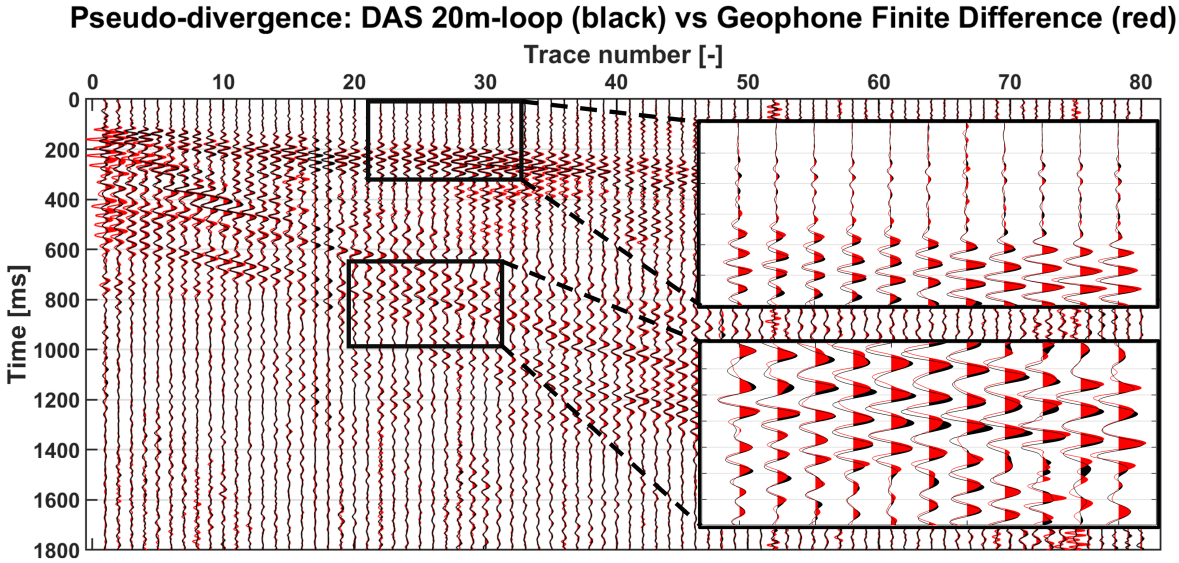

Figure 13: *Comparison of the pseudo-divergence obtained by the large 20m-DAS loop (black) and geophone pair 5-11 (red). The match is decent in terms of phase and relative amplitudes, except for a minor overall phase shift. The loop diameter is 6.37m and the geophone pair is spaced by 3m. The offset of the first channel is 71m increasing with approximately 2.80m every trace (moving source). The data for this comparison has been bandpass filtered by an Ormsby-filter [7-60Hz] and an AGC is applied with a 1200ms window length. The DAS cross amplitudes have been multiplied with a factor of 1.43 to equalize the norms of both gathers.*

5.4 Configuration dimensions vs wavelength

In the synthetic 20m-loop (diameter 6.37m) and 5m-cross results, a clear effect of the configuration size with respect to the wavelength was already recognizable for the surface waves. The wavelength and frequency are proportional to each other by $\lambda = \frac{v}{f}$ and hence, the relation with the loop/cross size could be expressed in terms of both. As the configuration size is given in the spatial dimension (m), expressing the influence in terms of wavelength we find most convenient.

The maximum FD geophone spacing for obtaining acceptable spatial wavefield gradients has been

generally accepted to be between 10% and 20% of the target wavelength (Allouche et al., 2017; Edme & Yuan, 2016; Schmelzbach et al., 2018). For longer DAS fiber arrays, the same applies with respect to the gauge length, which acts as a moving average filter (Paitz, 2021). However, considering the dimensions of the Yverdon configurations and the fact all clean channels are stacked to obtain one pseudo-divergence trace, we primarily look at the configuration size as the major variable.

In order to investigate the effect of the DAS loop & cross size on the synthetic pseudo-divergence results, we implemented many differently-sized loop and cross configurations in the Salvus model (Section 3.2.1). These synthetic loop and cross sizes range from 1 - 20m in diameter. Considering the model velocities and (wave type dependent) frequencies, the dominant wavelengths are in the order of 80-90m for the refractions and 20-25m for the surface waves. To quantify the similarity between the computed pseudo-divergence cross & loop traces and the local Salvus reference, we applied the NRMS-approach (Section 4.1).

The NRMS-results for the loop, cross and FD geophone configuration are presented in Figure 14a distinguishing between refracted and surface waves. Figure 14b shows the pseudo-divergence trace comparison of the 20m-cross and the local Salvus reference. We point out the most relevant features.

- Over the complete configuration size range, the refracted events are much better resolved, exhibited by the low NRMS-values in Figure 14a and the decent signal fit in Figure 14b. This stems from the larger refraction wavelength (80-90m) due to the higher P-wave velocity. Additionally, the refracted arrivals have small (vertical) incidence angles resulting in even larger apparent wavelengths at the surface. Hence, for obtaining pseudo-divergence data from small incidence angle P-wave events, larger cross/loop sizes do not pose wavelength-dependent problems.

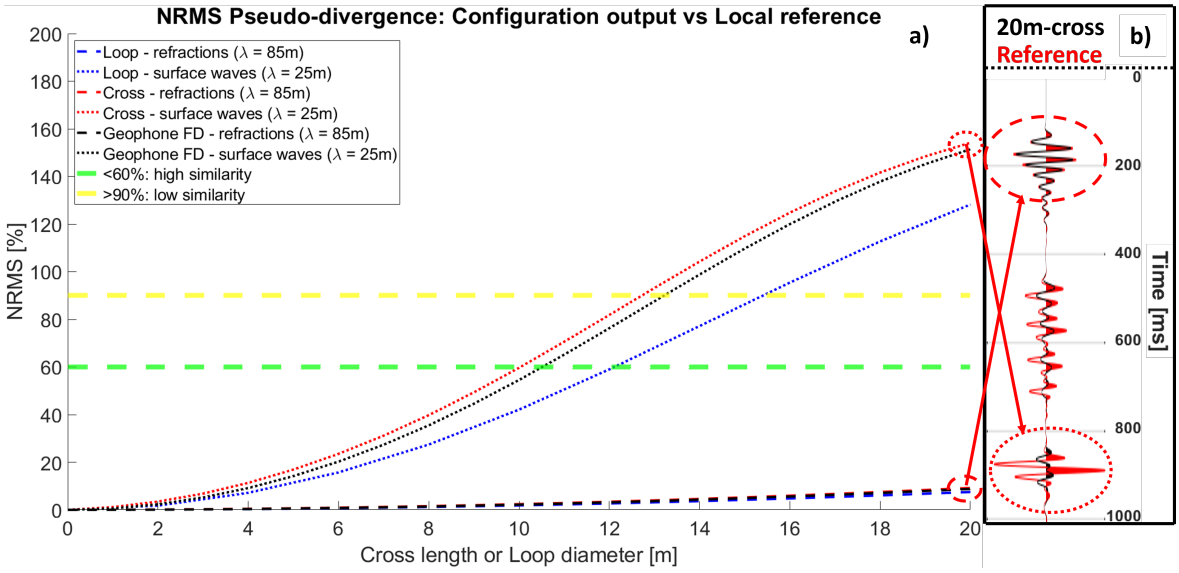

Figure 14: *a) Pseudo-divergence NRMS-plot for different configurations and wave types comparing the configuration output and local reference trace. The horizontal green and yellow line denote the defined boundaries of high and low similarity (Nap, 2020). Configuration sizes larger than 10m in diameter clearly start to show unacceptable pseudo-divergence results (considering our model parameters). b) Trace comparison of a 20m-cross pseudo-divergence output (black) with the Salvus pseudo-divergence reference in the centre (red). The pseudo-divergence refraction fit is still decent, except for a minor amplitude discrepancy. This is in contrast to the surface wave, which shows a complete misfit in terms of phase and amplitude. An AGC with a 300ms window length has been applied. Further information regarding the synthetic model parameters can be found in Section 3.2.1*

- Contrastingly, for the surface waves, the synthetic pseudo-divergence results decrease rapidly in quality for larger loop/cross dimensions. From 6-8m cross length / loop diameter ($\sim$1/4 of the wavelength) the amplitudes are considerably less resolved and for even larger configuration sizes ($>$1/3 of the wavelength), also the signal phase is distorted, as illustrated by the 20m-cross pseudo-divergence trace in Figure 14b. These results are approximately in line with previous findings regarding spatial gradient retrieval (Allouche et al., 2017; Paitz, 2021).

- We observe that the loop configuration shows slightly better similarity results. This is mostly due to less phase distortion for larger loop sizes (from a trace analysis). The origin of this difference between cross and loop is yet unclear and open for discussion.

5.5 Sensitivity Rayleigh & Love waves

Theoretically, we expect the cross & loop configuration to be exclusively sensitive to Rayleigh waves (Section 5.1). To verify this numerically, we modelled the 20m-loop response for both a pure Rayleigh and Love wave train in our 3D Salvus model (Section 3.2.1). We generated pure Rayleigh and Love waves by implementing two equally strong vector sources in the z- and y-direction, respectively. The comparison of the 20m-loop responses due to a passing Rayleigh and Love wave is presented in Figure 15. Clearly, the loop is highly sensitive to the Rayleigh wave (black) and almost insensitive to the Love wave energy (red). The red ellipse encircling the Love wave amplitudes is present at earlier times due to the slightly higher Love wave velocity.

We have attempted to obtain similar results from the Yverdon field data as well. However, we were unable to identify clear Rayleigh and Love waves in the receiver gathers. Hence, analysing the presence of specifically Rayleigh or Love waves in the DAS loop recordings was not possible from this dataset.

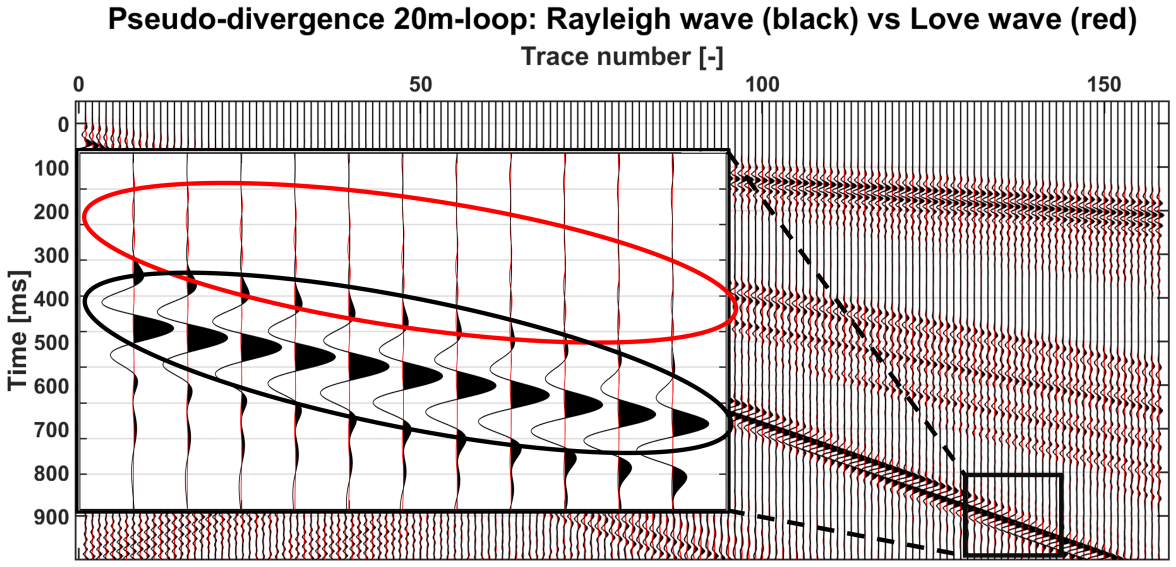

Figure 15: *Comparison of the synthetic 20m-loop response to a Rayleigh wave (black) and Love wave (red). The loop configuration is clearly sensitive to Rayleigh waves and almost insensitive to Love waves, as expected. The box displays a zoomed window of the late arrivals (surface waves). The black ellipse encircles the Rayleigh wave arrivals and the red one surrounds the hardly visible Love wave recordings (Love waves are slightly faster). The loop diameter is 6.37m. An AGC with a 300ms window length has been applied. Further information regarding the synthetic model parameters can be found in Section 3.2.1. The plotted traces have offsets ranging from 30-500m.*

5.6 Summary

We have modelled the responses of a DAS loop & cross configuration and have compared that to the local pseudo-divergence reference. We can confirm that a DAS cross and loop configuration both provide the pseudo-divergence, as expected from the theory (Section 5.1).

Additionally, we have compared the field measurements of the DAS loop and cross configurations with the pseudo-divergence obtained from a FD geophone cross, which is a proven concept and therefore acts as a reference. For the frequencies <60Hz, the DAS loop/cross - FD geophone match is very convincing in terms of phase and relative amplitudes. However, in general the DAS pseudo-divergence amplitudes are 1.2-1.8 times weaker, which is potentially related to winding/coupling issues or the configuration size. Regarding the higher frequency refractions (60-160Hz), we observe a significant mismatch, although it is unclear if this mismatch is due to poor DAS loop/cross or FD geophone results, especially considering the lower FD geophone repeatability for this frequency range (Section 4.2.1).

We have modelled many differently-sized fiber loops & crosses and analysed the effect of the configuration size with respect to the wavelength. The influence on the pseudo-divergence amplitudes is already clear for configurations spanning 1/5 of the target wavelength. Even greater loop/cross sizes result additionally in phase distortions. These effects mostly apply to surface waves considering their smaller (apparent) wavelengths compared to near-vertical P-wave events.

Finally, we have numerically confirmed that the DAS loop configuration is primarily sensitive to Rayleigh waves and almost insensitive to Love wave energy. Hence, by exploiting the presence and absence in the pseudo-divergence of respectively Rayleigh and Love waves, the DAS loop (and/or cross) configuration exhibits potential in surface wave separation.

6 Sphere: Gradient decomposition

This chapter is structured into four sections. First of all, we start by briefly discussing the relevant theory of the proposed configuration and the corresponding potential. Afterwards, we present the results obtained from a gradient decomposition of the synthetic and field measurements. These results are focused on retrieving the full divergence and estimating the V_S-V_P-ratio. Finally, we highlight the potential reasons for unsatisfactory field results of the sphere.

6.1 Theoretical potential

6.1.1 Gradient decomposition

In order to retrieve the longitudinal strain components $\partial_x v_x$, $\partial_y v_y$ and $\partial_z v_z$ from Distributed Acoustic Sensing (DAS) measurements, we propose a sphere configuration, consisting of three separate fiber loops in the orthogonal planes $x-z$, $x-y$ and $y-z$. The proposed sphere configuration is showed as field picture and conceptual sketch in Figure 16. The three loops in the $x-z$-, $x-y$- and $y-z$-plane measure the planar summed gradients and provide $(\partial_x v_x + \partial_z v_z)$, $(\partial_x v_x + \partial_y v_y)$ and $(\partial_y v_y + \partial_z v_z)$, respectively (Chapter 5).

The output of the three separate loops enables us to constrain the three spatial velocity gradients separately, by inverting the matrix relating them:

$$\partial_x v_x = 0.5 * (loop_{xz} + loop_{xy} - loop_{yz}) \tag{14a}$$

$$\partial_y v_y = 0.5 * (-loop_{xz} + loop_{xy} + loop_{yz}) \tag{14b}$$

$$\partial_z v_z = 0.5 * (loop_{xz} - loop_{xy} + loop_{yz}) \tag{14c}$$

The retrieved longitudinal velocity gradients can either be used separately, or summed to obtain the full wavefield divergence (Equation 6), depending on the application.

For practical reasons, it is probably convenient if the sphere dimensions are relatively small, as the sphere configuration must be buried. Furthermore, if the sphere configuration is used for purposes involving the free surface condition (FSC), a deeper sphere centre would be undesirable. The effect of seismic receivers being only a few tens of centimeters away from the free surface is discussed in Curtis & Robertsson (2002).

With regard to the proposed smaller dimensions, one gauge length will entail many loop windings and the three loops will become bundles of cable. This could potentially cause difficulties in terms of inadequate coupling of the inner cables.

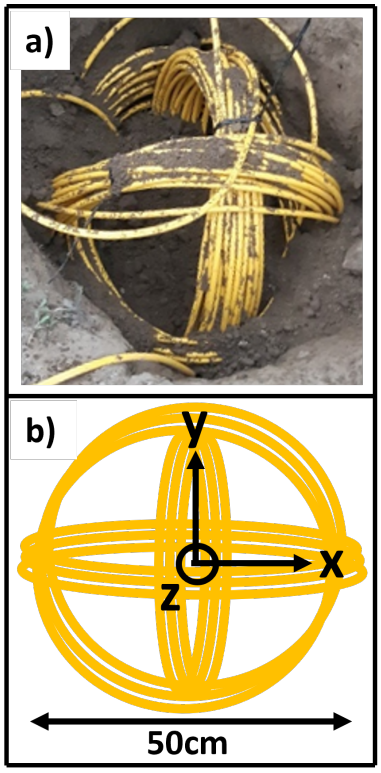

Figure 16: *a) Picture of the sphere configuration at the Yverdon test site. b) Conceptual drawing of the sphere configuration illustrating the three separate loops in the three orthogonal planes.*

6.1.2 Estimating local Vs/Vp-ratio

Equation 10a (Section 2.3.3) shows that the full- and pseudo-divergence of a wavefield at the free surface are only scaled by the local material properties. These material properties are described by the Lamé constants λ and μ (J. Robertsson & Curtis, 2002), but can also be expressed in terms of the P- and S-wave velocities (V_P and V_S respectively). Hence, the pseudo- and full divergence at the free surface provide information about the local V_S and V_P, without

the necessity of travel time information (Curtis & Robertsson, 2002). This is expressed by rewriting Equation 10a:

$$\nabla \cdot v = 2 \left(\frac{V_S}{V_P} \right)^2 (\partial_x v_x + \partial_y v_y) \tag{15}$$

From the sphere configuration, we have access to both the pseudo-and full divergence by applying the gradient decomposition to the sphere recordings (Section 6.1.1). Hence, Equation 15 enables the approximation of the local V_S-V_P-ratio from DAS sphere data only. Note that the term 'local' is not fixed to specific spatial dimensions, but instead dependent on the target wave type, orientation and wavelength/frequency/velocity, which are proportional to each other (Park et al., 2019).

6.2 Measuring full divergence

6.2.1 Synthetic data

To validate the theoretical potential of the fiber sphere, we implemented a synthetic sphere in our Salvus model with a diameter of 0.50m and composed of three separate fiber loops (Sections 3.2.1 and 3.2.2). By decomposing the gradients of the synthetic sphere recordings, the separate synthetic spatial velocity gradients $\partial_x v_x$, $\partial_y v_y$ and $\partial_z v_z$ were obtained. As an example, a comparison is shown in Appendix E.1 between the decomposed vertical gradient $\partial_z v_z$ and the Salvus $\partial_z v_z$-reference. Clearly, the fit is very accurate for both the refractions and surface wave event, which validates the gradient decomposition approach for sphere recordings.

As discussed in Section 6.1.1, the full divergence is obtained by summing the three decomposed gradients. The result of applying this to the synthetic data is presented in Figure 17. We observe an excellent match for all wave types between the full divergence obtained from the synthetic sphere recordings and the Salvus model reference. This synthetic validation is valuable, as it confirms the decomposition method/code which is also applied to the field data at a later stage.

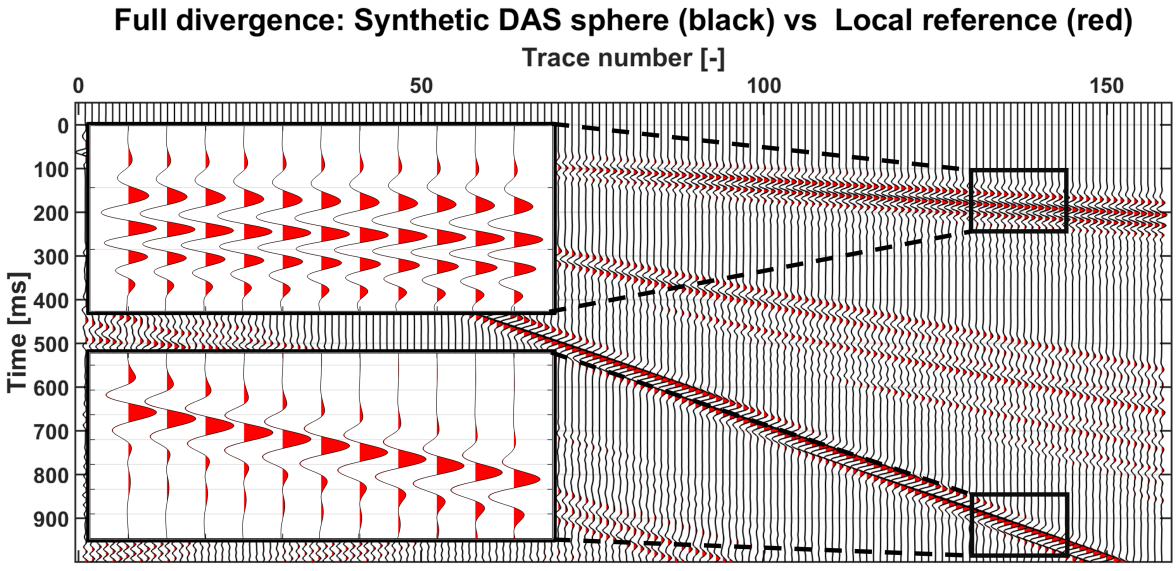

Figure 17: *Comparison of the full divergence obtained by the synthetic sphere (black) and the Salvus full divergence reference (red). The traces show perfect overlap, numerically confirming the theoretical potential of measuring the divergence by a DAS sphere. The sphere diameter is 0.50m. An AGC with a 300ms window length has been applied. The two boxes display zoomed windows of the early and late arrivals (refractions and surface waves respectively). Further information regarding the synthetic model parameters can be found in Chapter 3.2.1. The plotted traces have offsets ranging from 30-500m.*

6.2.2 Field data

The sphere is the only field configuration at Yverdon which is able to provide the vertical gradient $\partial_z v_z$, by means of the gradient decomposition. Hence, there is no reference field data which can verify the sphere-retrieved full divergence results, which are presented in Appendix E.2 with and without included higher frequencies. In these results, we notice predominantly high amplitudes for the early arrivals (refractions), which are even more prominent compared to the pseudo-divergence results, obtained by the loop and cross. This is probably related to the loop/cross configuration being only indirectly sensitive to vertical gradient information through the free surface effect (in contrast to the sphere) (J. Robertsson & Curtis, 2002).

A potential verification of the sphere results is the comparison of the inline gradient $\partial_x v_x$ obtained from the sphere decomposition and the FD geophone configuration. Note that the geophone cross and fiber sphere are not co-located. In fact, they are separated by 10m, but in exact crossline (y-)direction. Hence, regarding the offsets (plane wave assumption) and comparable soil conditions, little effect due to their crossline separation is expected. However, the sphere configuration is significantly closer to the road, possibly influencing the sphere and geophone results differently (Section 4.3).

The inline gradient comparison of the sphere decomposition and FD geophone reference is shown in Figure 18. Clearly, the match between the DAS sphere and FD geophone traces regarding $\partial_x v_x$ is far from optimal, both in terms of phase and relative amplitudes. The level of similarity is inconsistent and dependent on the selected trace- and time window. Additionally, the applied amplitude correction factor (Section 3.3.2) is 3.52, which is high compared to the loop/cross configuration and indicates a reduced sensitivity of the DAS sphere. The same reduced sphere sensitivity was discussed in Section 4.2.2, based on the configuration frequency spectra (Figure 8) . Plausible reasons for the poorer DAS sphere performance are considered in Section 6.4.

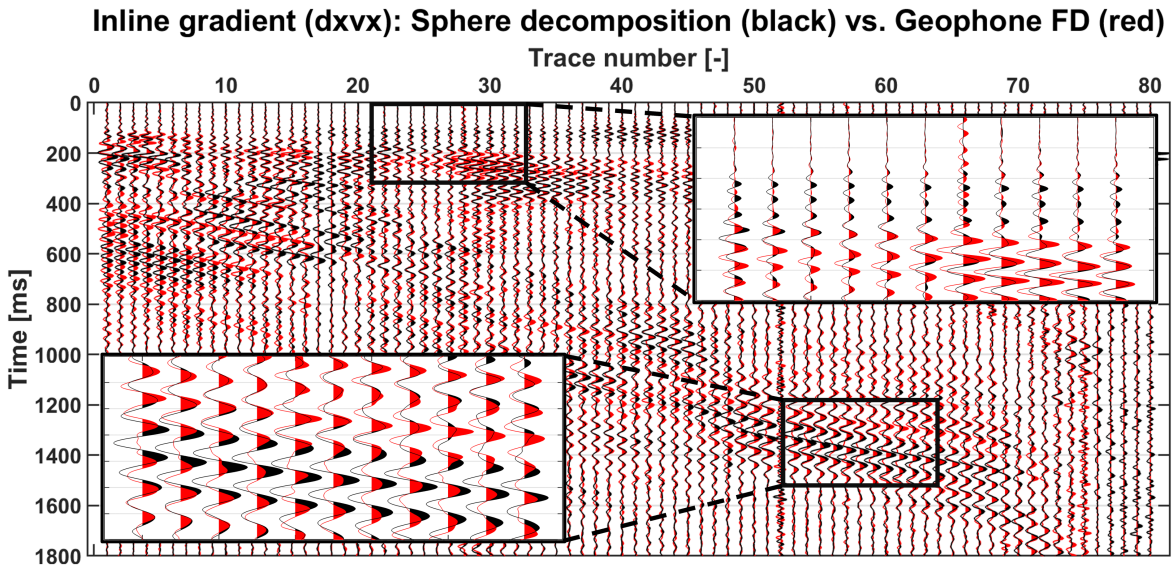

Figure 18: *Comparison of the inline velocity gradient (dxvx) retrieved from the decomposed sphere measurements (black) and geophone pair 5-11 (red). The fit is far from optimal and of much poorer quality compared to the inline DAS cross string for example. The DAS sphere has a diameter of 0.50m and the geophone spacing is 3m. The offset of the first channel is 71m increasing with approximately 2.80m every trace (moving source). The data for this comparison has been bandpass filtered by an Ormsby-filter [7-60Hz] and an AGC is applied with a 1200ms window length. The DAS amplitudes have been multiplied with a factor 3.52 to equalize the norms of both datasets.*

6.3 Estimating Vs/Vp-ratio

6.3.1 Synthetic data

The V_S-V_P-ratio can be retrieved from the ratio of the full- and pseudo-divergence at the free surface, as expressed by Equation 15. A convenient way to analyse the behaviour of this V_S/V_P-approximation, is by comparing the vertical gradient $\partial_z v_z$ and the pseudo-divergence at the free surface, which is shown in Appendix E.3 for the synthetic data. The full divergence is the resultant of both components (Equation 6), so the more the $\partial_z v_z$- and $(\partial_x v_x + \partial_y v_y)$-amplitudes cancel each other (see Appendix E.3), the smaller the full divergence is. This will result in a smaller V_S-V_P-ratio, considering that the full divergence comprises the nominator of Equation 15.

We applied Equation 15 to the synthetic data and found a V_S-V_P-ratio of approximately 0.3, which differs less than 1% with the true ratio (obtained directly from known model velocities). Curtis & Robertsson (2002) already mentioned the significant impact of not being exactly at or very close to the surface regarding the equation validity. Therefore, considering that the centre of a sphere configuration can never be exactly at the surface, we analysed the validity of Equation 15 at different depths in our Salvus model (Section 3.2).

The result of this analysis is shown in Figure 19 and shows the validity of the V_S-V_P-ratio approximation as a function of depth. Clearly, the approximation quality rapidly breaks down with depth already within the first meter. Additionally, we notice that the V_S/V_P-estimation diverges significantly faster for:

- refracted waves, which have a near-vertical incidence angle, in contrast to the horizontally propagating surface waves.
- higher frequencies / shorter wavelengths, which is theoretically expected considering that the distance to the free surface is relatively larger compared to the wavelength.

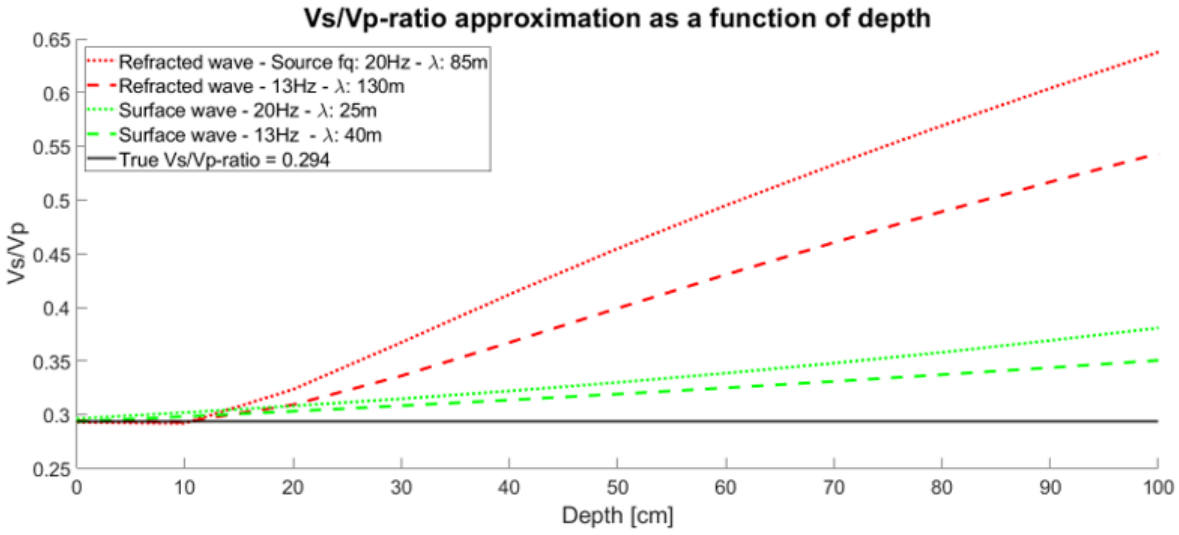

Figure 19: *Plot of the V_S-V_P-ratio approximation as a function of depth for different wave types and frequencies. Clearly, the approximation rapidly breaks down already over the first meter, especially for the refracted waves. Additionally, the validity of the V_s-V_p-ratio some depth below the free surface is frequency/wavelength dependent as well. The grey line denotes the true V_S-V_P-ratio, directly obtained from the model values. Our standard Salvus model was utilized for obtaining the synthetic data. Further information regarding the synthetic model parameters can be found in Chapter 3.2.1.*

6.3.2 Field data

Analogous to the synthetic data, we applied the same approach to the Yverdon sphere data. Unfortunately, from the decomposed gradients, no convincing V_S/V_P results could be retrieved. For selected surface wave windows, ratio values of 0.6 were obtained, which is relatively high for surface soils, but could potentially be close to the true local ratio (Salem, 2000). However, the same computation based on the refracted waves, resulted in values above unity, which is nonphysical. Furthermore, the sphere data seems overall too unstable to compute one representative V_S/V_P-value, as the computed values diverge significantly depending on the picked traces & times.

The poor sphere performance is illustrated by Figure 20, which compares the decomposed vertical gradient $\partial_z v_z$ and pseudo-divergence $(\partial_x v_x + \partial_y v_y)$, similar to the synthetic case (Section 6.3.1). From the comparison plot in Figure 20 we recognize two main features.

- The vertical gradient $\partial_z v_z$ (black) exhibits very large amplitudes compared to the pseudo-divergence (red). This feature results in the nonphysical V_S/V_P-values for the refracted waves and is contrasting substantially to the synthetic result (see Appendix E.3).
- The surface wave event is incoherent, which results in relative amplitude changes and corresponding inconsistent V_S/V_P-results depending on the selected trace & time window.

However, the V_S/V_P field data trends are similar to the synthetic results, with regard to wave type and frequency/wavelength factors (shown in Appendix E.4). We observe higher (less realistic) V_S-V_P-ratios for 1) the refracted waves and 2) a higher frequency content (shorter wavelengths). These features are clearly recognizable in the synthetic results as well (see Figure 19), considering that the DAS sphere centre was approximately 30-40cm below the free surface. Nevertheless, the inconsistent and non-physical V_S/V_P-computations probably can not be entirely contributed to the sphere centre depth. Potential other significant factors are discussed in the next section (Section 6.4).

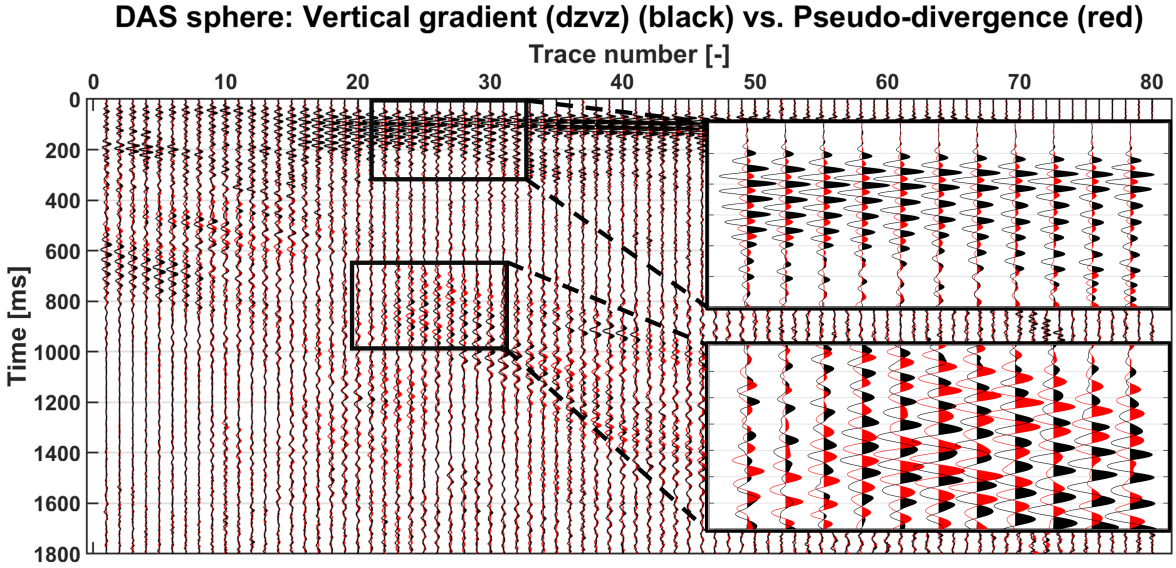

Figure 20: *Field data comparison of the vertical gradient (dzvz) (black) and pseudo-divergence (red), both retrieved from the decomposed sphere measurements. The amplitudes are cancelling each other less compared to the synthetic results (see Appendix E.3), especially for the early arrivals (refractions). Hence, unrealistic V_S-V_P-ratios are obtained. The offset of the first channel is 71m increasing with approximately 2.80m every trace (moving source). The data for this comparison has been bandpass filtered by an Ormsby-filter [7-60Hz] and an AGC is applied with a 1200ms window length.*

6.4 Unsatisfactory field results & sphere size trade-off

The field data from the Yverdon DAS sphere does not show the same potential as the synthetic results. Although the theoretical concepts were confirmed by the synthetic data, we observe that the sphere field results show divergent features and exhibit relatively poor sensitivity and repeatability performance. This was demonstrated by the frequency spectra (Figure 8), non-matching inline gradient results (Figure 18) and unrealistic V_S-V_P-ratios. We recognize two potentially related external factors:

- The road at the Yverdon test site is directly next to the sphere configuration (see Figure 4). As discussed in Section 4.3, the road probably has a major effect on the DAS and geophone recordings. However, this effect is probably larger for the sphere, considering the sphere being much closer to the road.
- It is more difficult to successfully bury a 3D DAS configuration, like the sphere, compared to a 2D configuration such as the loop or cross. Hence, this has potentially negatively influenced the coupling of some sphere parts due to less compacted soil at the inner side of the fiber sphere.

The above-mentioned factors have potentially impacted the results significantly. However, we expect the largest factor being related to the necessary cable bundling of the sphere configuration. The sphere consists of three separate loops and the loop configuration itself has proven be to successful, also in terms field results (see Chapter 5). The major difference between the 2D loop and 3D sphere is their size (circumference 10/20m vs 1.5m), which is directly related to the amount of necessary windings (see Section 3.3.2). Hence, the 3D sphere contains many cable windings which are strapped and bundled together. We expect that this results in excessively insufficient coupling of inner-bundle cables, which don't/hardly have any direct contact with the ground. This idea is supported by poorer shot-to-shot NRMS-results (see Figure 7) and lower amplitudes for most frequencies (see Figure 8). The only configuration showing worse repeatability and sensitivity results is the 0.5m mini-cross, which is the other bundled cable configuration.

In order to make the DAS sphere configuration attractive, also in practice, it must be mainly improved in terms of sensitivity and reliability. Hence, the first priority in this regard is to reduce the amount of cable windings, which can be done in two ways. One option is to increase the dimensions of the sphere. However, this is probably inconvenient primarily for practical (burial) reasons in the field. Additionally, it results in the sphere centre being further below the surface, negatively impacting the validity of the free surface condition.

A more realistic alternative is to reduce the amount of windings by using smaller gauge lengths, which are becoming available in the future. Furthermore, an interesting alternative could be the employment of a much thinner cable, potentially mitigating the coupling-issue, but probably at the cost of configuration robustness. In March 2021, we have conducted another small-scale field experiment at Honggerberg (Zurich), including a mini-sphere configuration composed of almost bare fiber. However, considering the limited preparation time, the mini-sphere data quality proved insufficient for further analysis so far. Nevertheless, other parts of this dataset will be subject of further research.

6.5 Summary

We have showed with synthetic data that the DAS sphere recordings can provide:

- The full wavefield divergence (Equation 6).
- The separate spatial velocity gradients $\partial_x v_x$, $\partial_y v_y$ and $\partial_z v_z$ by a gradient decomposition approach.

We numerically analysed the validity of the local V_S/V_P-approximation, based on the ratio of the full- and pseudo-divergence, at different depths. We found that the approximation breaks down rapidly over the first meter below the surface and is largely related to wave type and frequency/wavelength.

We compared the field results of the DAS sphere with the FD geophone configuration in terms of the inline gradient $\partial_x v_x$, for which we observe a poor fit. We have not been able yet to retrieve reliable V_S/V_P-results from the sphere field data. However, the field V_S/V_P-results show similar trends compared to the synthetics in terms of wave type and wavelength dependency. There are multiple potential factors related to the sub-optimal sphere field results, although we expect the cable bundling to be most important.

7 DAS: Local shear wave velocity approximation

We structure this chapter as follows: First we review the relevant theory and we theoretically work out the proposed configuration for local shear velocity estimations. Subsequently, we test this concept on our synthetic model and discuss the advantages. As a last step, we apply the same method on the Yverdon field data and discuss the results.

7.1 Theory

7.1.1 Background theory

At the free surface, incident upgoing P-waves are reflected as downgoing P-waves and converted SV-waves. This results in a discrepancy between the true incident angle i_P and the apparent incidence angle $\overline{i_P}$ (Edme & Singh, 2008). The measured apparent incidence angle $\overline{i_P}$ is a superposition of the incident- (P), reflected- (P) and converted wave (SV) particle velocities and hence, the apparent incidence angle $\overline{i_P}$ differs from the true P-wave incidence angle i_P (Svenningsen & Jacobsen, 2007). The relation describing true and apparent incidence angles was already formulated by Wiechert & Zoeppritz (1907):

$$\frac{\sin\left(\frac{1}{2}\overline{i_P}\right)}{V_S} = \frac{\sin\left(i_P\right)}{V_P} = p, \tag{16}$$

where V_S is the S-wave velocity, V_P the P-wave velocity and p the horizontal slowness/ray parameter. Equation 16 can be rearranged to:

$$V_S = \frac{\sin\left(\frac{1}{2}\overline{i_P}\right)}{p} \tag{17}$$

For general velocity distributions, V_S is the effective shear velocity of a half space: $V_{S,\,\text{eff.}}$ (Svenningsen & Jacobsen, 2007). Hence, $V_{S,\,\text{eff.}}$ is an average of a certain volume of the subsurface dependent on the wavelength of the incoming P-wave. The depth-sensitivity of the computed $V_{S,\,\text{eff.}}$ is extensively discussed in Park et al. (2019), including empirical relationships. For convenience, we will denote $V_{S,\,\text{eff.}}$ as V_S in the rest of the chapter.

The apparent incidence angle $\overline{i_P}$ is directly obtained from applying the following relation to the ratio of the horizontal and vertical wavefield at the surface (Edme & Singh, 2008):

$$\tan(\overline{i_P}) = \frac{U_x^P}{U_z^P}, \tag{18}$$

where U is the measured wavefield, which can be either particle displacement, velocity or acceleration. However, note the method requirement to exclusively use P-wave energy for the V_S-estimation. (Park et al., 2019).

7.1.2 Proposed configuration

The estimation of V_S from Equation 17 requires information on the horizontal slowness of the incident P-wave. Hence, especially in situations with an unknown source back-azimuth, this traditionally demands a large geophone or Distributed Acoustic Sensing (DAS)-array for the horizontal slowness determination, which can be labour- and cost-intensive.

Therefore, we propose incorporating spatial gradient information from local DAS measurements to have access to the effective shear velocity without the necessity of horizontal slowness information. This is possible by exploiting the relation between the horizontal slowness p, the horizontal particle accelerations $A_{x,y}$ and the horizontal spatial velocity gradients $\partial_x v_x$ and $\partial_y v_y$ (Sollberger et al., 2016):

$$p_{x,y} = \frac{S_{x,y}}{A_{x,y}}, \tag{19}$$

where $S_{x,y}$ is the strain rate in x- and y-direction and equal to $\partial_x v_x$ and $\partial_y v_y$ (see Chapter 2.3.1). This enables the computation of V_S from only the local horizontal spatial gradients and particle accelerations.

In order to retrieve the crucial spatial gradients, we suggest exploiting the DAS loop configuration (see Chapter 5), considering the omni-directional property of the loop shape. Hence, the back-azimuth of the wavefield is removed as a potential influencing factor. In addition, one centred 3C-geophone or seismometer is needed regarding the particle acceleration measurements.

For this DAS loop + 3C-geophone configuration, we can rewrite and combine Equations 17, 18 and 19 to obtain the following expression:

$$V_S = \frac{\sin\left(\frac{1}{2}\left(\tan^{-1}\left(\frac{\sqrt{A_x^2+A_y^2}}{A_z}\right)\right)\right)}{\left(\frac{S_{x+y(loop)}}{\sqrt{A_x^2+A_y^2}}\right)}, \tag{20}$$

where $A_{x,y,z}$ are the particle accelerations in x-, y- and z-direction and $S_{x+y(loop)}$ is the pseudo-divergence ($\partial_x v_x + \partial_y v_y$) measured by the DAS loop (see Section 5.1). The complete derivation of this expression is presented in Appendix F.1.

Equation 20 can be rewritten similarly for the cross configuration. In case of an active experiment (the source back-azimuth is known), using one inline string (x or y) is plausible as well, considering the (theoretical) absence of crossline P-wave energy. However, when the trenched cable is not winded like the Yverdon cross strings, care must be taken with regard to the gauge length (Paitz, 2021).

7.2 Synthetic data

We validated the proposed method for a synthetic 10m-fiber loop + 3C-geophone configuration by applying Equation 20 to the synthetic data by means of a Hilbert transform and sliding window in space and time. The result is demonstrated in Figure 21, which shows a simple V_z-receiver gather overlain by the computed V_S-values.

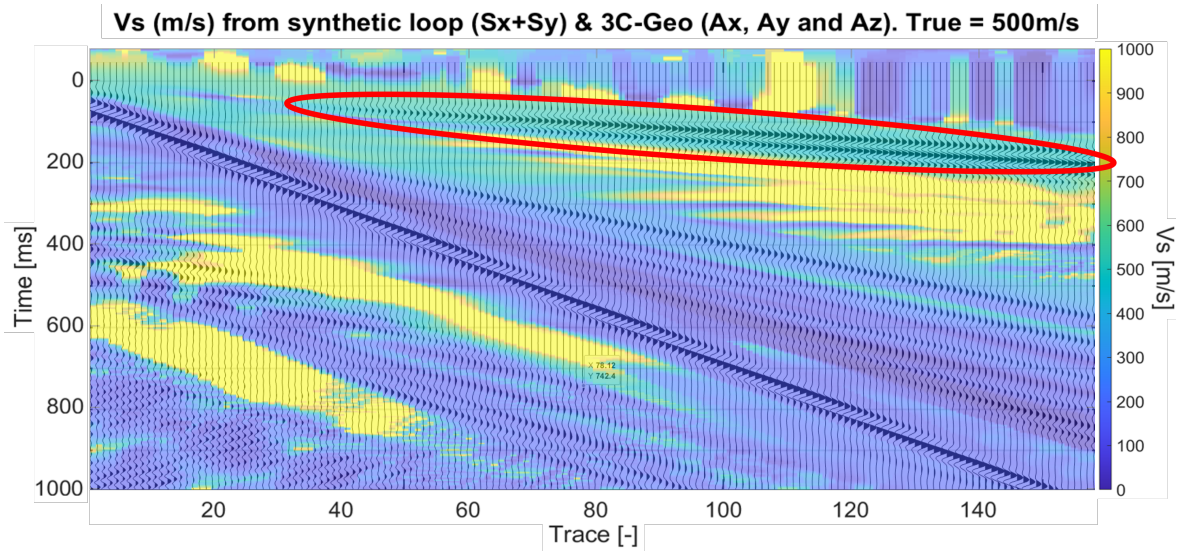

Figure 21: *Synthetic receiver gather of the V_z-component overlain by the computed V_S-values applying Equation 20 by means of a Hilbert transform and sliding window in space and time. The red ellipse encircles the refracted waves, which are the only arrivals providing correct V_S-values (true V_S = 500m/s), due to their pure P-wave content. Regarding the V_z receiver gather: AGC window length = 300ms. Further information regarding the synthetic model, see Section 3.2.*

We conclude two things from Figure 21.

- We recognize that the configuration of a fiber loop + 3C-geophone is able to estimate the local V_S correctly for pure P-wave events and that the validity of Equation 20 is therefore confirmed.
- We observe that the true model shear velocity of 500m/s is only estimated correctly for the refracted waves, as expected, which are encircled by the red ellipse. All other parts in the receiver gather either don't contain coherent seismic energy (before the refractions), or are not pure P-wave events, which is a method requirement (Park et al., 2019).

7.2.1 Azimuth independence

As discussed in Section 2.2.2, the DAS loop output is independent of the horizontal wavefield propagation direction. This omni-directional loop property results in local V_S-estimations which are free from influences related to the source back-azimuth. In order to validate the independence of V_S-approximations with regard to the wavefield back-azimuth, we have performed numerical simulations including one synthetic 10m-loop + 3C-geophone configuration and a varying source direction (with constant source-receiver offset).

The results are presented in Figure 22, which demonstrates the directional independence of the synthetic 10m-loop + 3C-geophone configuration in terms of V_S-computations. The estimated V_S-values accurately match for the time window exclusively containing pure P-wave refractions (denoted by black reference lines). Hence, this synthetic result confirms that such DAS loop + 3C geophone configuration can be installed without having any pre-knowledge on the wavefield back-azimuth.

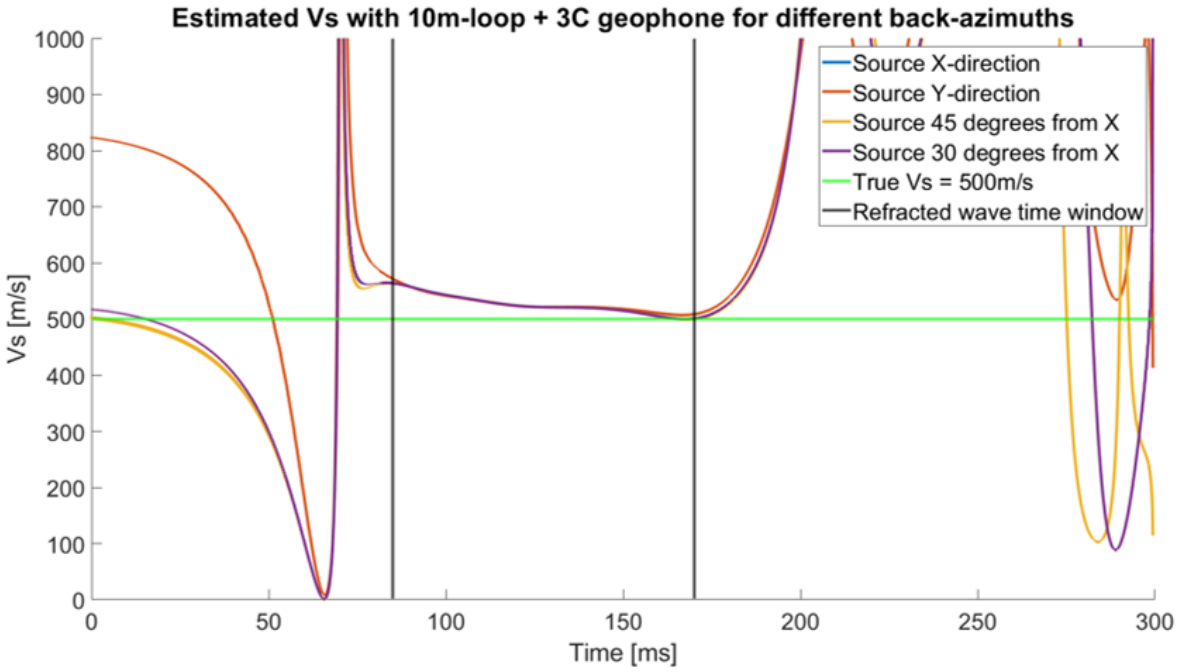

Figure 22: *Comparison of the computed V_S-results for sources with different back-azimuths but equal offsets (360m). The results clearly show the omni-directional property of the loop configuration and hence, the complete independence of source back-azimuth for our proposed configuration. The green line denotes the true V_S-reference at the surface and the black lines show the time window exclusively containing refracted waves (pure P-wave energy). Further information regarding the synthetic model parameters, see Section 3.2.*

Apart from the loop omni-directionality, we note that the computed V_S-values are slightly above the true model shear velocity at the surface (500m/s). Presumably, this is related to the model velocity gradient (see Section 3.2), considering that the computed V_S-value is an effective average over a certain volume of the subsurface, dependent on the wavelength of the incoming P-wave Park et al. (2019) (see Section 7.1.1). Additionally, Figure 22 clearly emphasizes again the importance of selecting P-wave energy as the computations outside the refracted wave time window are highly unstable.

7.3 Field data

Following the successful synthetic results, we applied the same approach to the Yverdon data and used the DAS 10m-loop and middle geophone as the proposed loop + 3C-geophone configuration. The result is demonstrated in Figure 23 and shows plausible V_S-values for the refracted arrivals. However, the computed V_S-values within the red encircled refracted wave window are not stable enough to provide one representative V_S-value yet. The observed V_S-variation within the refraction window does not depend on offset considering that the averaging volume for the effective V_S-approximation does not change for a fixed configuration, also demonstrated by the synthetic results (see Figure 21).

Surprisingly, in case of the Yverdon field data, using exclusively recordings from the inline cross string gives more stable V_S-results, which is shown in Appendix F.2. This is remarkable as the repeatability of the loop and cross is similar (see Section 4.2.1), just as the pseudo-divergence results (see Chapter 5). Therefore, we expect this phenomenon is not related to the loop or cross properties, but to the specifics of the Yverdon test site. As shown in Section 4.3, the contrasting road generates scattering of the refracted waves in crossline (y-)direction. Hence, the presence of the road results in the single event assumption to be violated, which only affects the y-sensitive loop, in contrast to the single inline cross string.

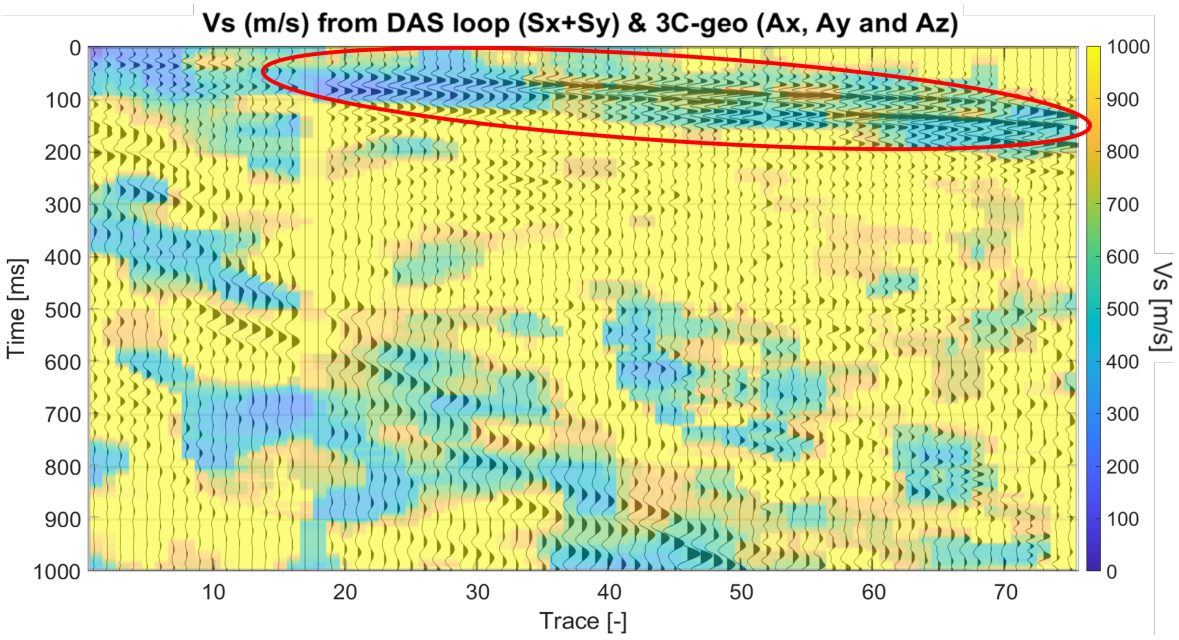

Figure 23: *Field data receiver gather of the V_z-component overlain by the computed V_S-values from the DAS loop + 3C-geophone configuration. The red ellipse encircles the refracted wave arrivals which provide plausible V_S-estimations. However, also the refracted P-wave energy does not provide one representative V_S-approximation as the computed V_S-value differs per trace/offset. Regarding the V_z receiver gather: The data has been bandpass filtered by an Ormsby-filter [7-60Hz] and an AGC is applied with a 1200ms window length.*

This explanation is numerically supported, as shown in Appendix F.3, by including the synthetic road feature in our Salvus model. Here, we observe that the nearby road distorts the V_S-computation from a the fiber loop + 3C-geophone configuration, in contrast to the estimations retrieved from exclusively inline information.

7.4 Summary

We proposed a configuration consisting of a fiber loop and one centred 3C-geophone, which is able to provide the local shear wave velocity without requiring horizontal slowness information of the incident P-wavefield. This is possible by exploiting spatial gradient information, obtained by the DAS loop.

We derived an expression taking the loop and centred 3C-geophone recordings as input, which we validated numerically. The synthetic results show stable and correct V_S-computations for only the refracted arrivals, demonstrating the P-wave energy condition for this method. Additionally, we numerically showed the advantage of using the omni-directional loop resulting in V_S-computations being completely independent of the wavefield back-azimuth.

We applied the same method to the Yverdon field data, which shows plausible but slightly unstable V_S-results. However, this instability is probably related to the nearby road violating the single event event assumption due to refraction scattering.

8 Discussion

8.1 Constraints & recommendations

Here, we discuss a few aspects which are noteworthy constraints on the presented results and/or general recommendations for a potential follow-up project.

Regarding the synthetic results, we were limited to a certain extent in terms of element sizes, source frequencies and model velocities. This is due to the several numerical criteria which must be met in combination with a standard personal laptop (running times 1-4 hours). For incorporating higher frequencies or lower model velocities, more professional computational resources are required.

For the Yverdon Distributed Acoustic Sensing (DAS) measurements, we have used a Silixa iDAS v2.4 interrogator, which is one of the commercially available DAS interrogators on the market. Although most systems have approximately similar specifics, there is a possibility that slightly different results are retrieved with other DAS systems, especially if they operate with a different gauge length.

The reference measurements in the field were retrieved from a 3C-geophone cross configuration. Although computing gradients from a geophone cross is a well-known and proven concept (J. Robertsson & Curtis, 2002), it is highly sensitive to sensor misplacement-related FD errors (extensively described by Allouche et al. (2017)). In terms of NRMS repeatability, the geophone results even show poorer results compared to the DAS loop and cross (see Section 4.2.1). Hence, differences between the DAS and geophone results are not necessarily DAS inaccuracies/shortcomings.

Our results show a likely influence of the nearby road on the recorded data. This has made the interpretation more difficult and potentially obscures relevant data features. Additionally, due to the configuration lay-out at the Yverdon test site (see Figure 4), the sphere results are probably more affected. Therefore, we strongly recommend avoiding adjacent contrasting bodies for a potential next field campaign.

Furthermore, the weather conditions changed significantly during the acquisition from dry conditions in the morning to very wet conditions at the end. Hence, the shallow soil properties must have evolved throughout the acquisition, which potentially has had an impact on primarily the surface wave-related results.

Finally, a valuable addition to a follow-up field experiment is a reference measurement for the vertical velocity gradient ($\partial_z v_z$). The DAS sphere showed great potential from the synthetic results, however, the field results were less convincing. Without a vertical gradient reference it is difficult to distinguish between poor performance of the sphere configuration and potential unexpected ground conditions. This $\partial_z v_z$-reference could be accomplished by burying two (V_z-)geophones at depths corresponding to the top and bottom of the buried sphere. In this way, the centres of the sphere and geophone FD-approximated vertical gradient will coincide.

8.2 Applications

8.2.1 Pseudo-divergence

We have shown that the DAS loop and cross configuration are able to provide the wavefield pseudo-divergence (see Chapter 5). The pseudo-divergence ($\partial_x v_x + \partial_y v_y$) is proportional to the full divergence by only a scalar (at the free surface), which is sometimes estimated from previous studies (Maeda et al., 2016). As discussed in Section 5.5, predominantly Rayleigh waves are present in divergence component. Hence, this opens up possibilities for DAS in terms of potential ground-roll suppression or isolation of P-wave and S-P converted events.

Edme et al. (2018) show that by having access to the omni-directional divergence (DAS loop) the ground roll energy can be successfully subtracted in an adaptive way. This would primarily allow a relaxation of the spatial sampling by removing the ground-roll locally instead of requiring spatially dense arrays. Additionally, adaptive P-wave subtraction by DAS could potentially contribute to improved S-wave analysis with corresponding applications, summarized by Schmelzbach et al. (2018).

8.2.2 Vertical gradient

Despite the dubious field results of the DAS sphere so far, it does have potential, taking the synthetic results and promising development of the gauge length into consideration (Chapter 6). In terms of applications regarding the divergence, there exists much similarity with the loop/cross. However, a sphere configuration is able to provide the full divergence directly, without scalar assumptions at the free surface.

A key difference in terms of applications is the ability of the DAS sphere to additionally provide the separate vertical gradient ($\partial_z v_z$). Access to $\partial_z v_z$ could greatly contribute to downward continuation and other related seismic processing steps (Claerbout & Doherty, 1972) (Yilmaz, 2001), such as shallow static corrections. Incorporating vertical gradient information can assist in the extrapolation of measured surface data to deeper levels in the subsurface. A comprehensive overview of the downward continuation approach for potential field data is given by Tran & Nguyen (2019).

8.2.3 Access to local material properties & relation to depth profile

We demonstrated at least numerically that the DAS sphere and a DAS loop + 3C-geophone configuration can provide local information on the V_S-V_P-ratio and V_S respectively (see Chapters 6 and 7). Besides that, the field results of the DAS loop + 3C-geophone configuration were already promising (see Section 7.3). These computed local wave velocities are directly related to material properties such as the Lamé parameters and the Poisson ratio (Bachrach et al., 2000) (Yilmaz, 2001). Hence, retrieving V_S/V_P and V_S gives access to information on the local subsurface structure.

In terms of applications, exploiting this concept is possible on multiple scales depending on the targeted frequencies. As discussed in Park et al. (2019), the depth-sensitivity of the locally retrieved V_S is equally proportional to the wavelength and frequency as they are related by $\lambda = \frac{v}{f}$. Hence, by computing V_S for different frequencies/periods, the relative information content with regard to depth is different as well (Park et al., 2019). This notion can be exploited through an inversion algorithm, and applied to teleseismic waves for instance, to obtain a local depth model of either V_S or related material properties for the upper crust kilometers (Svenningsen & Jacobsen, 2007).

The same wavelength/frequency dependent sensitivity can potentially be applied to the DAS sphere V_S/V_P-computation as well. As V_S/V_P is directly proportional to the meaningful Poisson-ratio (Hilterman, 2001), this could be an interesting application of the DAS sphere. However, more research on the feasibility is necessary.

8.3 Wavefield gradiometry: (Dis-)Advantages DAS vs. conventional geophones

The reason DAS is getting such increased attention, is due to three major advantages over conventional geophone systems:

- Unprecedented spatial and temporal sampling possibilities.
- Practical benefits of handling a cable and its non-intrusive character once the fiber is installed.
- The growing cost-effectiveness of DAS.

Hence, if similar results are achievable with DAS instead of conventional geophone systems, it is possibly profitable to switch to DAS acquisition. We've seen that this is the case for measuring the pseudo-divergence, where DAS shows at least a similar performance compared to a FD geophone cross.

In addition to the above-mentioned DAS benefits, we see an important advantage specifically regarding gradient sensing with DAS configurations. Conventional geophone gradient measurements are prone to various forms of finite-difference errors, for instance resulting from tilted or inaccurately spaced geophones (Allouche et al., 2017). This type of FD-errors is inherently solved by gradient DAS measurements as the fiber is equally sensitive along the entire configuration and the gradients are not computed from only two separate (particle velocity) values at both ends.

On the other hand, we also recognize disadvantages of using DAS for wavefield gradiometry purposes, although some of them will probably be solved in the near future. A fundamental challenge of DAS that will remain is related to measuring the vertical components of a wavefield at the free surface. This is due to DAS being limited to measuring 1D fiber strain, in contrast to 3C-geophones which can record the three orthogonal particle velocities simultaneously. Hence, convenient DAS configurations in the horizontal plane, such as the fiber loop and cross, are poorly sensitive to most incident near vertical (broadside) P-wave events (See Section 2.2.1), which usually contain (desired) reflection/refraction/teleseismic information. Although the free surface condition can be exploited or 3D fiber configurations can be employed, it will be often practical to place one or more additional geophones providing the vertical particle velocity at the free surface.

Related to the same 1D limitation of DAS are cases where the particle velocity and the desired spatial gradient are not aligned. For example, retrieving $\partial_x v_y$ and $\partial_y v_x$ (constituents of the vertical component of the rotation at the surface) with DAS has been (numerically) shown by Paitz (2021), by means of a conversion from strain rate to particle velocity and a finite-difference approach. However, this conversion approach demands configuration dimensions of a least a few wavelengths, which is relatively unpractical compared to a small scale 3C-geophone configuration. Lastly, we note that for smaller 3D configurations, like the sphere, the 10m gauge length results in the necessity of many cable windings. As demonstrated, this leads to reduced coupling of the configuration as a whole and hence, sub-optimal results. Increasing the size of the sphere is probably unpractical, so especially smaller gauge lengths are crucial in this regard. These smaller gauge lengths will become available in the future, which would certainly benefit small-sized DAS configurations (probably at the cost of a poorer SNR unfortunately). Additionally, the winding issue could potentially be mitigated by employing thinner cable/fiber. However, care should be taken regarding the expected trade-off with robustness and durability.

9 Conclusion & outlook

9.1 Conclusion

The popularity of Distributed Acoustic Sensing (DAS) is growing rapidly, mainly due to the unprecedented spatial sampling possibilities. In this study, we have investigated the potential of unconventional fiber configurations, such as a fiber loop, cross and sphere, with regard to measuring attractive gradient-based wavefield components. Here, we present our main findings:

- The repeatability and sensitivity results show significant difficulties for the sphere and mini-cross configuration, probably due to their excessive cable winding and related inadequate coupling. For sub-meter configurations, many cable windings are unfortunately unavoidable considering the gauge length and the need for uncontaminated channels. To potentially mitigate the small configuration coupling issue, the employment of thinner cable could be examined.
- The DAS loop and cross configuration convincingly provide the pseudo-divergence, defined as $\partial_x v_x + \partial_y v_y$, which is proportional to the full divergence at the free surface. Therefore, the fiber loop and cross are primarily sensitive to Rayleigh surface waves and unresponsive to Love wave energy.
- Numerical results show a large influence of the configuration size with respect to the (apparent) wavelength (λ). Configuration dimensions must not exceed $1/5\lambda$ with regard to amplitude losses and $1/3\lambda$ concerning phase distortions.
- The three independent loop recordings comprising the DAS sphere can be summed or decomposed to obtain the full divergence or the separated orthogonal gradients, respectively. At the free surface, the ratio of the measured full- and pseudo-divergence can additionally provide the local V_S/V_P-ratio, which is supported by solid synthetic results. However, the DAS sphere field results are less convincing so far, probably as a result of the excessive amount of cable windings and the associated suspected poor coupling with the ground.
- A novel 4C-configuration consisting of a fiber loop and one centred 3C-geophone is able to constrain the local effective shear wave velocity, by exploiting spatial gradient information obtained from the loop. The approach is validated numerically and the field data results are promising, despite slightly unstable V_S-estimations due to the adjacent road. The synthetic V_S-results are independent of the wavefield back-azimuth as a result of the omni-directional sensitivity of the fiber loop.

This study further supports the development of DAS opening up new DAS-possibilities with respect to ground-roll suppression, relaxation of spatial sampling criteria, downward continuation and effective shear wave velocity estimations. This DAS-potential could be applied to many seismic/seismological applications, such as wavefield separation, passive traffic/earthquake/mass movement monitoring and near-surface characterization from active shots, earthquakes and/or potentially ambient noise.

9.2 Outlook

Based on our results and additional ideas, we list some recommended topics for future research with regard to further exploitation of the DAS-potential.

- Cables at different depths. A configuration with two parallel cables deployed at different depths can potentially have interesting properties/applications. It would give access to some form of vertical gradient information, which can be expressed by horizontal gradients at the free surface and hence, can be potentially exploited with regard to rotational components.
- Poisson ratio of helicoidal configuration. In March 2021, we have conducted an additional small scale field experiment regarding helicoidal configurations. When axially compressed, a

helicoidally wrapped fiber is sensitive to both the axial compression and the perpendicular extension due to the Poisson ratio of the hosting rod/cylinder. Hence, there is always a wrapping angle for which the fiber experiences zero strain from axial compression/extension, which could have interesting applications. The field data has not been extensively analysed yet, which can hopefully be done in the near future.

- Employing (very) thin fiber. The necessary cable winding and related coupling issues for smaller configurations have been extensively described in this thesis. An interesting alternative could be the employment of (very) thin cable, which can potentially mitigate the coupling issue, however, probably at the expense of configuration robustness. Hence, a key factor is the amount of robustness and durability loss due to thin cable employment. Therefore, further research on this aspect and other consequences of using thin cable is recommended regarding the potential benefits for small-scale DAS configurations.

- Applying novel V_S-approach to real earthquake data. Regarding the local V_S-estimations from the fiber loop + 3C-geophone configuration, we have presented solid synthetic and promising field data results. However, both results were obtained from an active (synthetic) experiment. Considering Svenningsen & Jacobsen (2007), this approach should also be applicable to real earthquake data from teleseismic events or potentially ambient noise. Therefore, we recommend a passive experiment employing a similar 4C-configuration, but focused on recording teleseismic events and ambient noise.

The findings presented in this study can hopefully be used and profited from in the (near) future, to increase our knowledge about DAS and exploit the potential DAS exhibits.

10 Acknowledgements

First of all, I would like to thank you, Pascal, for all your help, ideas, feedback, flexibility and the time you put in our 'small chats', which in the end were never small. I really appreciate all the effort you invested in supervising me, being always available for questions and continuously reminding me that everything can always be sharper and more concise. I will definitely remember that every time I see you walking on H-floor during the coming years!
Patrick, thank you for taking the time to place so many helpful comments in the thesis draft version, always responding to my emails within literally a few minutes and helping me out with the fiber splicing at Honggerberg.
Cédric, I want to thank you for your sharp and valuable feedback on the thesis abstract. I appreciate that you took the time to provide such extensive comments and suggestions, despite your busy days towards the end.
I want to thank Martin van Driel for all the help related to using Salvus. Your help probably saved me days. Great thanks to the Salvus-team for providing the numerical wave propagation software, containing such an extensive set of features but being very user-friendly at the same time. Clearly, the available Salvus-features have added a lot to this project/thesis.
At last, I want to thank you Ana. At the end of the day, you were often able to put everything into perspective again. Hopefully, you can keep doing that over the next few years!

10.1 Yverdon dataset

We would like to thank the following institutes and people for facilitating or contributing to the field dataset from Yverdon:
A. Fichtner (ETHZ), F. Martin (SIG), V. Metraux (GEO2X), D. Dupuy (GEO2X), L. Guglielmetti (UniGe), A. Moscariello (UniGe), V. Perron (ETHZ) and D. Bowden (ETHZ) for enabling or contributing to the experiment. The field test was part of GECOS (Geothermal Exploration Chance Of Success).

References

Afanasiev, M., Boehm, C., van Driel, M., Krischer, L., Rietmann, M., May, D., ... Fichtner, A. (2019, 03). Modular and flexible spectral-element waveform modelling in two and three dimensions. *Geophysical Journal International*, *216*, 1675-1692. doi: 10.1093/gji/ggy469

Ajo-Franklin, J., Dou, S., Lindsey, N., Monga, I., Tracy, C., Robertson, M., ... Li, X. (2019, 02). Distributed acoustic sensing using dark fiber for near-surface characterization and broadband seismic event detection. *Scientific Reports*, *9*. doi: 10.1038/s41598-018-36675-8

Aki, K., & Richards, P. G. (2002). *Quantitative seismology* (2nd ed.). University Science Books. Hardcover. Retrieved from `http://www.worldcat.org/isbn/0935702962`

Allouche, N., Muyzert, E., & Edme, P. (2017). On the accuracy of seismic wavefield spatial gradients. *EAGE*, *2017*(1), 1-6. Retrieved from `https://www.earthdoc.org/content/papers/10.3997/2214-4609.201702076` doi: https://doi.org/10.3997/2214-4609.201702076

Bachrach, R., Dvorkin, J., & Nur, A. (2000, 03). Seismic velocities and poisson's ratio of shallow unconsolidated sands. *Geophysics*, *65*, 559-564. doi: 10.1190/1.1444751

Cedilnik, Lees, & Geisler. (2019). Ultra-long reach fiber distributed acoustic sensing for power cable monitoring..

Claerbout, J. F., & Doherty, S. M. (1972). Downward continuation of moveout-corrected seismograms. *GEOPHYSICS*, *37*(5), 741-768. Retrieved from `https://doi.org/10.1190/1.1440298` doi: 10.1190/1.1440298

Curtis, A., & Robertsson, J. O. A. (2002). Volumetric wavefield recording and wave equation inversion for near-surface material properties. *GEOPHYSICS*, *67*(5), 1602-1611. Retrieved from `https://doi.org/10.1190/1.1512751` doi: 10.1190/1.1512751

Daley, T., Freifeld, B., Ajo-Franklin, J., Dou, S., Pevzner, R., Shulakova, V., ... Lüth, S. (2013, 06). Field testing of fiber-optic distributed acoustic sensing (das) for subsurface seismic monitoring. *The Leading Edge*, *32*, 699-706. doi: 10.1190/tle32060699.1

Dean, T., Cuny, T., & Hartog, A. H. (2017). The effect of gauge length on axially incident p-waves measured using fibre optic distributed vibration sensing [Journal Article]. *Geophysical Prospecting*, *65*(1), 184-193. Retrieved from `https://www.earthdoc.org/content/journals/10.1111/1365-2478.12419` doi: https://doi.org/10.1111/1365-2478.12419

Den Boer, J. J., Mateeva, A. A., Pearce, J. G., Mestayer, J. J., Birch, W., Lopez, J. L., ... Kuvshinov, B. N. (2013). *Detecting broadside acoustic signals with a fiber optical distributed acoustic sensing (das) assembly.* WIPO. Retrieved from `https://patentscope.wipo.int/search/en/detail.jsf?docId=WO2013090544&tab=PCTBIBLIO` (WO2013090544)

Den Boer, J. J., Vianney, J. M., Koelman, A., Pearce, J. G., Franzen, A., Lumens, P. G. E., & Joinson, D. (2015). *Fiber optic cable with increased directional sensitivity.* Google Patents. Retrieved from `https://patents.google.com/patent/US9091589` (US 9,091,589 B2)

Dou, S., Lindsey, N., Wagner, A., Daley, T., Freifeld, B., Robertson, M., ... Ajo-Franklin, J. (2017, 12). Distributed acoustic sensing for seismic monitoring of the near surface: A traffic-noise interferometry case study. *Scientific Reports*, *7*. doi: 10.1038/s41598-017-11986-4

Eaid, M., Li, J., & Innanen, K. A. (2018). Modeling the response of shaped das fibres to microseismic moment tensor sources. In *Seg technical program expanded abstracts 2018* (p. 4698-4702). Retrieved from `https://library.seg.org/doi/abs/10.1190/segam2018-2998378.1` doi: 10.1190/segam2018-2998378.1

Edme, P., Muyzert, E., Goujon, N., El Allouche, N., & Kragh, E. (2018). Seismic wavefield divergence at the free surface [Journal Article]. *First Break*, *36*(12), 75-82. Retrieved from https://www.earthdoc.org/content/journals/10.3997/1365-2397.2018008 doi: https://doi.org/10.3997/1365-2397.2018008

Edme, P., Paitz, P., Sollberger, D., Kiers, T., Perron, V., Schmelzbach, C., ... Robertsson, J. O. A. (2021, April). On the use of Distributed Acoustic Sensing for seismic divergence and curl estimations. In *Egu general assembly conference abstracts* (p. EGU21-12443).

Edme, P., & Singh, S. (2008, 05). Receiver function method in reflection seismology. *Geophysical Prospecting*, *56*, 327-340. doi: 10.1111/j.1365-2478.2007.00685.x

Edme, P., & Yuan, S. (2016). Local dispersion curve estimation from seismic ambient noise using spatial gradients. *Interpretation*, *4*(3), SJ17-SJ27. Retrieved from https://doi.org/10.1190/INT-2016-0003.1 doi: 10.1190/INT-2016-0003.1

Egorov, A., Correa, J., Bóna, A., Pevzner, R., Tertyshnikov, K., Glubokovskikh, S., ... Gurevich, B. (2018). Elastic full-waveform inversion of vertical seismic profile data acquired with distributed acoustic sensors. *GEOPHYSICS*, *83*(3), R273-R281. Retrieved from https://doi.org/10.1190/geo2017-0718. doi: 10.1190/geo2017-0718.1

Farhadiroushan, M., Parker, T. R., & Shatalin, S. (2010). *Method and apparatus for optical sensing.* Google Patents. Retrieved from https://patents.google.com/patent/WO2010136810A2/en (WO 2010/136810 A2)

Fenta, M., & Szanyi, J. (2021, 05). Fibre optic methods of prospecting: A comprehensive and modern branch of geophysics. *Surveys in Geophysics*. doi: 10.1007/s10712-021-09634-8

Fichtner, A., Saygin, E., Taymaz, T., Cupillard, P., Capdeville, Y., & Trampert, J. (2013, 07). The deep structure of the north anatolian fault zone. *Earth and Planetary Science Letters*, *373*, 109–117. doi: 10.1016/j.epsl.2013.04.027

Gabai, H., & Eyal, A. (2016, Dec). On the sensitivity of distributed acoustic sensing. *Opt. Lett.*, *41*(24), 5648–5651. doi: 10.1364/OL.41.005648

Hartog, A. (2017). *An introduction to distributed optical fibre sensors.* doi: 10.1201/9781315119014

Hartog, A., Frignet, B., Mackie, D., & Clark, M. (2014, 05). Vertical seismic optical profiling on wireline logging cable. *Geophysical Prospecting*, *62*. doi: 10.1111/1365-2478.12141

Hilterman, F. J. (2001). *Seismic amplitude interpretation.* Society of Exploration Geophysicists and European Association of ....

Igel, H. (2016). The spectral-element method. In *Computational seismology* (chap. 7). Retrieved from https://oxford.universitypressscholarship.com/10.1093/acprof:oso/9780198717409.001.0001/acprof-9780198717409-chapter-7 doi: 10.1093/acprof:oso/9780198717409.003.0007

Innanen, K. (2017a). Determination of seismic-tensor strain from helical wound cable-distributed acoustic sensing cable with arbitrary and nested-helix winds. In *Seg technical program expanded abstracts 2017* (p. 926-930). Retrieved from https://library.seg.org/doi/abs/10.1190/segam2017-17664060.1 doi: 10.1190/segam2017-17664060.1

Innanen, K. (2017b). Parameterization of a helical das fibre wound about an arbitrarily curved cable axis. *European Association of Geoscientists & Engineers*, *2017*(1), 1-5. Retrieved from https://www.earthdoc.org/content/papers/10.3997/2214-4609.201701202 doi: https://doi.org/10.3997/2214-4609.201701202

Innanen, K. A., Lawton, D., Hall, K., Bertram, K. L., Bertram, M. B., & Bland, H. C. (2019). Design and deployment of a prototype multicomponent distributed acoustic sensing loop array. In *Seg technical program expanded abstracts 2019* (p. 953-957). Retrieved from https://library.seg.org/doi/abs/10.1190/segam2019-3216304.1 doi: 10.1190/segam2019-3216304.1

Kamal, S. Z. (2014). Fiber optic sensing: Evolution to value. *SPE-167907-MS*. doi: https://doi.org/10.2118/167907-MS

Kechavarzi, C., Pelecanos, L., De Battista, N., & Soga, K. (2019, 05). Distributed fibre optic sensing for monitoring reinforced concrete piles. *Geotechnical Engineering*, *50*, 43-51.

Kragh, E., & Christie, P. (2002). Seismic repeatability, normalized rms, and predictability. *The Leading Edge*, *21*(7), 640-647. Retrieved from https://doi.org/10.1190/1.1497316 doi: 10.1190/1.1497316

Kuvshinov, B. (2016). Interaction of helically wound fibre-optic cables with plane seismic waves. *Geophysical Prospecting*, *64*(3), 671-688. Retrieved from https://onlinelibrary.wiley.com/doi/abs/10.1111/1365-2478.12303 doi: https://doi.org/10.1111/1365-2478.12303

Langston, C. A. (2007, 02). Spatial Gradient Analysis for Linear Seismic Arrays. *Bulletin of the Seismological Society of America*, *97*(1B), 265-280. Retrieved from https://doi.org/10.1785/0120060100 doi: 10.1785/0120060100

Lin, Y., & Pisano, A. P. (1988, 12). The Differential Geometry of the General Helix as Applied to Mechanical Springs. *Journal of Applied Mechanics*, *55*(4), 831-836. Retrieved from https://doi.org/10.1115/1.3173729 doi: 10.1115/1.3173729

Lindsey, N. J., Rademacher, H., & Ajo-Franklin, J. B. (2020). On the broadband instrument response of fiber-optic das arrays. *Journal of Geophysical Research: Solid Earth*, *125*(2), e2019JB018145. Retrieved from https://agupubs.onlinelibrary.wiley.com/doi/abs/10.1029/2019JB018145 (e2019JB018145 10.1029/2019JB018145) doi: https://doi.org/10.1029/2019JB018145

Luo, B., Trainor-Guitton, W., Bozdağ, E., LaFlame, L., Cole, S., & Karrenbach, M. (2020, 06). Horizontally orthogonal distributed acoustic sensing array for earthquake- and ambient-noise-based multichannel analysis of surface waves. *Geophysical Journal International*, *222*(3), 2147-2161. Retrieved from https://doi.org/10.1093/gji/ggaa293 doi: 10.1093/gji/ggaa293

Maeda, T., Nishida, K., Takagi, R., & Obara, K. (2016, 10). Reconstruction of a 2d seismic wavefield by seismic gradiometry. *Progress in Earth and Planetary Science*, *3*, 31. doi: 10.1186/s40645-016-0107-4

Marijnissen, K.-A. (2020). *Spectral element elastic wave modelling of Distributed Acoustic Sensing data for the analysis of limited broadside sensitivity, in a surface seismics configuration* (Unpublished master's thesis). Utrecht University, Utrecht, The Netherlands.

Mateeva, A., Lopez, J., Potters, H., Mestayer, J., Cox, B., Kiyashchenko, D., ... Detomo, R. (2014). Distributed acoustic sensing for reservoir monitoring with vertical seismic profiling. *Geophysical Prospecting*, *62*(4), 679-692. Retrieved from https://onlinelibrary.wiley.com/doi/abs/10.1111/1365-2478.12116 doi: https://doi.org/10.1111/1365-2478.12116

Muyzert, E., Allouche, N., Edme, P., & Goujon, N. (2019). A five component land seismic sensor for measuring lateral gradients of the wavefield. *Geophysical Prospecting*, *67*(1), 97-113. Retrieved from https://onlinelibrary.wiley.com/doi/abs/10.1111/1365-2478.12716 doi: https://doi.org/10.1111/1365-2478.12716

Nap, A. (2020). *On the fidelity of Distributed Acoustic Sensing at the surface* (Unpublished master's thesis). Eidgenössische Technische Hochschule Zürich, Zürich, Switzerland.

Nap, A., Edme, P., Schmelzbach, C., Paitz, P., & Robertsson, J. (2020). Surface seismic with distributed acoustic sensing: Is trenching worthwhile? *EartDoc*, *2020*(1), 1-5. Retrieved from `https://www.earthdoc.org/content/papers/10.3997/2214-4609.202020145` doi: https://doi.org/10.3997/2214-4609.202020145

Ning, I. L. C. (2019). *Multicomponent distributed acoustic sensing: Concept, theory and applications* (Unpublished doctoral dissertation). Colorado School of Mines, Colorado.

Ning, I. L. C., & Sava, P. (2016). Multicomponent distributed acoustic sensing. In *Seg technical program expanded abstracts 2016* (p. 5597-5602). Retrieved from `https://library.seg.org/doi/abs/10.1190/segam2016-13952981.1` doi: 10.1190/segam2016-13952981.1

Ning, I. L. C., & Sava, P. (2018). Multicomponent distributed acoustic sensing: Concept and theory. *GEOPHYSICS*, *83*(2), P1-P8. Retrieved from `https://doi.org/10.1190/geo2017-0327.1` doi: 10.1190/geo2017-0327.1

Paitz, P. (2021). *Potentials of distributed acoustic sensing in seismic imaging* (Doctoral dissertation, ETH Zurich, Zurich). doi: 10.3929/ethz-b-000474545

Paitz, P., Edme, P., Gräff, D., Walter, F., Doetsch, J., Chalari, A., ... Fichtner, A. (2020, 10). Empirical Investigations of the Instrument Response for Distributed Acoustic Sensing (DAS) across 17 Octaves. *Bulletin of the Seismological Society of America*. Retrieved from `https://doi.org/10.1785/0120200185` doi: 10.1785/0120200185

Park, S., Tsai, V. C., & Ishii, M. (2019). Frequency-dependent p wave polarization and its sub-wavelength near-surface depth sensitivity. *Geophysical Research Letters*, *46*(24), 14377-14384. Retrieved from `https://agupubs.onlinelibrary.wiley.com/doi/abs/10.1029/2019GL084892` doi: https://doi.org/10.1029/2019GL084892

Peterson, D., Meyer, A., Dunn, K., Vecherin, S., Glaser, D., Costley, D., ... Moran, M. (2020). Improving detection of acoustic sources by coiling fiber optic cable. In S. S. Bishop & J. C. Isaacs (Eds.), *Detection and sensing of mines, explosive objects, and obscured targets xxv* (Vol. 11418, pp. 77 – 94). SPIE. Retrieved from `https://doi.org/10.1117/12.2559133` doi: 10.1117/12.2559133

Rind, D., & Down, W. L. (1979). Microseisms at palisades: 2. rayleigh wave and love wave characteristics and the geologic control of propagation. *Journal of Geophysical Research: Solid Earth*, *84*(B10), 5632-5642. Retrieved from `https://agupubs.onlinelibrary.wiley.com/doi/abs/10.1029/JB084iB10p05632` doi: https://doi.org/10.1029/JB084iB10p05632

Robertsson, J., & Curtis, A. (2002). Wavefield separation using densely deployed three-component single-sensor groups in land surface-seismic recordings. *Geophysics*, *67*, 1624-1633.

Robertsson, J. O. A., & Muyzert, E. (1999). Wavefield separation using a volume distribution of three component recordings. *Geophysical Research Letters*, *26*(18), 2821-2824.

Salem, H. (2000, 12). The compressional to shear-wave velocity ratio for surface soils and shallow sediments. *European Journal of Environmental and Engineering Geophysics*, *5*, 3-14.

Schmelzbach, C., Donner, S., Igel, H., Sollberger, D., Taufiqurrahman, T., Bernauer, F., ... Robertsson, J. (2018). Advances in 6c seismology: Applications of combined translational and rotational motion measurements in global and exploration seismology. *GEOPHYSICS*, *83*(3), WC53-WC69. Retrieved from `https://doi.org/10.1190/geo2017-0492.1` doi: 10.1190/geo2017-0492.1

Sollberger, D., Schmelzbach, C., Robertsson, J. O. A., Greenhalgh, S. A., Nakamura, Y., & Khan, A. (2016). The shallow elastic structure of the lunar crust: New insights from seismic wavefield gradient analysis. *Geophysical Research Letters*, *43*(19), 10,078-10,087. Retrieved from `https://agupubs.onlinelibrary.wiley.com/doi/abs/10.1002/2016GL070883` doi: https://doi.org/10.1002/2016GL070883

Stork, A. L., Baird, A. F., Horne, S. A., Naldrett, G., Lapins, S., Kendall, J.-M., ... Williams, A. (2020). Application of machine learning to microseismic event detection in distributed acoustic sensing data. *GEOPHYSICS*, *85*(5), KS149-KS160. doi: 10.1190/geo2019-0774.1

Svenningsen, L., & Jacobsen, B. H. (2007, 09). Absolute S-velocity estimation from receiver functions. *Geophysical Journal International*, *170*(3), 1089-1094. Retrieved from `https://doi.org/10.1111/j.1365-246X.2006.03505.x` doi: 10.1111/j.1365-246X.2006.03505.x

Tejedor, J., Macias-Guarasa, J., Martins, H. F., Pastor-Graells, J., Corredera, P., & Martin-Lopez, S. (2017). Machine learning methods for pipeline surveillance systems based on distributed acoustic sensing: A review. *Applied Sciences*, *7*(8). doi: 10.3390/app7080841

Tran, K. V., & Nguyen, T. N. (2019, 11). A novel method for computing the vertical gradients of the potential field: application to downward continuation. *Geophysical Journal International*, *220*(2), 1316-1329. Retrieved from `https://doi.org/10.1093/gji/ggz524` doi: 10.1093/gji/ggz524

Van Renterghem, C. (2019). *Novel developments in spatial wavefield gradient research for elastic wavefield decomposition* (Doctoral dissertation, ETH Zurich, Zurich). doi: 10.3929/ethz-b-000372269

White, R. (1980). Partial coherence matching of synthetic seismograms with seismic traces*. *Geophysical Prospecting*, *28*(3), 333-358. Retrieved from `https://onlinelibrary.wiley.com/doi/abs/10.1111/j.1365-2478.1980.tb01230.x` doi: https://doi.org/10.1111/j.1365-2478.1980.tb01230.x

Wiechert, E., & Zoeppritz, K. (1907). *Uber erdbebenwellen*. Retrieved from `http://worldcat.org`

Yilmaz, o. (2001). *Seismic data analysis* (Vol. 10). Society of Exploration Geophysicists. doi: 10.1190/1.9781560801580

Yin, S., Ruffin, P., & Yu, F. (2008). *Fiber optic sensors (2nd ed.)*. CRC Press. doi: 10.1201/9781420053661

Young, W., & Budynas, R. (2001). *Roark's formulas for stress and strain*. McGraw-Hill Education. Retrieved from `https://books.google.ch/books?id=pummClLoFXEC`

Appendix A Helicoidal fiber shapes - multicomponent sensing (theory)

The section below was written by the same authors as part of a preliminary project of the thesis, called the Research Module, a few months before the thesis project itself.

The directionality property of DAS can also be used in favor of potential multicomponent sensing. This concept of multicomponent sensing by means of DAS could potentially be a powerful and very interesting link between the relatively new technique of DAS and the branch of wavefield separation (J. Robertsson & Curtis, 2002). In order to get there, the full strain tensor must be retrieved, which consists of six independent components (Young & Budynas, 2001).

Until now, a popular approach has been to make use of the DAS directionality by deploying it in some form of helical shape (Kuvshinov, 2016) (Ning & Sava, 2018) (K. Innanen, 2017a). Throughout many fields of physics, the helical shape is a powerful concept and exhibits many advantages (Lin & Pisano, 1988).

Two groups of active DAS researchers (1. Ning & Sava and 2. Innanen & Eaid) have achieved the most promising results in terms of multicomponent DAS sensing so far. Both groups have taken an almost similar approach, where they project the axial strain measured by one or more DAS fibers from a cable coordinate frame to a fixed standard Cartesian frame and subsequently combine it with a least-squares method (Ning & Sava, 2018) (Eaid et al., 2018) (K. Innanen, 2017a).

First, they set up a system which translates the tangent $\hat{\mathbf{T}}(s)$ (direction vector) at any arc-length along the fiber s to a standard Cartesian frame as extensively described in K. Innanen (2017a) and shown in figure 24. This information is put into a rotation matrix which converts strain measured by the fiber in the fiber frame to a Cartesian strain field, as expressed by the following system (K. Innanen, 2017a):

$$\begin{bmatrix} e_{tt} & e_{tn} & e_{tb} \\ e_{nt} & e_{nn} & e_{nb} \\ e_{bt} & e_{bn} & e_{bb} \end{bmatrix} = \mathbf{R}(s) \begin{bmatrix} e_{11} & e_{12} & e_{13} \\ e_{21} & e_{22} & e_{23} \\ e_{31} & e_{32} & e_{33} \end{bmatrix} \mathbf{R}^{-1}(s) \tag{21}$$

When taking this approach it is important to account for the gauge length. For this purpose, an averaging matrix can be constructed, which is explained in a detailed way in Ning & Sava (2018), or an alternative can be found (K. Innanen, 2017a). In essence, when at least six separate locations at different arc-lengths s are known with their corresponding DAS measurements, a least-squares system can be formed as follows (K. Innanen, 2017a) (Ning & Sava, 2018):

$$\mathbf{m} = \left(\mathbf{G^T A^T A G}\right)^{-1} \mathbf{G^T A^T d}, \tag{22}$$

where the previously described rotation matrix is embedded in the forward operator $\mathbf{G}$, $\mathbf{A}$ is the averaging matrix (to account for the gauge length), $\mathbf{d}$ is the data vector at the measurement locations and the model $\mathbf{m}$ is the full strain tensor at a given location (Ning & Sava, 2018).

From here, the authors take slightly different routes. First it was Ning & Sava (2016), who proposed the idea of a chirping helix, which is a helical shape with a varying pitch- or wrapping angle. The pitch- or wrapping angle is defined as the complement of the angle between the tangent vector and the axial direction of the DAS cable core (Lin & Pisano, 1988). Afterwards, K. Innanen (2017a) came up with the concept of a n-order helix, where a 0-helix is a straight fiber, a 1-helix is a standard helical configuration and a 2-helix is described by a helix which cable axis is arranged in a helical shape is again, etc. This is displayed in Figure 25.

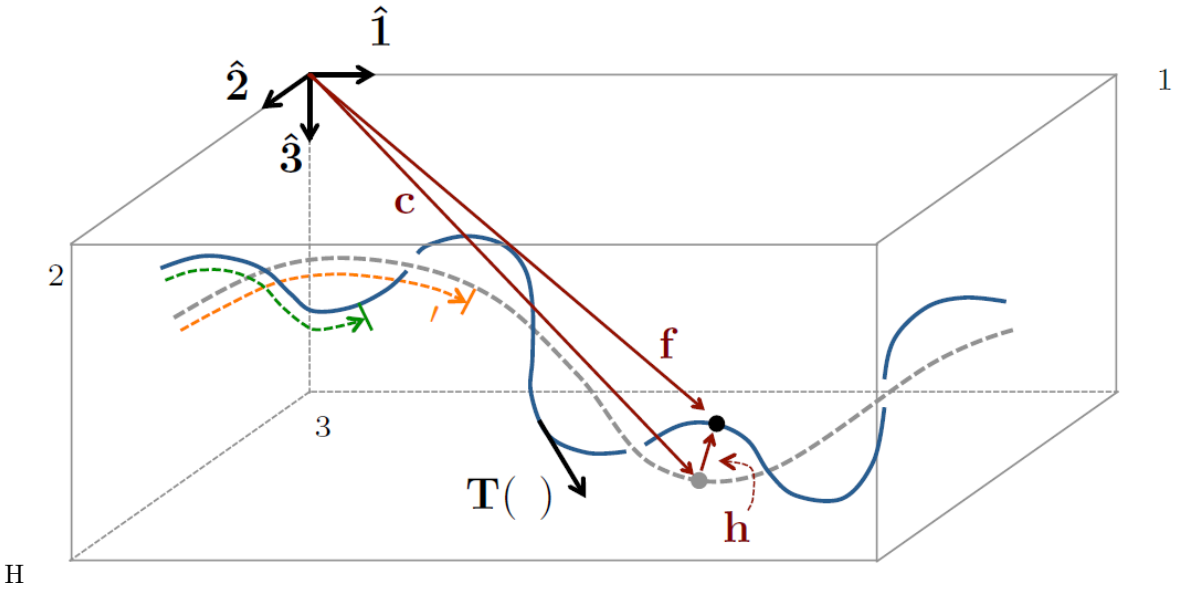

Figure 24: *Figure from K. Innanen (2017a) illustrating the helical parameterization. The location vector of some point along the fiber (blue line) f is given by $f = c + h$, where c is the position vector of the central axis of the cable (grey dashed) and h points from the cable axis to the fibre which winds around it (blue line). The dashed green line is the arc-length s along the fiber and the orange dashed line is the arc-length s' along the cable axis. The tangent $\hat{\mathbf{T}}(s)$ is dependent on s.*

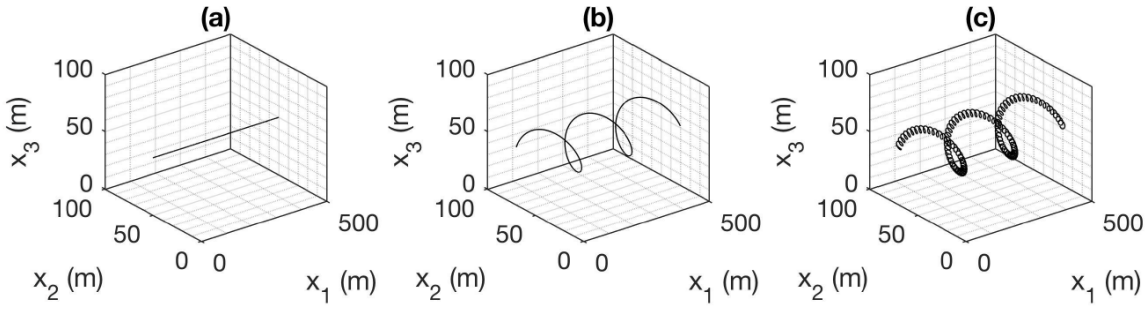

Figure 25: *Overview from K. Innanen (2017a) of different helix orders. a) 0-helix, b) 1-helix and c) 2-helix.*

In 2018, Ning & Sava (2018) improved the chirping helix-idea by proposing a setup with one straight fiber in the core and two helical fibers around, with 20 and 60 degree pitch angles. The results of applying this geometry to synthetic data was already very promising. One drawback of all three methods is that in order to perform the least-squares calculation of the complete strain tensor, you need to group consecutive strain measurements along the optical fiber within a defined window (Ning & Sava, 2018). This window consists at least of 6 independent consecutive measurements, but optimally considerably more to obtain a better-posed least-squares problem. As it is important that the consecutive DAS measurements needed for the least-squares solution are independent, their measured strain cannot overlap and hence, the gauge length can not be larger than the channel spacing. This obviously puts constraints on this proposal considering the current standard gauge lengths. Additionally, within such a window of grouped measurements, it has to be assumed that the

wavefield does not change within the window, thus that it is invariant at the window scale. In order to let this be a valid assumption, the wavelength of the incoming wavefield must be much larger than the window length, at least five times according to Ning & Sava (2018).

These problems were subsequently solved, at least in a theoretical/conceptual way, by Ning (2019). Ning (2019) proposed a setup with one straight fiber in the middle and five helical fibers around with equal and constant pitch angles. This configuration should be easier to manufacture and overcomes the above-described problem of the large wavelength assumption, because no grouping of many consecutive channels is needed (Ning, 2019). Again, the synthetic results are very promising, even with much noise added, but this configuration has not been tested in the field yet, regarding multicomponent sensing.

Besides that, it is important to mention that these authors assume (synthetic) gauge lengths which are much smaller compared to the Yverdon field experiments for example. For example Ning & Sava (2018) and Ning (2019) use a gauge length of 1m, or even 0.1m to obtain the best results. These smaller gauge lengths will probably become available in the near future as Ning & Sava (2018) mention, but are currently not standard yet.

Appendix B Synthetic model: Validity 4-receiver approximations

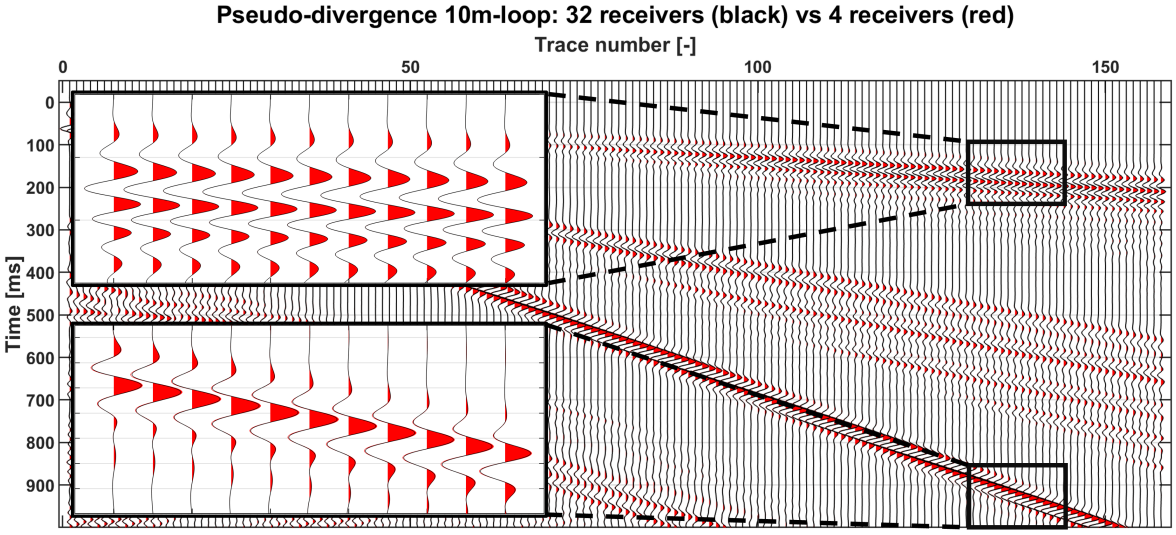

Figure 26: *Synthetic comparison of the pseudo-divergence obtained from the 10m-loop approximated by 32 receivers (black) 4 receivers (red). For loops smaller than 10m circumference (diameter 3.18m), the difference between a 4-receiver and 32-receiver loop approximation becomes negligible. An AGC with a 300ms window length has been applied. The two boxes display zoomed windows of parts of the early and late arrivals (refractions and surface waves respectively). Further information regarding the synthetic model parameters can be found in Section 3.2. The plotted traces have offsets ranging from 30-500m.*

Appendix C Data quality

C.1 Results individual FD geophone pairs

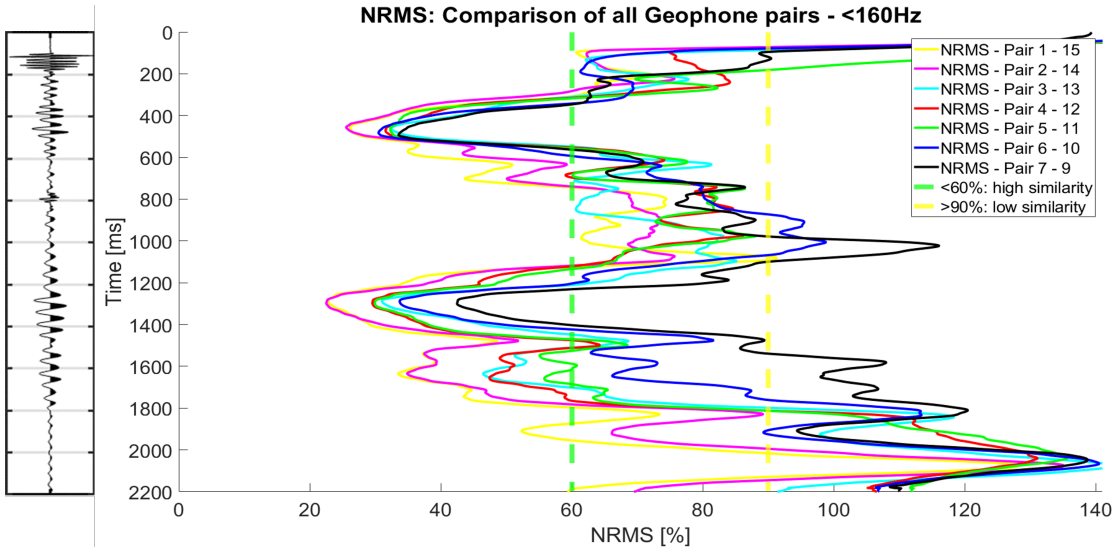

Figure 27: *Shot-to-shot NRMS results of all FD geophone pairs for shots 2-18 at shot location 97. The vertical green and yellow line denote the defined boundaries of high and low similarity (Nap, 2020). On the left, a trace of the average FD geophone result is added as signal reference. In general, we observe lower repeatability for the more closely-spaced FD geophone pairs (7-9, 6-10).*

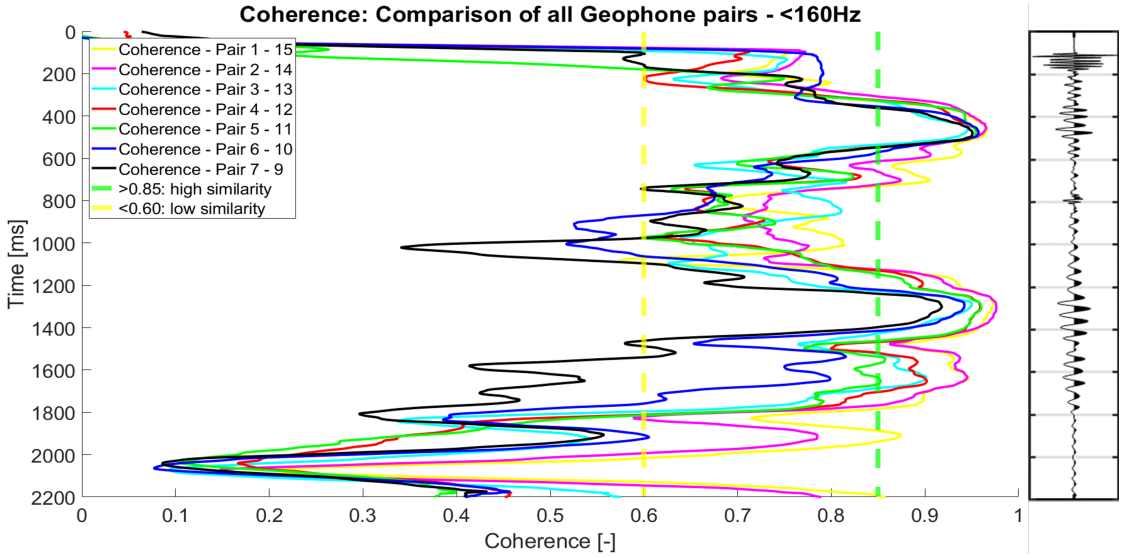

Figure 28: *Shot-to-shot Coherence results of all FD geophone pairs for shots 2-18 at shot location 97. The vertical green and yellow line denote the defined boundaries of high and low similarity (Nap, 2020). On the right, a trace of the average FD geophone result is added as signal reference. In general, we observe lower repeatability for the more closely-spaced FD geophone pairs (7-9, 6-10).*

C.2 Coherence results Yverdon configurations

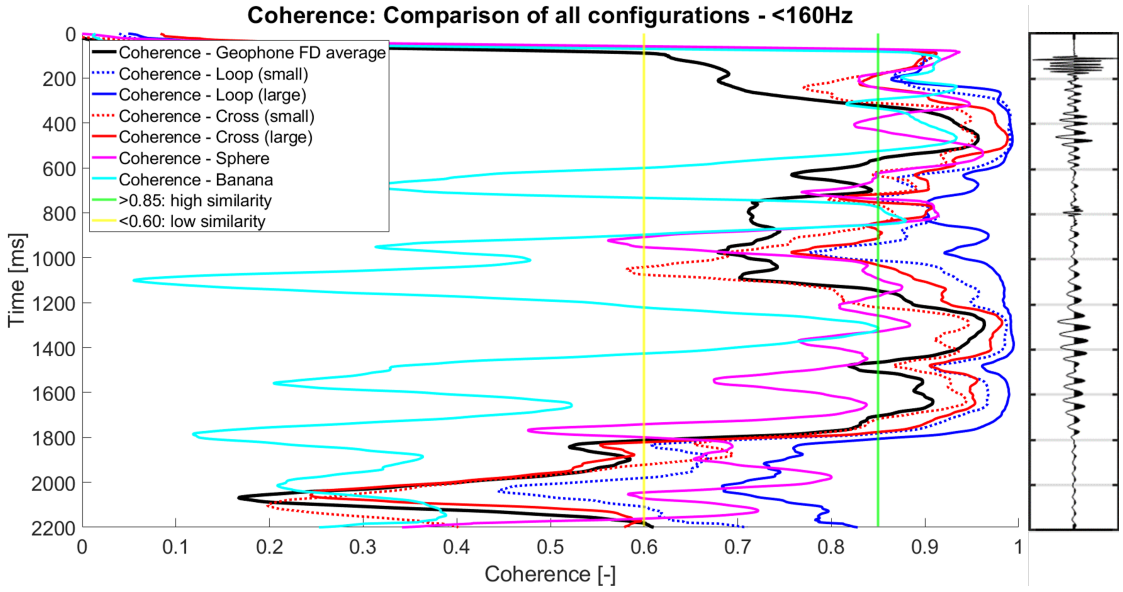

Figure 29: *Shot-to-shot Coherence results of all field configurations for shots 2-18 at shot location 97. The vertical green and yellow line denote the defined boundaries of high and low similarity (Nap, 2020). On the right, a trace of the average FD geophone result is added as signal reference. In general, we observe lower repeatability for the more bundled configurations (sphere & mini-cross).*

C.3 NSD results Yverdon configurations

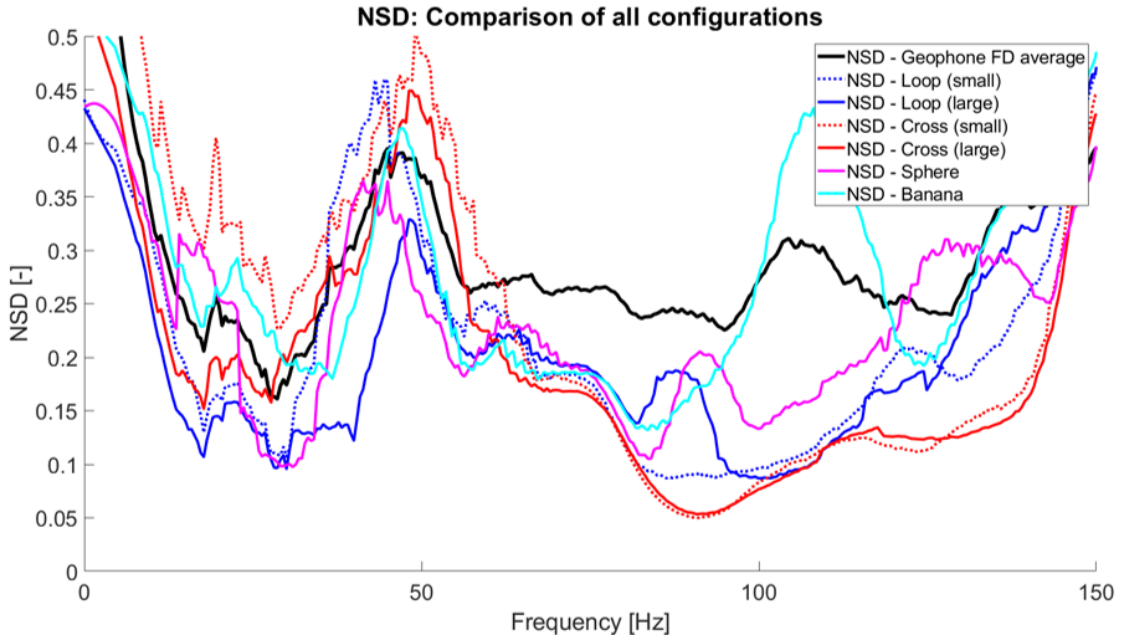

Figure 30: *Shot-to-shot NSD results of all field configurations for shots 2-18 at shot location 97. The FD geophone configurations shows remarkably high NSD values for the refracted waves (80Hz).*

C.4 Influence of nearby road

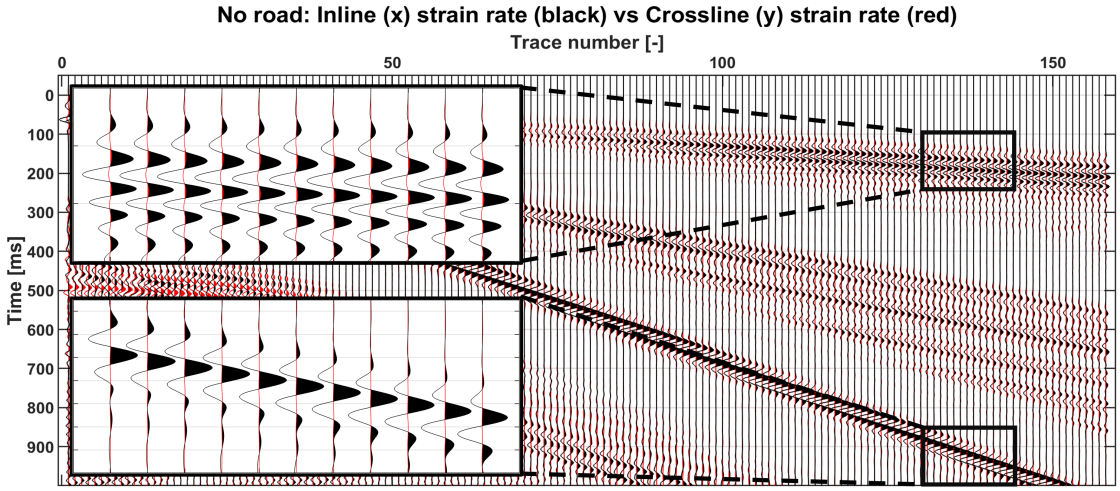

Figure 31: *Synthetic comparison of the inline strain rate e_{xx} (black) and crossline strain rate e_{yy} (red), for a simulation without road. The measurement recordings are obtained from surface receivers 10m next to the potential road feature. Note the small strain rate amplitudes in y-direction (red), compared to x-direction (black), for both the early refractions and later surface waves. An AGC with a 300ms window length has been applied. Further information regarding the synthetic model parameters can be found in Section3.2. The plotted traces have offsets ranging from 30-500m.*

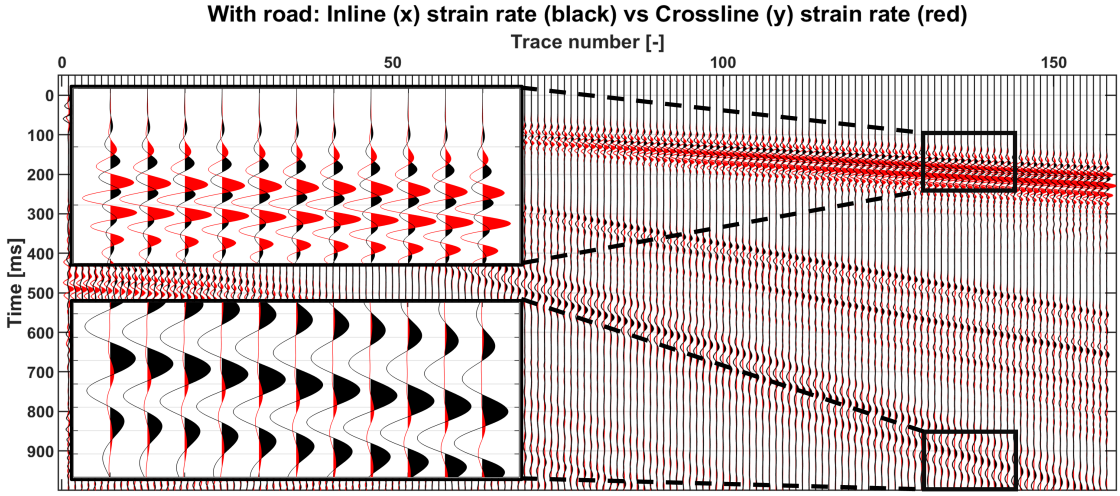

Figure 32: *Synthetic comparison of the inline strain rate e_{xx} (black) and crossline strain rate e_{yy} (red), for a simulation including the road. The measurement recordings are obtained from surface receivers 10m next to the road. In contrast to Figure 31, note the considerable strain rate amplitudes in y-direction (red) for the early refractions. Considering the surface waves, the crossline strain rate amplitudes remain small. However, the waveform of the inline strain component (x-direction) is changed due to the synthetic road feature. An AGC with a 300ms window length has been applied. Further information regarding the synthetic model parameters can be found in Section3.2. The plotted traces have offsets ranging from 30-500m.*

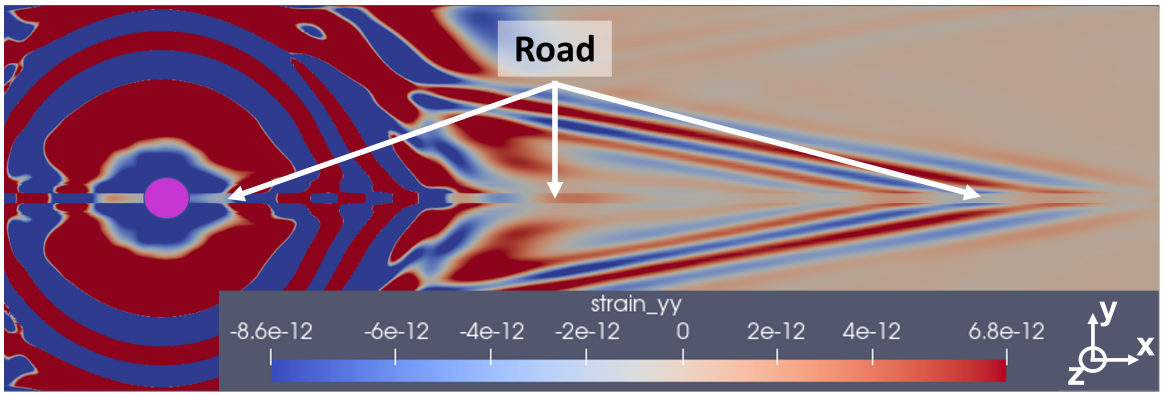

Figure 33: *Wavefield snapshot of the crossline strain rate e_{yy} at the model surface of a simulation including the synthetic road. Note the road feature along the x-direction 1) causing crossline scattering of the refractions and 2) disrupting the surface wavefield.*

Appendix D Loop & Cross: Pseudo-divergence

D.1 Synthetic comparison small 10m-loop and pseudo-divergence Salvus reference

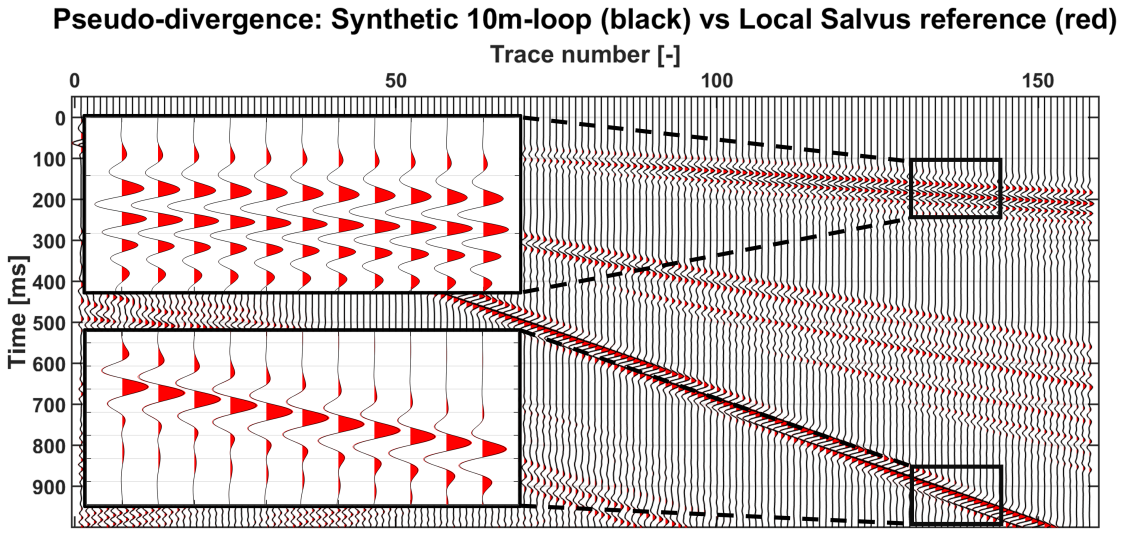

Figure 34: *Comparison of the synthetic pseudo-divergence obtained by the large synthetic 10m-loop (black) and the local pseudo-divergence reference (red). The match is solid for both refractions and surface waves. The loop diameter is 3.18m. An AGC with a 300ms window length has been applied. The two boxes display zoomed windows of the refracted and surface waves. Further information regarding the synthetic model parameters can be found in Section 3.2.*

D.2 Synthetic comparison small 2.5m-cross and pseudo-divergence Salvus reference

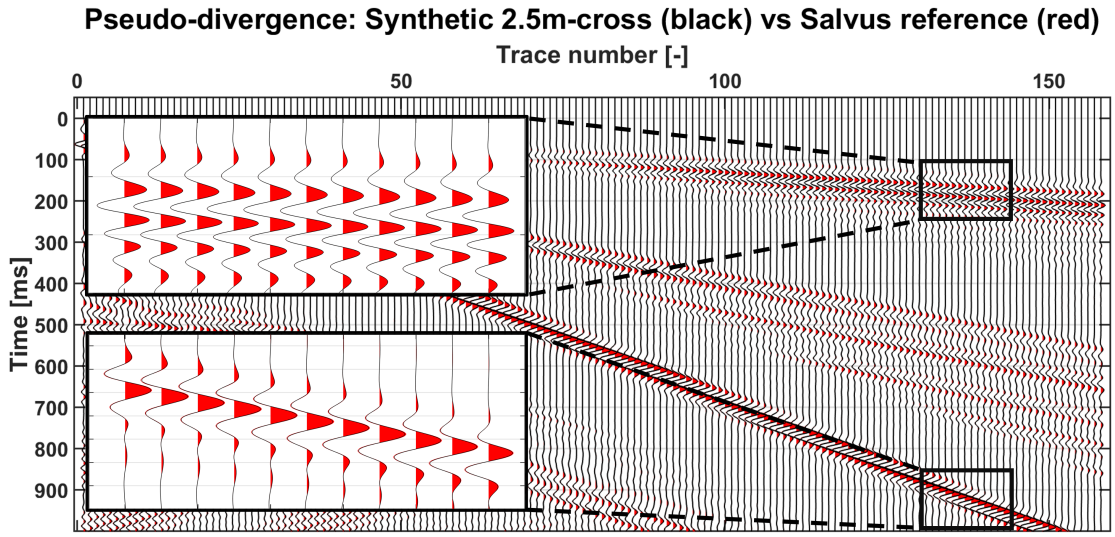

Figure 35: *Comparison of the synthetic pseudo-divergence obtained by the small synthetic 2.5m-cross (black) and the local pseudo-divergence reference (red). The match is solid for both refractions and surface waves. An AGC with a 300ms window length has been applied. The two boxes display zoomed windows of the refracted and surface waves. Further information regarding the synthetic model parameters can be found in Section 3.2.*

D.3 Synthetic comparison large 5m-cross and pseudo-divergence Salvus reference

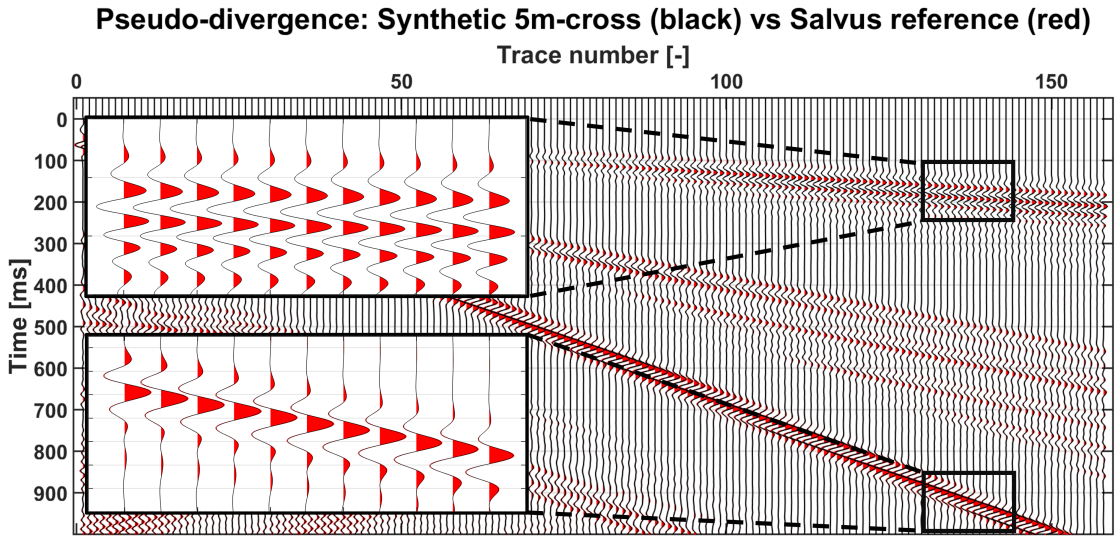

Figure 36: *Comparison of the synthetic pseudo-divergence obtained by the large synthetic 5m-cross (black) and the local pseudo-divergence reference (red). The match is solid, except for a slight amplitude misfit for the surface waves. An AGC with a 300ms window length has been applied. The two boxes display zoomed windows of the refracted and surface waves. Further information regarding the synthetic model parameters can be found in Section 3.2.*

D.4 Field data comparison small 2.5m-DAS cross and FD geophone

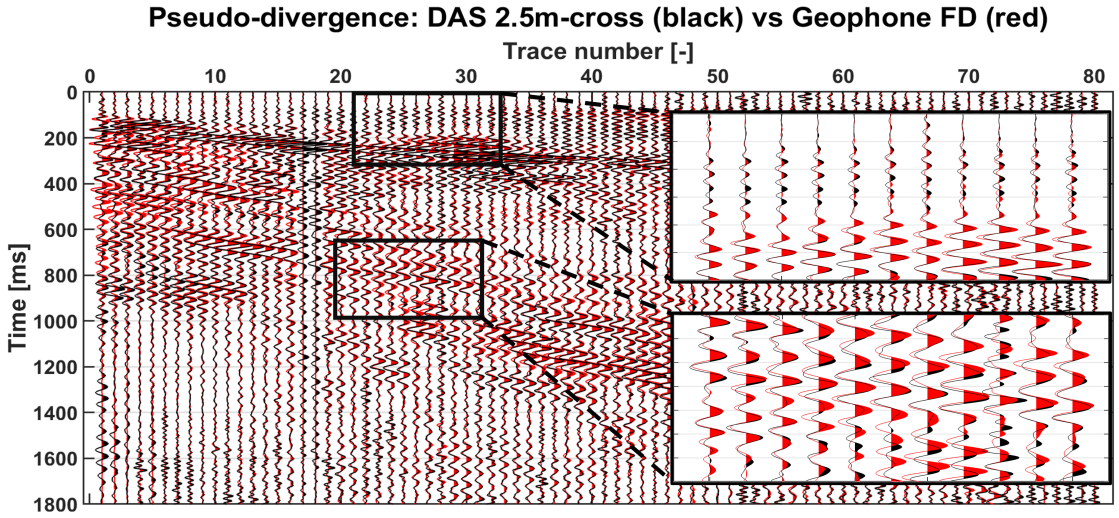

Figure 37: *Comparison of the pseudo-divergence obtained by the small 2.5m-DAS cross (black) and geophone pair 5-11 (red). Generally, the match is solid in terms of phase and relative energy distribution. The geophone spacing in both horizontal directions is 3m and the trace offset ranges from 71m - 300m (moving source). Ormsby bandpass filter: [7-60Hz] & AGC: 1200ms. The DAS cross amplitudes have been multiplied with a factor of 1.83 to equalize the norms of both gathers.*

D.5 Field data comparison large 5m-DAS cross and FD geophone - incl. high fq

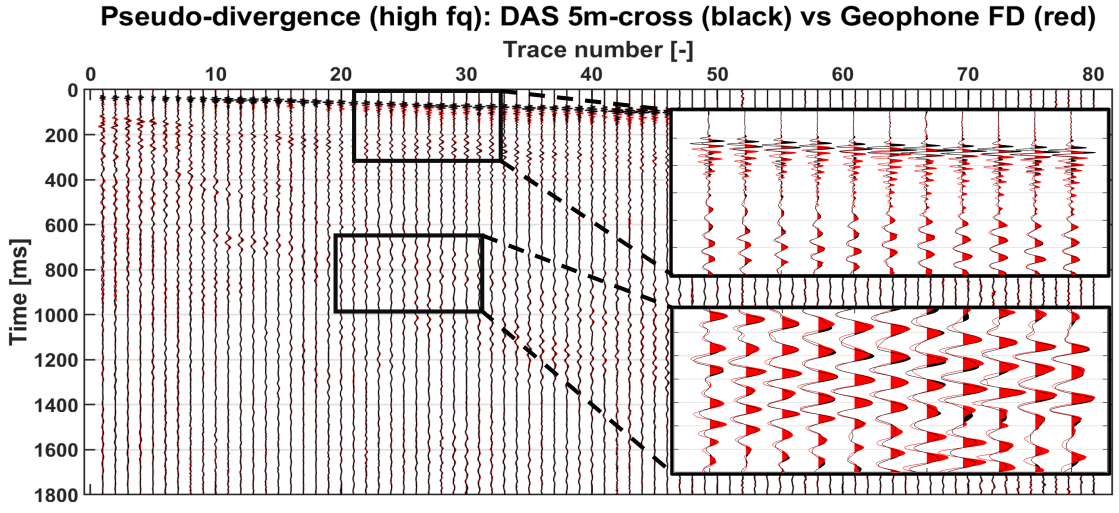

Figure 38: *Comparison of the pseudo-divergence obtained by the large 5m-DAS cross (black) and geophone pair 5-11 (red) including higher frequencies. The match is weak - the refraction event is much sharper resolved by the DAS cross. The geophone spacing in both horizontal directions is 3m and the trace offset ranges from 71m - 300m (moving source). Ormsby bandpass filter: [7-160Hz] & AGC: 1200ms. The DAS cross amplitudes have been multiplied with a factor of 1.39 to equalize the norms of both gathers.*

D.6 Field data comparison small 10m-DAS loop and FD geophone

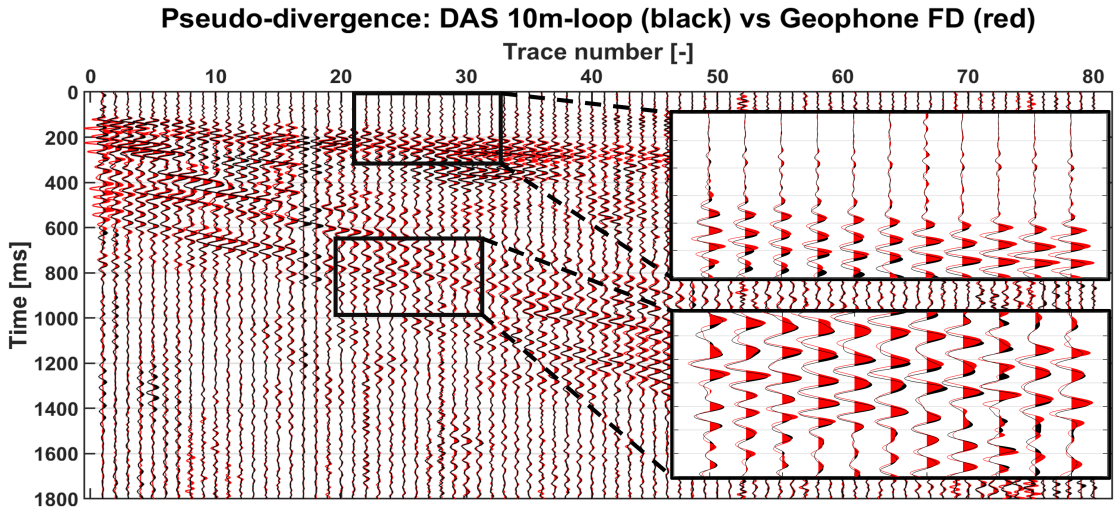

Figure 39: *Comparison of the pseudo-divergence obtained by the small 10m-DAS loop (black) and geophone pair 5-11 (red). The match is solid in terms of phase and relative energy distribution, except for a minor relative phase shift. The geophone spacing in both horizontal directions is 3m and the trace offset ranges from 71m - 300m (moving source). Ormsby bandpass filter: [7-60Hz] & AGC: 1200ms. The DAS loop amplitudes have been multiplied with a factor of 1.19 to equalize the norms of both gathers.*

D.7 Field data comparison large 20m-DAS loop and FD geophone - incl. high fq

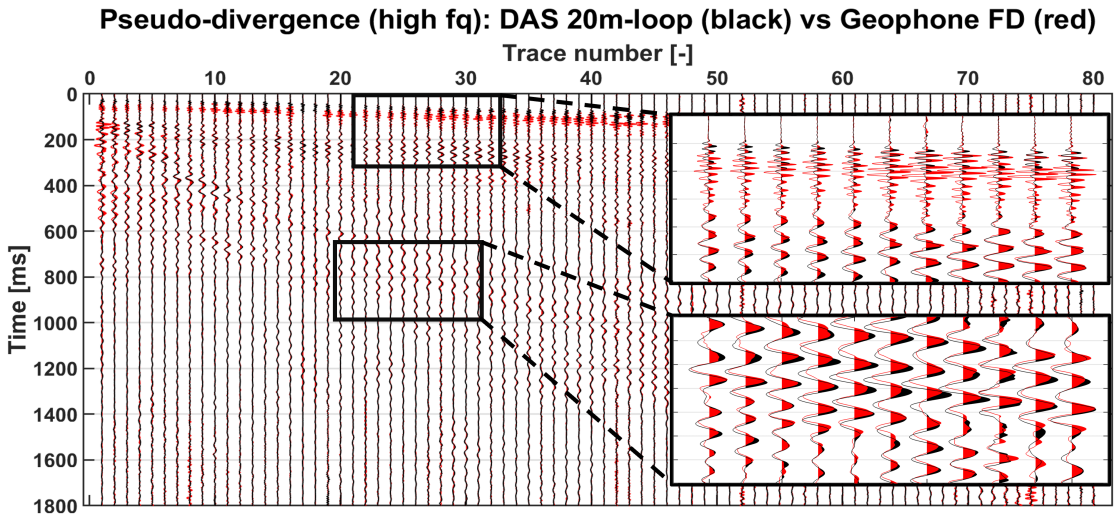

Figure 40: *Comparison of the pseudo-divergence obtained by the large 20m-DAS loop (black) and geophone pair 5-11 (red) including higher frequencies. The match is weak for the refractions, especially in terms of amplitudes. The geophone spacing in both horizontal directions is 3m and the trace offset ranges from 71m - 300m (moving source). Ormsby bandpass filter: [7-160Hz] & AGC: 1200ms. The DAS loop amplitudes have been multiplied with a factor of 1.65 to equalize the norms of both gathers.*

Appendix E Sphere: Gradient decomposition

E.1 Synthetic comparison vertical gradient: Sphere vs Salvus reference

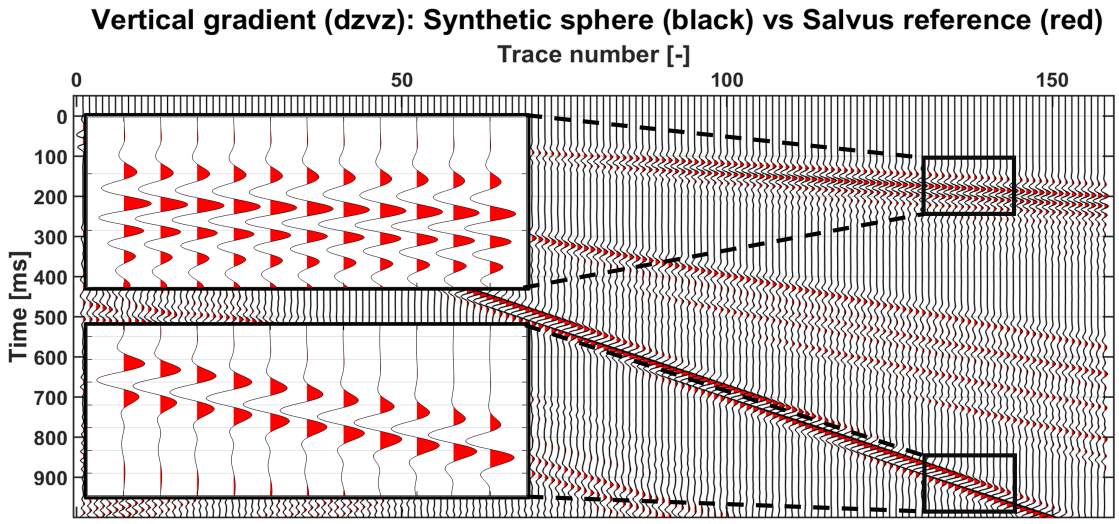

Figure 41: *Comparison of the vertical gradient (dzvz) obtained by the synthetic sphere (black) and the local Salvus reference (red). The traces show a good match, numerically confirming the validity of the sphere gradient decomposition. The sphere diameter is 0.50m. An AGC with a 300ms window length has been applied. The two boxes display zoomed windows of the refracted and surface waves. Further information regarding the synthetic model parameters can be found in Section 3.2.*

E.2 Field data: Full divergence from DAS sphere

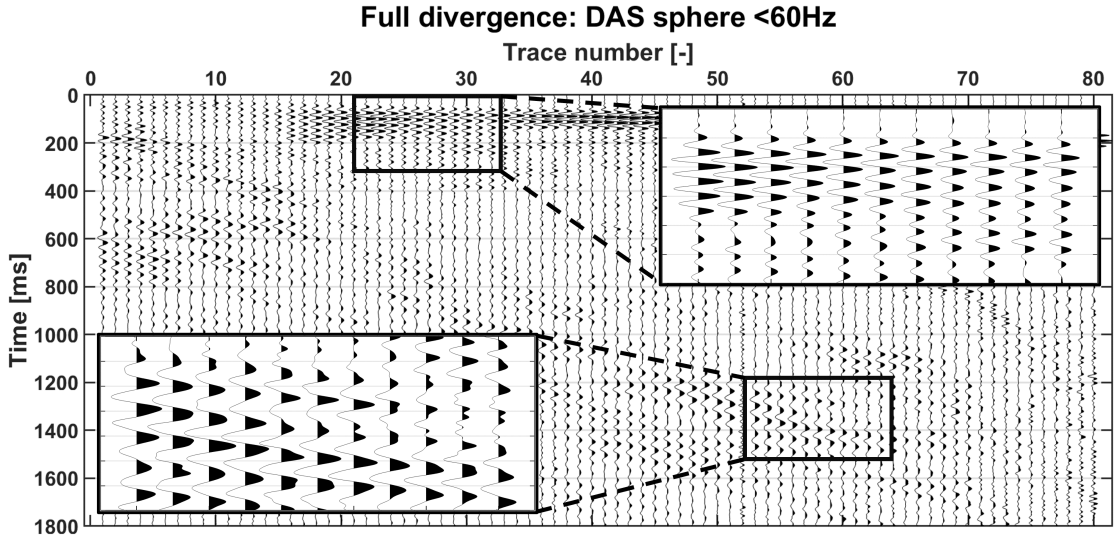

Figure 42: *Wiggle plot of the full divergence ($\leq$ 60Hz) retrieved from summation of the decomposed sphere gradients. Note the large amount of energy present in the refractions. The trace offset ranges from 71m - 300m (moving source) with larger spacing between trace 70 and 80. Ormsby bandpass filter: [7-60Hz] & AGC: 1200ms.*

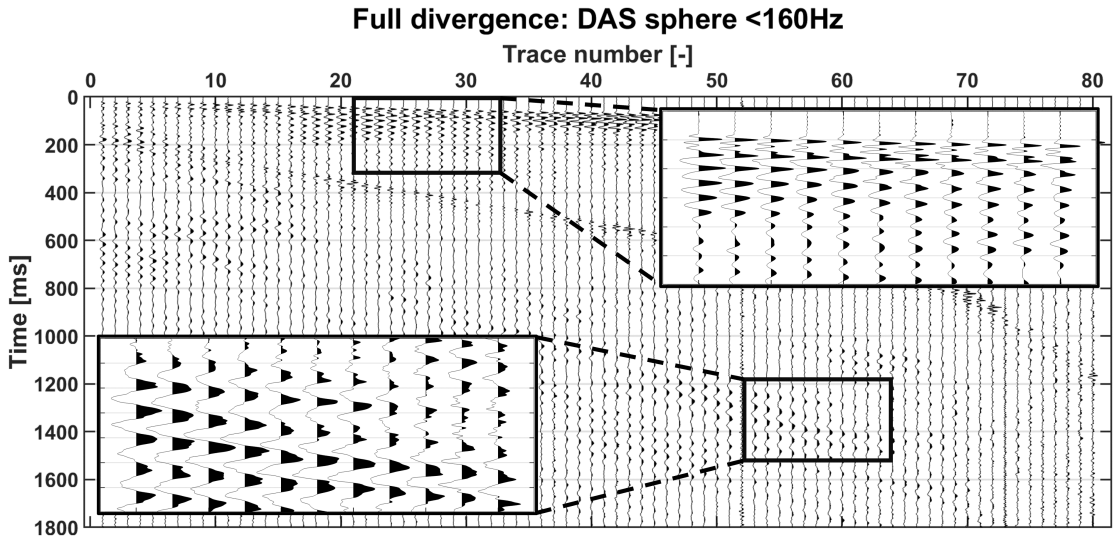

Figure 43: *Wiggle plot of the Yverdon full divergence ($\leq$ 160Hz) retrieved from summation of the decomposed DAS sphere gradients. Note the large amount of energy present in the refractions and the recognizable air wave. The trace offset ranges from 71m - 300m (moving source) with larger spacing between trace 70 and 80. Ormsby bandpass filter: [7-160Hz] & AGC: 1200ms.*

E.3 Synthetic comparison vertical gradient (dzvz) and pseudo-divergence at the free surface

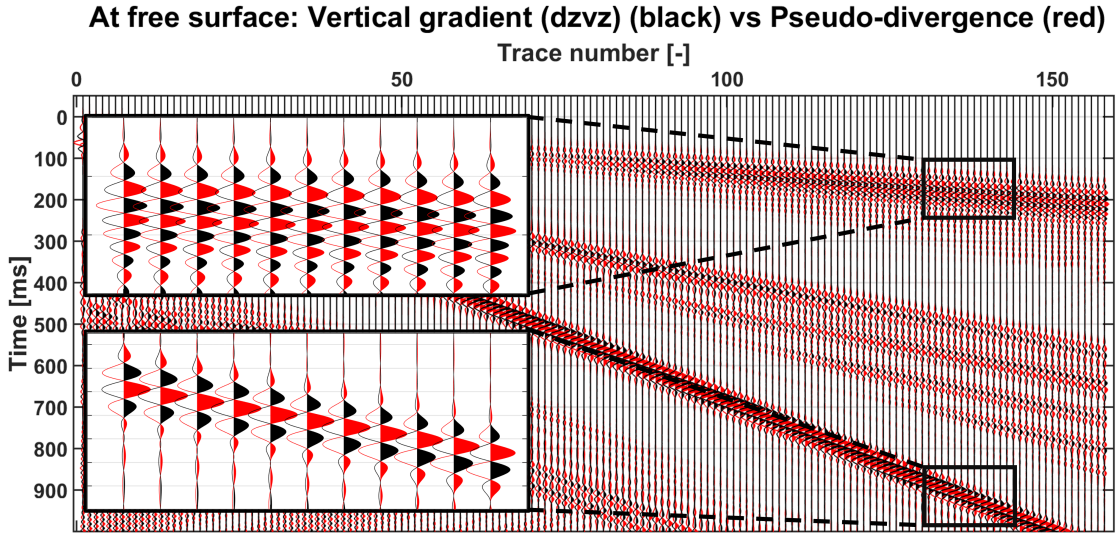

Figure 44: *Synthetic comparison at the free surface of the vertical gradient (dzvz) (black) and the pseudo-divergence (red). The amplitudes of the vertical gradient and pseudo-divergence largely cancel each other due to the free surface effect - the resultant is the full divergence. The sphere diameter is 0.50m. An AGC with a 300ms window length has been applied. The two boxes display zoomed windows of the refracted and surface waves. Further information regarding the synthetic model parameters can be found in Section 3.2.*

E.4 Field data DAS sphere: Vs/Vp-ratio for different wave types and frequencies

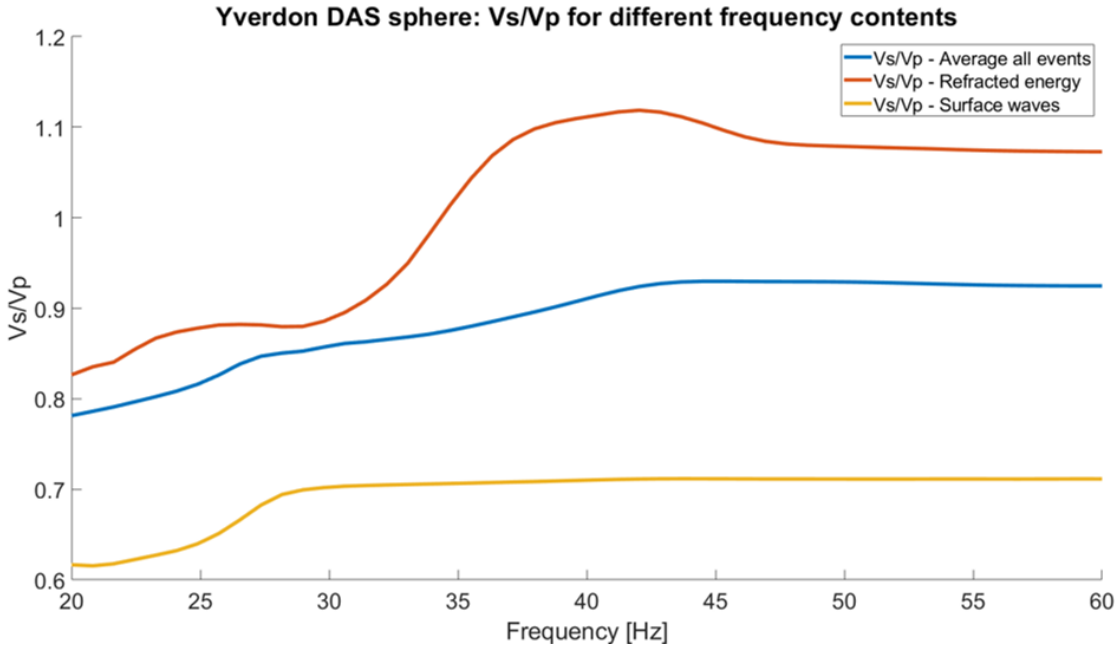

Figure 45: *Plot of the computed V_S-V_P-ratio values, based on the decomposed gradients from the DAS sphere, for different frequencies and wave types (refractions and surface waves). The refracted arrivals clearly result in higher (more unrealistic) ratios, just as including higher frequencies (shorter wavelengths).*

Appendix F DAS: Local shear wave velocity estimation

F.1 Derivation shear velocity from DAS loop + 3C geophone configuration

The derivation of the Equation 20, providing the shear velocity from a fiber loop + 3C-geophone configuration, is based on Equations 17, 18 and 19 in Chapter 7:

$$V_S = \frac{\sin\left(\frac{1}{2}\overline{i_P}\right)}{p}, \tag{23a}$$

$$\tan(\overline{i_P}) = \frac{U_x^P}{U_z^P}, \tag{23b}$$

$$p_{x,y} = \frac{S_{x,y}}{A_{x,y}}, \tag{23c}$$

where V_S is the S-wave velocity, $\overline{i_P}$ the apparent incidence angle, p the horizontal slowness/ray parameter, U the measured wavefield (particle displacement/velocity/acceleration), $S_{x,y}$ the strain rate and $A_{x,y}$ the particle acceleration in x- and y-direction. The superscript P denotes the P-wave energy, which is a requirement for the V_S-estimation approach. For convenience, we will leave away the superscript P for the rest of the derivation.

Equations 23a and 23b can be combined to obtain the shear velocity from horizontal slowness and the ratio of the horizontal and vertical wavefield:

$$V_S = \frac{\sin\left(\frac{1}{2}\left(\tan^{-1}\left(\frac{U_x}{U_z}\right)\right)\right)}{p} \tag{24}$$

According to Equation 23c, we can replace the horizontal slowness by the ratio of the horizontal strain rate and particle acceleration. Hence, the local shear wave velocity can estimated in the 2D x-z plane as follows:

$$V_S = \frac{\sin\left(\frac{1}{2}\left(\tan^{-1}\left(\frac{A_x}{A_z}\right)\right)\right)}{\frac{S_x}{A_x}} \tag{25}$$

This expression is for example applicable to a configuration consisting of an inline DAS cross string and one centred 3C-geophone.

This 2D expression in the x-z plane can be extended to a multi-directional 3D setting, applicable to a DAS cross + 3C-geophone arrangement, now including both the x- and y-string of the cross configuration:

$$V_S = \frac{\sin\left(\frac{1}{2}\left(\tan^{-1}\left(\frac{\sqrt{A_x^2+A_y^2}}{A_z}\right)\right)\right)}{\left(\frac{\sqrt{S_x^2+S_y^2}}{\sqrt{A_x^2+A_y^2}}\right)} \tag{26}$$

The omni-directional DAS loop can not distinguish between S_x and S_y separately, but is only sensitive to the sum of both horizontal gradients (see Chapter 5). Hence, the expression can simplified to the final expression applicable to the fiber loop + centred 3C-geophone configuration, as presented in Chapter 7:

$$V_S = \frac{\sin\left(\frac{1}{2}\left(\tan^{-1}\left(\frac{\sqrt{A_x^2+A_y^2}}{A_z}\right)\right)\right)}{\left(\frac{S_{x+y(loop)}}{\sqrt{A_x^2+A_y^2}}\right)} \tag{27}$$

F.2 Vs-approximation field data: inline cross string + 3C geophone

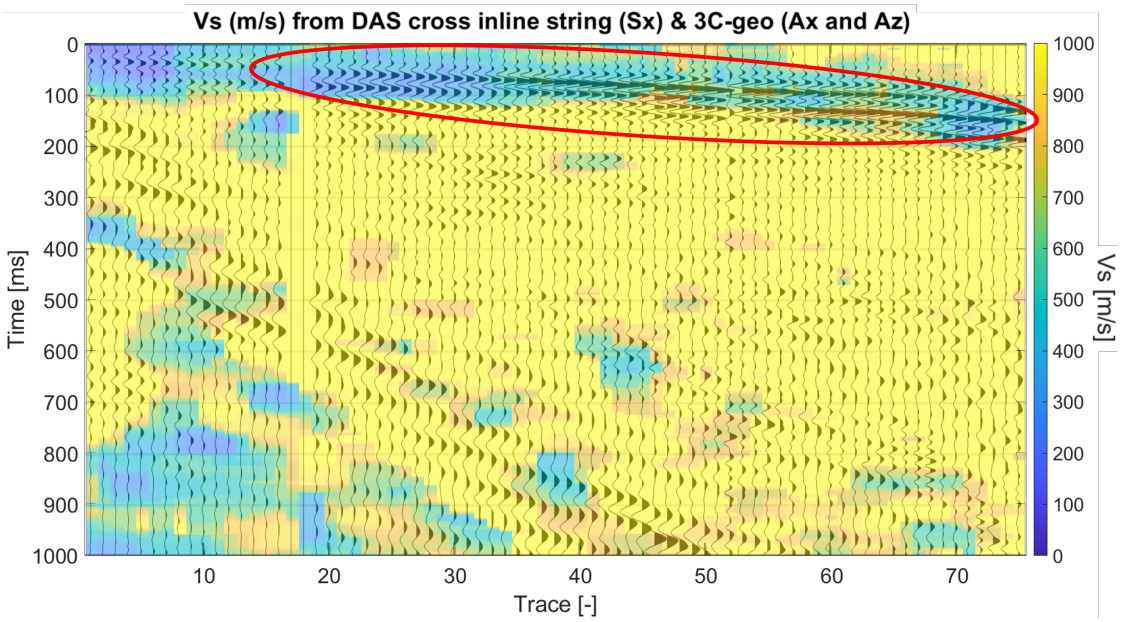

Figure 46: *Field data receiver gather of the V_z-component overlain by the computed V_S-values from the DAS inline cross string + 3C-geophone configuration (only inline sensitive). The red ellipse encircles the refracted wave arrivals which provide plausible V_S-estimations and which are slightly more stable compared to the DAS loop + 3C-geophone V_S-results . Regarding the V_z receiver gather: The data has been bandpass filtered by an Ormsby-filter [7-60Hz] and an AGC is applied with a 1200ms window length.*

F.3 Influence synthetic road on x- and (x+y)-sensitive configurations

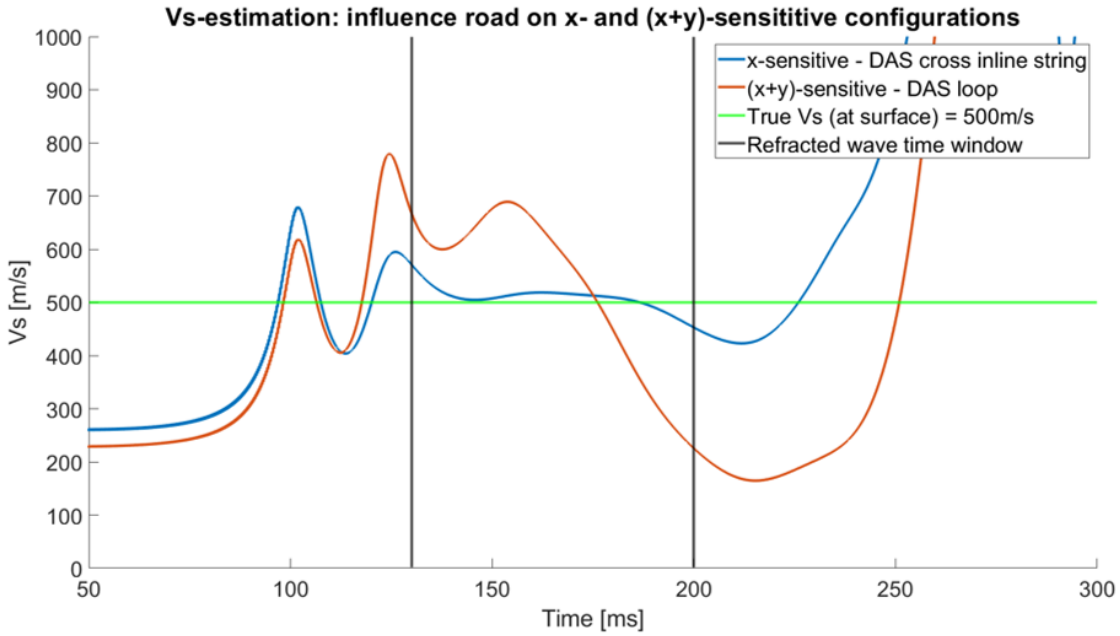

Figure 47: *Plot from a simulation including the road feature, showing a synthetic comparison of the computed V_S-results for the inline x-sensitive cross string + 3C geophone configuration and inline & crossline (x+y)-sensitive loop + 3C geophone configuration. Note the large unstable influence of the road on the (x+y)-sensitive loop + 3C geophone configuration results, due to the violated single event assumption. The green line denotes the true V_S-reference at the surface and the black lines show the refracted wave time window (pure P-wave energy). The selected offset is 360m. Further information regarding the synthetic model parameters, see Section 3.2.*